

A targeted proteomics approach for the
investigation of drug-induced liver
injury in hepatic organoids using nano
liquid chromatography mass
spectrometry

Maria Schüller



Thesis for the Master's Degree in chemistry
60 study points

Bioanalytical Chemistry
Department of Chemistry
Faculty of Mathematics and Natural Sciences

UNIVERSITY OF OSLO

05/2020

© Maria Schüller

2020

A targeted proteomics approach for the investigation of drug-induced liver injury in hepatic organoids using nano liquid chromatography mass spectrometry

Maria Schüller

<http://www.duo.uio.no/>

Printed at Representralen

Preface

The work of this master's thesis has been carried out at the Department of Chemistry, University of Oslo (the group for Bioanalytical Chemistry), in the time-period from August 2018 to May 2020. This project was supervised by Professor Steven Ray Wilson (main supervisor), Professor Elsa Lundanes, and PhD candidate Frøydis Sved Skottvoll. I would like to thank all for their support and guidance through this work and I greatly appreciate the freedom they have given me to pursue my scientific ambitions. Professor Steven Ray Wilson has always encouraged me and motivated me with his "you can do it"-spirit and Professor Elsa Lundanes has always been there for educational and technical support and guidance. A special thank you to PhD candidate Frøydis Sved Skottvoll who has closely followed up on me, instructed me and given me proper instrument training throughout my thesis. She has been a great companion in both scientific and social endeavors.

I also want to thank PhD candidate Henriette Engen Berg who was able to spontaneously provide me with in-house analytical columns. Without her, a lot of experiments could not have been completed.

During my work, I also had the pleasure of collaborating with, and being a part of the Hybrid technology Hub. Here, I have been able to develop cross-disciplinary communication skills and found the inspiration to incorporate fields of science that are outside our research groups' expertise. A special thank you to PhD Sean Harrison and the Sullivan group for providing me with organoids and collaborating with me on one of my experiments.

I want to thank the Olav Thon foundation for providing the funding for this work. This funding has also allowed me to present part of my work at the HPLC conference (2019) in Milan, where I have been able to evolve as a scientist and meet many aspiring scientists. I sincerely hope you are pleased with my achievements.

Lastly, I want to thank all my fellow students at the group for Bioanalytical Chemistry whose emotional and social support I couldn't have been without. I also want to send lots of love to my mom and my grandparents, who have been my number one cheerleader's through the ups and downs in these years.

Abstract

Late-stage drug attrition and post-market withdrawals attributed to drug-induced liver injury (DILI) has been a prevailing concern for the pharmaceutical industry. The current gaps in preclinical safety assessment impede the termination of DILI drug candidates to earlier stages of drug development, with the consequence of possibly exposing patients to hepatotoxic agents. Recent advances in liver-emulating models, with the development of hepatic organoids, seem promising in filling these gaps. The purpose of this study was to look into opportunities for the advancement of the preclinical safety assessment of the hepatic system. This was approached by combining the liver-emulating power of hepatic organoids with the well-studied protein biomarker alanine aminotransferase isoform 1 (ALT1) to investigate their compatibility with nano liquid chromatography mass spectrometry (nanoLC-MS). A targeted proteomics approach for the absolute quantification of ALT1 was developed by a thorough assessment of signature peptide candidates and corresponding multiple reaction monitoring (MRM) transitions. NanoLC-MS platform optimization was performed to maximize detection sensitivity and reliability. From empirical nanoLC-MS platform optimization, the greatest improvement was achieved from collision energy optimization, with an increase of mean peptide peak area of 22%. ALT1 peptide assessment showed that the peptide LLVAGEGHTR with the MRM fragments y_{8+} and y_{7+} were best suited to infer the presence of ALT1 in absolute quantification. The finalized method was applied for the investigation of drug-induced liver injury in hepatic organoids, where acetaminophen was used as the model drug. This work has shown that ALT1 quantification with a nanoLC-MS platform is feasible and has great potential to support preclinical DILI detection. Further studies must be conducted to give reliable statements on the applicability of the method for drug-induced ALT1 release in hepatic organoids.

Table of content

Preface.....	V
Abstract	VII
1 Abbreviations	1
2 Introduction.....	3
2.1 The drug development process.....	3
2.1.1 Currently faced challenges in drug development.....	4
2.2 The role of the liver in drug metabolism.....	5
2.2.1 Liver physiology, histology, and blood supply.....	5
2.2.2 Drug metabolism.....	6
2.3 Drug-induced liver injury.....	7
2.3.1 Acetaminophen-induced liver injury.....	7
2.4 <i>In vitro</i> models applicable for preclinical liver safety assessment.....	9
2.4.1 Hepatic mono cell cultures.....	9
2.4.2 Liver slices.....	10
2.4.3 Organoids.....	10
2.5 Protein biomarkers for drug-induced liver injury.....	11
2.5.1 Alanine aminotransferase and its isoforms.....	12
2.6 Targeted proteomics.....	14
2.7 Sample preparation for targeted bottom-up protein analysis.....	16
2.7.1 Cell lysis with detergents.....	17
2.7.2 Gel electrophoresis.....	17
2.7.3 Denaturation.....	18
2.7.4 Reduction and alkylation.....	19
2.7.5 Enzymatic digestion.....	20
2.7.6 Sample clean-up.....	21
2.7.7 Bicinchoninic acid (BCA) assay for total protein determination.....	22
2.8 Chromatographic separation.....	23
2.8.1 Nano-liquid chromatography for downscaling.....	24
2.9 Mass spectrometric detection.....	25
2.9.1 Triple quadrupole mass spectrometer.....	25
2.9.2 Electrospray ionization and nanoelectrospray.....	27
2.10 MRM assay development for absolute quantitation.....	29

2.11	Aim of study	30
3	Experimental	31
3.1	Software, online tools and databases	31
3.2	Chemicals, materials, and equipment	31
3.3	Spectrophotometric determination of total protein.....	33
3.4	Sample preparation for protein samples	34
3.4.1	Protein precipitation	34
3.4.2	In-solution digestion.....	34
3.4.3	Gel electrophoresis	35
3.4.4	In-gel digestion.....	36
3.4.5	Peptide desalting	37
3.5	Preparation of peptide standard solutions.....	38
3.6	Liquid chromatography-mass spectrometry platform	39
3.6.1	Sample run conditions	40
3.7	Software settings.....	41
3.7.1	Peptide and MRM selection criteria - Skyline settings	41
3.7.2	MRM transitions	42
3.8	Elution time prediction	44
3.9	Collision energy optimization.....	44
3.10	APAP- and NAPQI induced DILI in hepatic organoids.....	45
3.11	Statistics	45
4	Results and discussions	47
4.1	The selection of a suitable biomarker.....	48
4.2	Platform performance optimization with serum albumin.....	48
4.2.1	Gradient optimization.....	52
4.2.2	Collision energy optimization	55
4.2.3	Retention time prediction	56
4.3	The investigation of alanine aminotransferase isof. 1	57
4.4	Quantification using signature peptide – LLVAGEGHTR.....	63
4.4.1	Considerations with quantification.....	64
4.4.2	MRM transition qualifier- and qualifying ion.....	65
4.5	ALT1 in biological samples	70
4.5.1	The presence of ALT1 in organoids.....	70

4.5.2	APAP- and NAPQI-induced ALT1 release in hepatic organoids	71
4.6	Experimental achievements – A summary	73
5	Concluding remarks and further work	74
6	References	75
7	Appendix	81
7.1	Supplementary theory	81
7.1.1	Molecular structure of amino acid	81
7.1.2	Protein structure	82
7.1.3	Plots	83
7.1.4	SSRCalculator	84
7.2	Websites and downloads	85
7.3	Dilutions of peptide and protein standards	85
7.4	Raw data and calculations	88
7.4.1	BCA-assay with NanoDrop measurements	89
7.4.2	Gel electrophoresis	91
7.4.3	Chromatographic data	92
7.4.4	Regression analysis	98
7.4.5	Chart data	99
7.4.6	Statistics	102
7.4.7	Detection attempt of ALT1 standard	107

1 Abbreviations

ABC	Ammonium bicarbonate
ACN	Acetonitrile
ALP	Alkaline phosphatase
ALT1	Alanine aminotransferase isoform 1
ALT2	Alanine aminotransferase isoform 2
APAP	Acetaminophen
APAP-ILI	Acetaminophen-induced liver injury
ATP	Adenosine triphosphate
BCA	Bicinchoninic acid
BLAST	Basic local alignment search tool
BSA	Bovine serum albumin
C	Carbon
CID	Collision-induced dissociation
CYP	Cytochrome P450
DC	Direct current
DILI	Drug-induced liver injury
DMSO	Dimethyl sulfoxide
DNA	Deoxyribonucleic acid
DTT	dithiothreitol
ESI	Electrospray ionization
FA	Formic acid
FBS	Fetal bovine serum
FDA	Food and Drug Administration
FWHM	Full width at half maximum
GSH	Glutathione

HSA	Human serum albumin
IAM	Iodoacetamide
ID	Inner diameter
iPSCs	Induced pluripotent stem cells
LC	Liquid chromatography
<i>m/z</i>	Mass to charge ratio
MP	Mobile phase
MRM	Multiple reaction monitoring
MS	Mass spectrometry
NAD	Nicotinamide adenine dinucleotide
NAPQI	N-acetyl-p-benzoquinone imine
NIH	The national institute of health
NIST	National Institute of Standards and Technology
PCLS	Precision cut liver slices
PSCs	Pluripotent stem cells
RF	Radio frequency
ROS	Reactive oxygen species
RP-HPLC	Reversed-phase high performance liquid chromatography
SDS-PAGE	Sodium dodecyl sulfate polyacrylamide gel electrophoresis
SP	Solid phase
SPE	Solid-phase extraction
SRC	Sample run condition
SRM	Selected reaction monitoring
TFA	Trifluoroacetic acid
TQ	Triple quadrupole

2 Introduction

2.1 The drug development process

Drug development is the process of bringing a new pharmaceutical drug to the market. According to the US Food and Drug Administration (FDA), the drug development process is comprised of 5 steps as illustrated in **Figure 1**, where each step contributes to an end-product with thorough efficacy- a. This process is most often initiated by the discovery of a new drug target. A drug target is an endogenous molecule, usually a protein that is intrinsically associated with a specific disease process. When addressed by the correct chemical entity, a desired therapeutic effect can be produced [1].

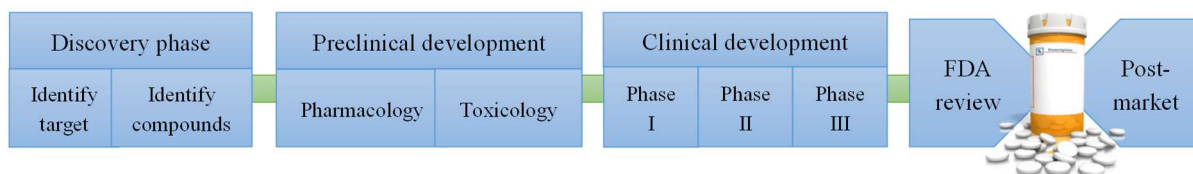


Figure 1: Overview of the drug development process.

Further investigation is driven by the search for lead compounds that could become that chemical entity. High throughput screening followed by optimization and modification of drug candidates with therapeutic activity (lead compound optimization) is the prevailing approach here [2]. The lead compound(s) is tested *in-vitro* and in animal models for pre-clinical pharmacology- and toxicology studies. The core battery of toxicology studies includes the assessment of effects on the cardiovascular system, central nervous system, and the respiratory system [3]. The preclinical developmental phase aims to provide sufficient information about the toxicological and pharmacological profile of a potential drug candidate to ethically justify its administration in human subjects [4]. Clinical drug development is separated into three phases, where the enrollment of trial subjects and the study's complexity increases with each phase.

Up to 15 years can pass from the discovery of a new drug target to the granting of market authorization for the finalized drug. The safety information which is collected during pre-marketing phases is inevitably incomplete. Thus, spontaneous reporting of adverse drug reactions from consumers or health care professionals are constantly evaluated to reassess the

risk-benefit balance of the drug. If the risks, at some point, outweighs the health benefit, access restrictions or even market withdrawals are initiated [5].

2.1.1 Currently faced challenges in drug development

The use of animal models in preclinical testing is a controversial topic. Existing models are constantly challenged by publications demonstrating their inability to recapitulate human drug responses [6, 7]. The pharmaceutical industry is in desperate need to implement better cell models that can gradually subside the use of animal models.

Figure 2 illustrates the percentage of drug candidates that complete respective phases of clinical trials. Having only a 22% success rate puts enormous financial pressures on the pharmaceutical industry and thousands of patients enrolled in these trials are not treated with an effective drug. Expediting the termination of failed drugs to earlier stages in drug development could potentially solve these issues and most importantly put fewer patients at risk.

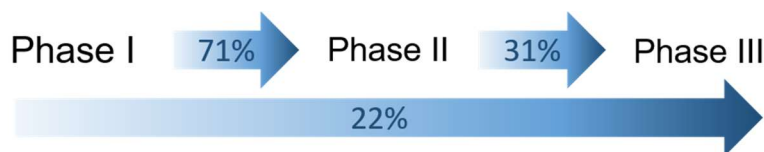


Figure 2: Percentage of successful clinical trial phases. Information was retrieved from [8].

Careful attention must be paid towards the compelling prevalence of a specific cause of late-stage drug attritions and withdrawals. Safety issues related to the hepatic system make up a bulk of late-stage drug terminations in development [9, 10]. In the years between 1900 and 2005, a total of 34 drugs were withdrawn from major markets and the majority of these drugs were withdrawn due to incidents of drug-induced liver injury (DILI) [11]. A systematic review from the FDA in 2009 shows that DILI has been the most frequent single cause of safety-related drug marketing withdrawals in the last 50 years [12].

One might ask why this alarming number of drug withdrawals are attributed to DILI, and why the liver is a particularly vulnerable organ in drug consumption. It is also important to identify where the drug development process fails to detect this serious patient risk. Understanding liver physiology and how the liver interplays with the drug and other organs when consuming a drug can help shed light on these queries.

2.2 The role of the liver in drug metabolism

2.2.1 Liver physiology, histology, and blood supply

The liver is one of five vital organs in the human body and serves a plethora of functions including the support of metabolism, immunity, digestion, vitamin storage, and detoxification [14]. It is a highly perfused organ, receiving both oxygen-rich blood through the hepatic artery from the heart and nutrient-dense blood through the hepatic portal vein from the small intestine/duodenum. Blood that is transferred away from the liver enters the heart and is pumped throughout the systemic cycle (**Figure 3**). This unique blood supply is what causes the so-called “first-pass effect”, which is experienced by pharmaceuticals being administered orally and absorbed from the intestine. For the drug to enter the systemic cycle, it must first pass the liver. The liver thereby acts as a guard to protect from potential hazardous compounds from being distributed throughout the body [15]. More on this topic in an upcoming section.

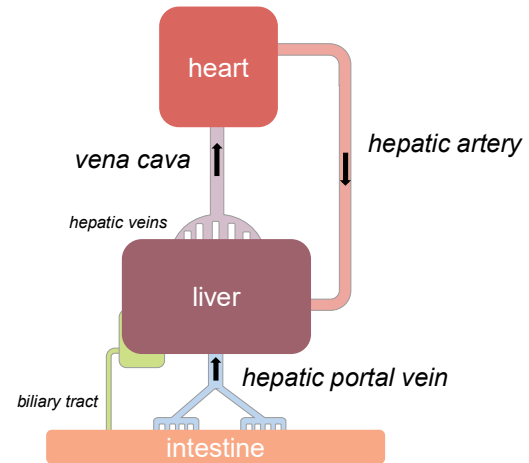


Figure 3: Overview of the liver's dual blood supply. Oxygen-rich blood is received from the heart and nutrient-rich blood is received from the intestine. Adapted from [13].

The liver has an intricate architecture defined by hexagonally shaped units called hepatic lobules arranged around veins and arteries for optimal blood perfusion (**Figure 4A**). Each hepatic lobule is constructed from smaller units with distinct morphology comprised of several cell types (**Figure 4B**). The parenchymal cells or the “working cells” of the liver are the hepatocytes, which principal responsibility is the metabolism of drugs. The remaining cells make up the stroma and provide mechanical and nutritional support [16]. Blood from the portal vein mixes with blood from the hepatic artery and drains to the central vein. The hepatocytes absorb substances from the bypassing blood, metabolizes them, and excretes the metabolites back into the blood, or into the bile.

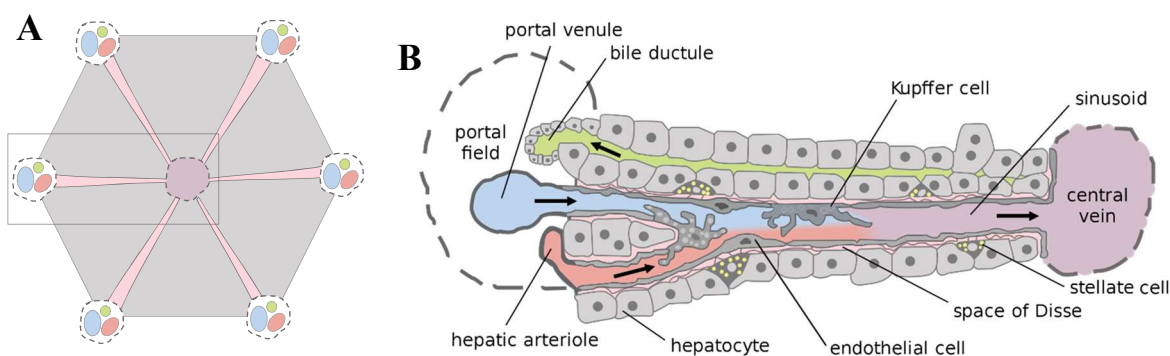


Figure 4: A schematic illustration of the hepatic lobule with its different compartments and cell types. Blood from the portal vein mixes with blood from the hepatic artery and drains to the central vein. *The left side image was created by the author of this document, and the right side image has creative commons license and was retrieved from Bing images.*

2.2.2 Drug metabolism

Pharmaceutical drugs are exogenous compounds and are thereby recognized as foreigners to the body. The body's natural defense system initiates a variety of reactions, depending on the nature of the drug, so that the elimination of the foreign body is facilitated. As already implicated, the liver is the principal site for drug metabolism. All drugs go through some degree of metabolism which is correlated to some degree of excretion. The excretion of an orally administered drug is mainly handled by the liver and its enzymes through a process called biotransformation. This process is divided into phase I and phase II reactions which can happen simultaneously, sequentially, from Phase I to Phase II or isolated (rarely the case for Phase II) [17]. Phase I reactions are catalyzed by the cytochrome P450 (CYP) enzymes and involve the formation of reactive species with the introduction or unmasking of a polar entity [18]. Phase II reactions are catalyzed by a variety of enzymes and commonly involves the addition of a larger polar group. Most drugs are inactivated by biotransformation and lose their efficacy, while others enhance their potency. The latter is referred to as prodrugs [19].

In being responsible for metabolizing many drugs, the liver is also at a correspondingly high risk of exposure to toxic drug metabolites. The liver is, in fact, the prime target for drug-induced injury [20]. This is part of explaining the large number of drug withdrawals attributed to DILI. The mechanism of action for DILI is generally defined by either idiosyncratic or intrinsic reactions. The next section will elaborate on this.

2.3 Drug-induced liver injury

DILI can be categorized as idiosyncratic or intrinsic based on its mechanism of toxicity. Idiosyncratic reactions are characterized by occurring in a minority of patients, with an unpredictable time of onset after drug consumption. They are characterized by unpredictability regarding dose-dependency and seem difficult to reproduce in animal models [21]. Idiosyncratic DILI can mimic many liver disorders in terms of clinical symptoms, which make them more difficult to distinguish from non-drug related liver diseases [22]. In recent years, new insights in idiosyncratic DILI has allowed for novel associations to be made with its mechanism of action [23]. Idiosyncratic DILI is characterized as having low incident rates of approximately 1 in 10 000. This causes it to often bypass detection in clinical trials and harm patients who are being prescribed the drug post-marketing authorization. It is therefore strongly desired to implement *in vitro* models in drug development that can reduce this patient risk.

Intrinsic DILI is more manageable in drug development as it shows a clear dose-dependency [21]. Its toxicity is reproducible in preclinical models and outcomes can be extrapolated to humans. Intrinsic DILI-causing agents seem to exert toxicity through three main mechanisms: (1) mitochondrial dysfunction, (2) oxidative stress, and (3) alternations in bile homeostasis. Mitochondrial dysfunction is the result of the toxic agent inhibiting mitochondrial ATP production. A temporary or permanent cessation in ATP production will eventually cause the cell to shut down. Oxidative stress occurs with the formation of reactive oxygen species (ROS), which when exceeding their rate of detoxification can cause organelle damage. Lastly, DILI causing drugs can interact with bile acid efflux pumps, leading to the intracellular accumulation of toxic bile acids [21, 24]. A classic example of an intrinsic hepatotoxin is acetaminophen (APAP), which is the active ingredient in the analgesic drug Paracet[®]. APAPs toxicity profile is represented by an interplay of all the above-mentioned mechanisms.

2.3.1 Acetaminophen-induced liver injury

APAP accounts for nearly 50% of adult acute liver failures in the US and is the prevailing cause of DILI [25]. Mechanism of APAP induced-hepatocyte necrosis has been depicted in **Figure 5**. The majority of APAP is metabolized by phase II enzymes (glucuronidation and sulfate conjugation) and excreted through the kidneys. A fraction of APAP is acted upon by the CYP P450 enzyme family, mainly by CYP2E1 and CYP1A2, and metabolized into the highly

reactive N-acetyl-p-benzoquinone imine (NAPQI). The antioxidant glutathione (GSH) detoxifies NAPQI, but when concentrations exceed a critical threshold, GSH stores are depleted and NAPQI is accumulated in the cell [26, 27]. Free NAPQI covalently binding to mitochondrial proteins, causing ATP cessation and ROS formation. The initiation of ROS formation cascades into a set of protein translocations between cytosol and mitochondria, eventually leading to the fragmentation of nuclear DNA and programmed necrosis (alternative form of apoptosis) [27]. Although this mechanism only describes hepatocyte cell death, secondary mechanisms include activation of non-parenchymal cells, which emphasizes the importance of in-vitro models with multiple cell types [27].

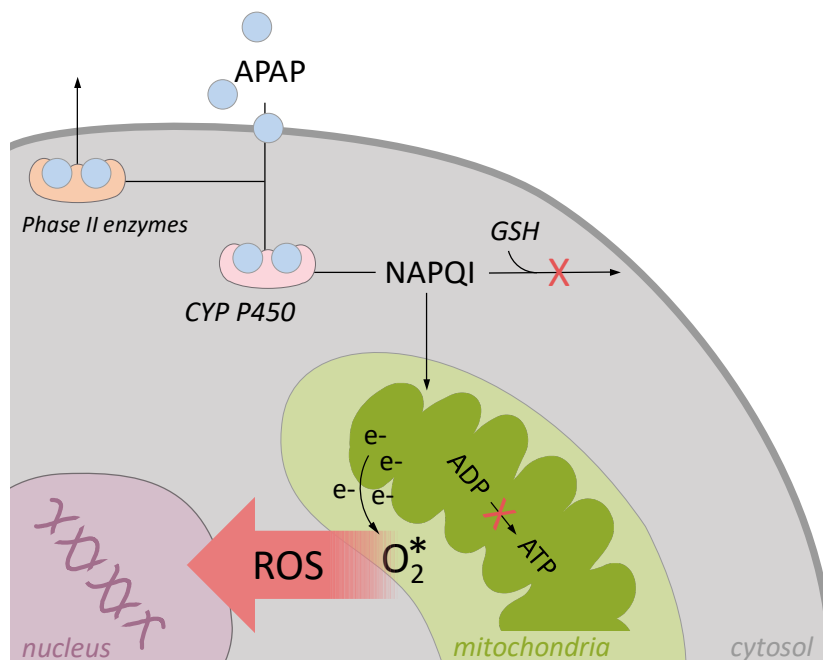


Figure 5: Mechanism of APAP induced-hepatocyte necrosis. The majority of APAP is metabolized by phase II enzymes for renal excretion, while a fraction is acted upon by CYP P450 enzymes into the toxic metabolite NAPQI. Upon GSH depletion, NAPQI disrupts mitochondrial respiration which causes ROS formation and DNA fragmentation. *The figure has been created by the author of this document and is based on information retrieved from [26, 27].*

Figure 6 illustrates the important differentiation of the two types of cell death. Whereas apoptosis takes place as an encapsulation of cellular contents, necrosis causes membrane rupture and the release of cellular contents [28, 29]. Measurements of different substances in

these cellular contents can be utilized to detect APAP-induced liver injury (APAP-ILI). This topic will be discussed in an upcoming section.

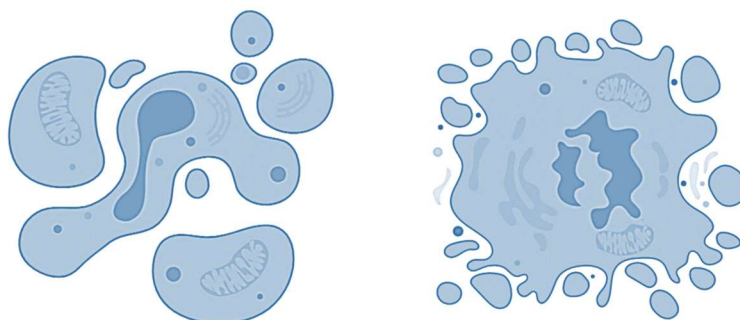


Figure 6: Cell apoptosis (left) vs cell necrosis (right). Cell apoptosis takes place as an encapsulation of cellular contents while cell necrosis causes membrane disruption and the release of cellular contents. *The illustration has been created with BioRender.com*

2.4 *In vitro* models applicable for preclinical liver safety assessment

There is an increasing interest to gradually replace animal-based models with cell-based models and implement these in the preclinical safety assessment of drugs. This is, of course, beneficial from an ethical perspective, but is also hoped to strengthen the extrapolation of preclinical findings to human. It is, however, important to recognize that cell-based models probably never will reproduce all functions of an intact living organism and that assumptions and extrapolations from animals to humans will continue to influence decision making in drug development [30].

2.4.1 Hepatic mono cell cultures

Hepatic mono cell cultures are two-dimensionally seeded cells of a single cell type derived from an immortalized or primary liver source. Immortalized cells are ‘immortal’ in the sense that they are not subjected to apoptosis, also called programmed cell death [31]. The HepG2 cell line is the immortalized representative for the liver and is commonly implemented as a part of DILI-assessment [32-34]. The advantage of using HepG2 is their availability, ease of handling, and inter-donor consistency. The latter being responsible for a stable cell expression. HepG2 cells maintain some functions of *in vivo* hepatocytes but are rather considered a helpful

supplementary tool than a true representation of the liver [8, 35]. An upgrade from HepG2 are the primary hepatocytes, which are considered the gold standard in toxicity assessment and have even shown to elucidate previously unknown mechanisms of DILI [35]. They are directly isolated from liver tissue, hence closely representing *in vivo* conditions. General downsides are the high costs and labor intensiveness, alongside undisputable inter-donor variability [35].

Hepatic mono cell cultures have left their mark in preclinical safety assessment but have also faced controversy by the fact that intercellular interactions are completely disregarded. This is especially prominent, considering that studies have demonstrated such intercellular interactions to take play in drug metabolism [36].

2.4.2 Liver slices

A way of incorporating non-parenchymal cells is with the implementation of precision-cut liver slices (PCLS). Being cut directly from a healthy or diseased liver, they have the advantage of maintaining the multi-cellular architecture of the hepatic environment. PCLSs have yet to become commercialized and this may lay in the far future, but it has been recognized as a promising tool to advance DILI assessment [37]. The co-culturing of PCLS with blood components has for example shown to recreate some immunological behavior. An interesting implementation of PCLS has been demonstrated by Midwoud et al., who utilized continuously perfused PCLS in an online liquid chromatography system with UV detection to monitor drug metabolism [38]. Limitations to this model are the access to freshly resected liver, inter-donor variability, and increasing system complexity [37].

2.4.3 Organoids

When life is created, a few-celled embryo develops into a complex human, being puzzled together from over 200 different cell types. The driving force for this cell differentiation is the pluripotency of the embryonic stem cells [39]. The ability of stem cells to differentiate into virtually any cell type is a remarkable feature that also has been implemented into advanced cell-based models called organoids.

Organoids, as defined by Lancaster et al. are multiple organ-specific cell types, derived from pluripotent stem cells (PSCs) or organ progenitors, which are spatially organized through self-assembly similarly to the organ it emulates. As per definition, it is also required to recapitulate

some specific functions of the organ [40]. Going forward, the use of the term ‘organoid(s)’ will refer to this definition. Three main steps are described in the formation of organoids: (1) PSC differentiation, (2) cell sorting out, and (3) spatially restricted lineage commitment. Cell sorting out is believed to arise when cells with similar adhesive properties compartmentalize to form an energetically favorable pattern, while lineage commitment is an internal cell-fate decision that leads to the final arrangement and maturation of the cells [40]. In 2006, Yamanaka et al. offered a major

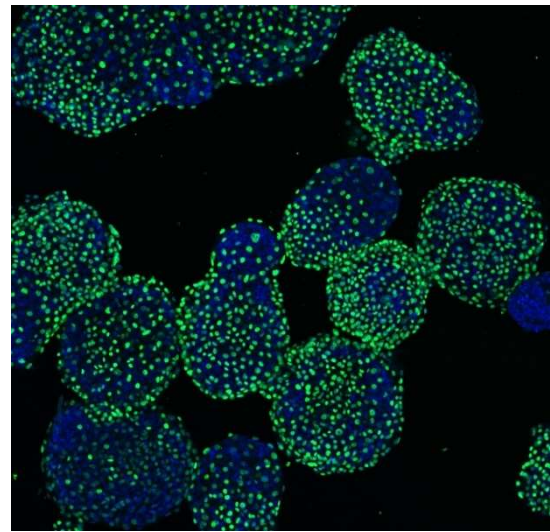


Figure 7: Wholemount immuno-fluorescence pictures of hepatic organoids. The green color (HNF4a hepatocyte marker expression) shows the cell nuclei. *The image was kindly provided by PhD Sean Harrison at the lab of Rikshospitalet.*

contribution to the evolution of organoids with their pioneering work on induced pluripotent stem cells (iPSCs). This meant that already differentiated cells, e.g. skin cells, could be reprogrammed (induced) into an embryonic-like state before being differentiated to the desired cell type. This overcomes the limitation to only use embryonic or adult stem cells, that are of high cost and limited access.

Hepatic organoids (**Figure 7**) are useful in a plethora of applications such as disease modeling and seem very promising as a platform for drug screening and toxicity testing [41]. Being a young field of research, efforts are still made to understand all aspects of liver organoids and how well they emulate liver physiology. For this thesis, hepatic organoids will be the cell model of choice for toxicity assay development with protein biomarkers.

2.5 Protein biomarkers for drug-induced liver injury

The National Institute of Health (NIH) has defined biomarkers as biological characteristics that are objectively measured and evaluated as indicators of normal biological processes, pathogenic processes, or pharmacological responses [42]. One such “biological characteristic” are proteins; these are a popular choice as they can be quantified by a variety of analytical methods. The pathogenic processes of DILI are multi-faceted and have a large clinical spectrum represented

by a comprehensive list of protein biomarkers. Dividing the biomarkers into biomarkers of disease mechanism and biomarkers of injury can be helpful in orientation, although there is some overlap between the groups.

Biomarkers of disease mechanism are indicators for the underlying biochemical event that has led or contributed to the injury or disease [43]. This is a great advantage, given that protein expression from disease mechanism can offer a predictive utility, so that signs of toxicity can be detected early on in drug development. Another advantage is the biomarkers' intracellular origin, which circumvents the inclusion of e.g. blood components for the implementations in *in vitro* liver models. Mechanistic biomarkers have been discovered for cell death, oxidative stress, mitochondrial damage, and immunological response. Many are still in the discovery phases and have yet not been properly validated [43]. A challenge with some mechanistic biomarkers is their reliable detection. If the biomarker is not released into the intracellular space upon exposure to a toxic compound, intentional disruption of the cell (*in vitro* liver model) must be performed to access the analyte. This may induce cellular stress responses and result in a potential upregulation of the biomarker in question.

The biomarkers of liver injury are commonly directly associated to the cell injury. This is, for example, the case for the membrane protein alkaline phosphatase (ALP). Animal studies suggest that, upon biliary obstruction, ALP is solubilized and released into the extracellular space due to the accumulation of bile salts [44, 45]. Alanine aminotransferase is another commonly featured liver injury biomarker, which will be discussed in more detail below.

2.5.1 Alanine aminotransferase and its isoforms

Alanine aminotransferase (ALT) has a long history in clinical diagnostics and is traditionally measured as increased plasma concentrations in DILI suspect patients. Increased plasma levels are caused by hepatocyte injury, where an increase in cell membrane permeability or a complete compromise of cell membrane integrity (necrotic pathway), causes the cell contents to leach out into the extracellular space, and thereafter into the plasma [46].

ALT is the enzyme that catalyzes the conversion of L-alanine and 2-oxoglutarate to pyruvate and L-glutamate (**Figure 8**) with the concomitant reduction of NAD⁺ to NADH (not shown). This mechanism plays part in muscle cell/hepatocyte interchange for muscle cell nitrogen elimination and energy replenishment [45, 47, 48].

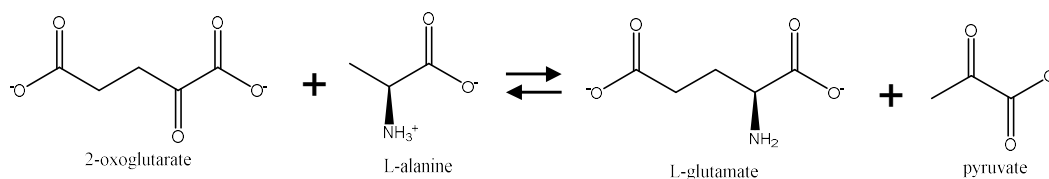
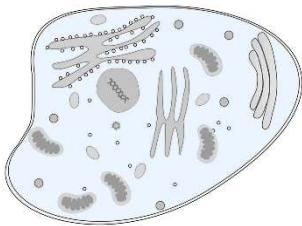
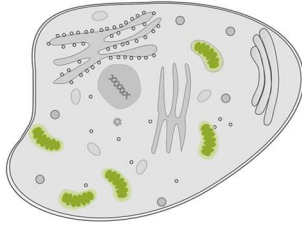


Figure 8: Chemical reaction for the conversion of L-alanine and 2-oxoglutarate to L-glutamate and pyruvate.

ALT has two isoforms (I and II) with identical catalytic activity and capacity. ALT isoform 1 (ALT1) is primarily found in the liver but is also expressed in small amounts in the kidney, heart, and skeletal muscles [48]. ALT2 is expressed at high levels in muscle, adipose tissue, kidney, and brain [45]. **Table 1** presents a summary of the respective isoforms. It is ALT1 that is considered a biomarker for DILI, as its primary location is the liver cytosol.

Table 1: Summary of protein characteristics for ALT1 and ALT2. The information was obtained from the Uniprot DB [45, 48]. *The embedded figures have creative commons license and have been edited for this overview.*

Isoform	1	2
Subcellular location		
Length (amino acid residues)	496	523
Size (Da)	54 637	57 904
Expression in	liver (highly expressed), kidney, heart, and skeletal muscles	high levels in muscle, adipose tissue, kidney, and brain
Sequence identity of ALT1 (%) ¹	100	69
Catalytic activity	Conversion of L-alanine and 2-oxoglutarate to pyruvate and L-glutamate	

¹ Obtained from performing BLAST (Basic Local Alignment Search tool) analysis for ALT1 (P24298) and ALT2 (Q8TD30). Result file in **Appendix, Figure 53**.

The use of ALT as a biomarker for DILI is often criticized as having unsatisfactory specificity towards the liver. That is, in fact, a rightful argument if both isoforms of the protein are measured. Common ALT liver function tests measure the catalytic activity by quantifying the amount of NAD⁺/NADPH that is produced. These tests are non-isoform specific, given that both isoforms have identical catalytic activity and capacity. However, as previously implicated, it is ALT1 that is specific towards the liver and can distinguish hepatic from extrahepatic injury [49]. One way this obstacle can be overcome is by the implementation of targeted proteomics. In short, this can be described as mass spectrometry (MS)-based protein quantification to detect proteins of interest [50]. The main advantage of targeted proteomics is the ability to tailor the method for specific needs, like in this case, to selectively measure each isoform. Once a method is developed, it can easily be extended to several proteins, which opens the opportunity to measure entire biomarker profiles. Biological matrices are often complex and MS detection is therefore preferably combined with an online separation step, like liquid chromatography (LC).

The steps towards a finalized targeted proteomics method will be described in detail in the last section of this introduction.

2.6 Targeted proteomics

The term targeted proteomics covers several mass spectrometry (MS)-based methods, where the main distinction is drawn between the top-down and the bottom-up approaches. Both approaches are visualized in **Figure 9**. In top-down proteomics, the proteins are injected into the instrument in their intact form before being dissociated into fragments that add up to the total mass of the protein. The main advantage of this approach is that all information, including mutations and post-translational modifications, related to the intact protein, is preserved. The disadvantages, it that the diversity in the proteins physicochemical properties complicate front-end sample preparation and the current state of software for back-end data interpretation lacks the advancement needed for reliable quantification [51]. Current efforts have also been limited to proteins smaller than 50 kDa [52]. The bottom-up approach overcomes a lot of the hurdles associated with top-down proteomics and is the preferred approach for targeted proteomics. Here, the proteins are subjected to proteolytic cleaving at specific cleavage sites and shorter amino acid sequences called proteolytic peptides are formed. It is these peptides that are analyzed downstream. Although the complexity of the sample is increased, the equalization of the physicochemical properties that is obtained from proteolytic cleavage generally simplifies

front-end handling and back-end data interpretation. Bottom-up analysis offers increased MS sensitivity, improved ionization in the LS-MS interface, and is accompanied by well-established software to rebuild or quantify the target protein [53]. In this thesis, a bottom-up approach was implemented.

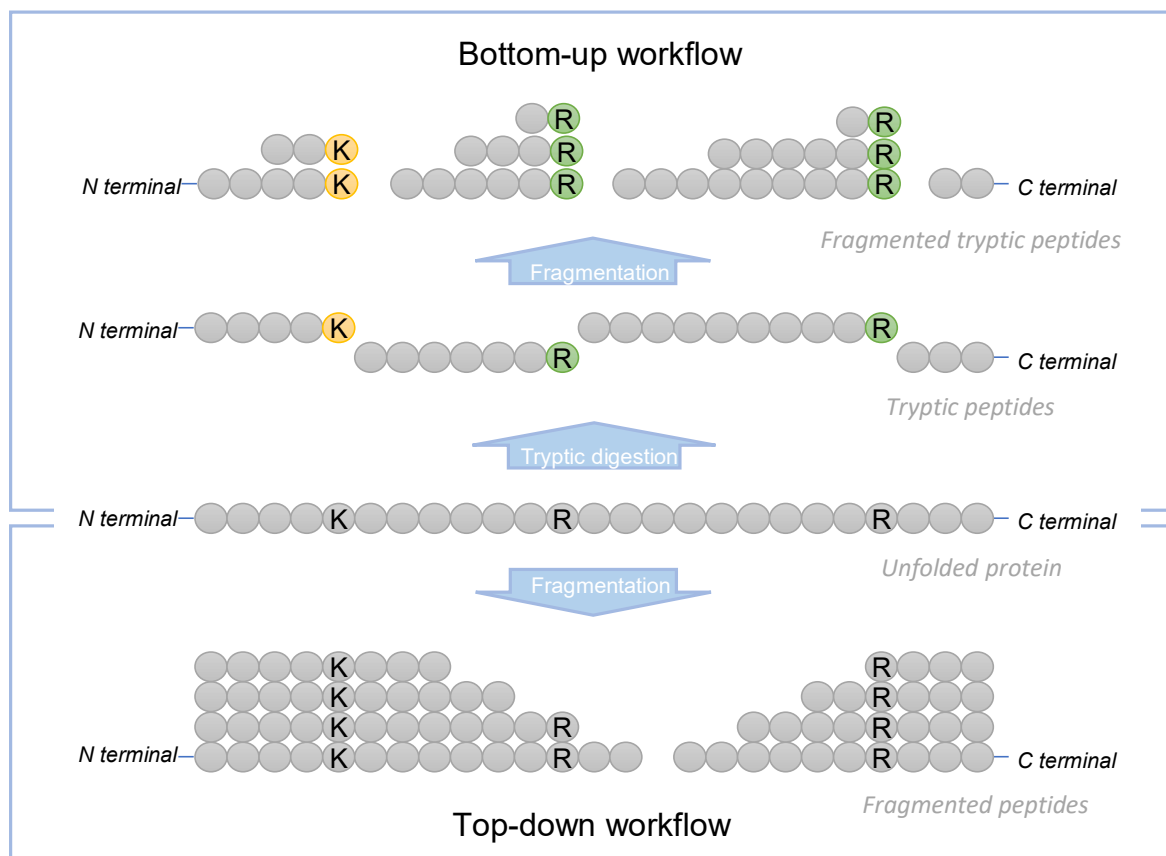


Figure 9: Illustration of bottom-up and top-down proteomics. *The figure has been created by the author of this document and was adapted from [54].*

The only way to target proteins?

Proteins may also be targeted through a process called immunoblotting. It is a non-spectrometric approach, where the determination of specific proteins is performed with the use of antibodies with an exclusive affinity towards the targeted protein. Detection then proceeds with chemiluminescent visualization with digital imaging equipment [55]. The consensus is that, although useful for fast protein detection, the quantitative data that is produced is of

considerably lower quality, in regards to detection sensitivity and reliability compared to spectrometry-based approaches [56].

2.7 Sample preparation for targeted bottom-up protein analysis

The sample preparation for targeted bottom-up analysis includes the in-gel or in-solution digestion of proteins. In both of these, the proteins are unfolded, stabilized in the unfolded position, and cleaved by a proteolytic enzyme. In-gel digestion is most often performed following a prefractionation by gel electrophoresis based on the size of the intact proteins. This step is commonly performed with sodium dodecyl sulfate polyacrylamide gel electrophoresis (SDS-PAGE).

The type of digestion to perform is dependent on the complexity of the sample. While in-solution digestion is more time and labor efficient, in-gel digestion (after e.g. SDS-PAGE) allows for the depletion of high abundance proteins that potentially interfere with analyte detection. The main disadvantage with in-gel digestion is the loss of sample during sample preparation, which might influence method detection limits. The flow chart in **Figure 10** describes the typical workflow for targeted proteomics sample preparation. The blue squares will be described in more detail in this section. It is also common to include a step for the estimation of the total protein content of the sample, which is typically included before the enzymatic digestion. The determination of the total protein content with bicinchoninic acid will also be described in this section.

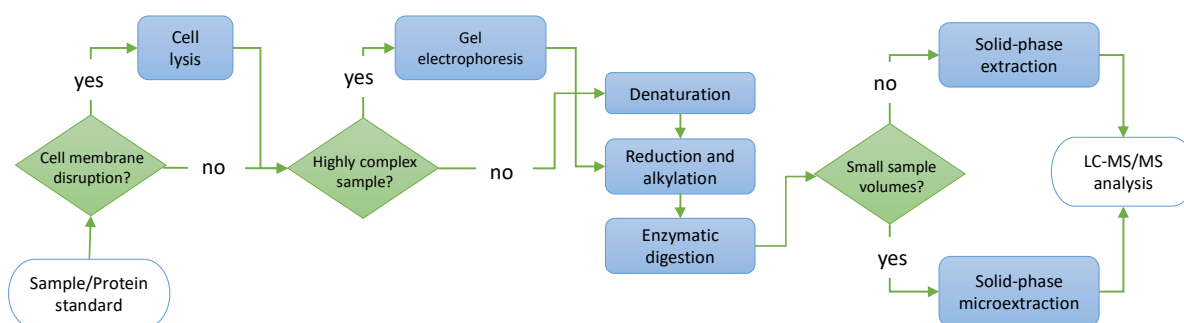


Figure 10: Flowchart of sample preparation for targeted proteomics. The start- and endpoint is depicted as white ovals.

2.7.1 Cell lysis with detergents

Cell lysis is the process of cell membrane disruption, which in the context of protein analysis, has been utilized to access proteins localized in the interior of a cell or other cell-like encapsulations. Cell lysis can be executed in a variety of ways but has in recent years progressed towards the use of chemical detergents/surfactants. The aliphatic nature of detergents enables them to interact with the phospholipid bilayer of the cell membrane which eventually compromises the cell membranes' integrity [57].

The number of chemical detergents is endless, allowing this step to be highly customizable depending on the cell type, protein identity, or method of analysis. SDS, due to its aliphatic nature and negatively charged head, is a popular choice, as it both acts as a detergent for cell lysis and as a denaturing agent in SDS-PAGE. The chemical structure of SDS is presented in **Figure 11**.

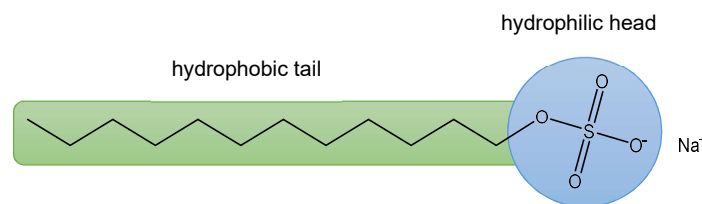


Figure 11: Chemical structure of sodium dodecyl sulfate (SDS). The green area is hydrophobic, and the blue area is hydrophilic

2.7.2 Gel electrophoresis

Gel electrophoresis was originally intended for the fractionation of nucleic acids (DNA fragments), but its use has been extended to other macromolecules like proteins. In in-gel electrophoresis with SDS, the proteins applied to a porous polymer (gel) are separated by moving through an electric field at different velocities depending on the size of the protein [58].

The velocity is given by the equation,

$$v = \frac{Eq}{f} \quad (\text{Equation 1})$$

where v is the velocity of the proteins, E is the applied electric field, q is the net charge of the protein, and f is the frictional coefficient experienced by the proteins [58].

Before the protein sample is being applied to the gel, it is treated with SDS, which serves two main functions: (1) the non-covalent bonds of the native protein structures are broken and (2) SDS binds to the side chains of the amino acids giving the proteins an overall negative charge. SDS masks the charge normally present and equalizes the charge between proteins. The negative charge enables the proteins to move in the direction of the electric field but does not affect the velocity at which the proteins travel [58]. Since smaller proteins experience less frictional force than larger protein, they will travel at a greater velocity and hence separate as illustrated in **Figure 12**.

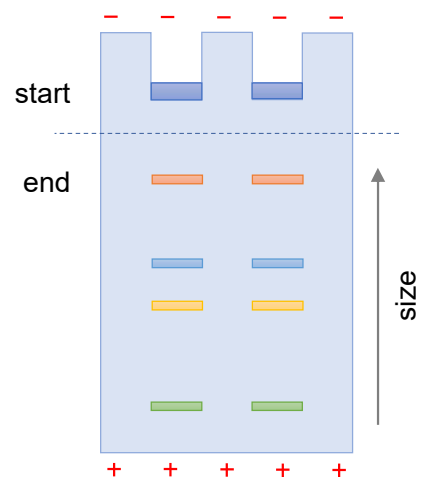


Figure 12: Proteins of different sizes separated (different colors) by SDS-PAGE. Negatively charged proteins move in the direction of the electric field. Smaller proteins move faster than larger proteins. *The figure has been created by the author of this document.*

2.7.3 Denaturation

Denaturation involves the unfolding of the native structure of the protein and is imperative for the consecutive proteolytic cleavage (**Figure 13**). Urea is the most widely used denaturant in proteomics studies and is used to increase protease efficiency in the proceeding digestion. It also promotes solubilization by preventing protein precipitation and aggregation [59]. Urea is a denaturing agent that partially or completely unravels the quaternary-, tertiary-, and secondary structure of the proteins [60]. Two symbiotic mechanisms are suggested for the unfoldment of proteins with urea: (1) A direct interaction of urea with the protein through hydrogen bonding that allows for the solvation of the hydrophobic core via the influx of water molecules and (2) a urea-mediated alteration of the water structure and dynamics, diminishing the hydrophobic effect which allows for the exposure of hydrophobic core residues [60].

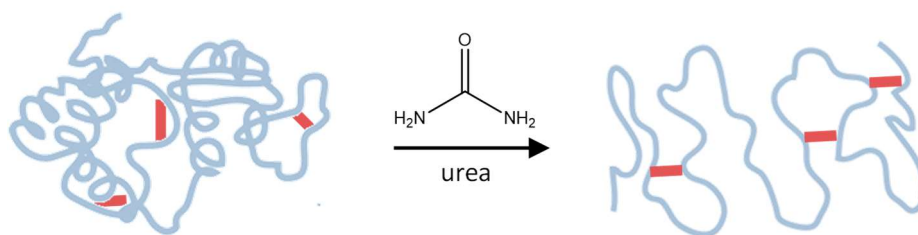


Figure 13: Denaturation of proteins with urea. The primary structure, including disulfide bonds (red lines), is preserved.

2.7.4 Reduction and alkylation

Disulfide bonds, occurring on the side chain thiol groups of two opposing cysteine residues, contribute to the stabilization of the native protein structure and regulate the catalytic activity of enzyme proteins [61]. The reduction of these sulfide bonds followed by the alkylation of the resulting free thiol groups is important for the reliable detection of peptides. **Figure 14** illustrates the hypothetical consequence of omitting the reduction and alkylation of disulfide bonds, where the targeted peptide is missed since another peptide changes its m/z value of detection.

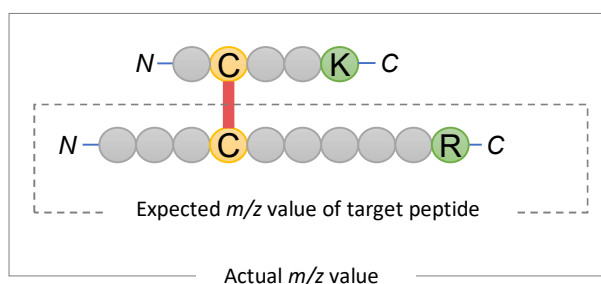


Figure 14: The consequence of omitting the reduction and alkylation of disulfide bonds (red line).

The reducing agent dithiothreitol (DTT) was introduced in 1964 as a more stable and less toxic reducing agent than its forerunners and is today one of the most frequently used in proteomics sample preparation [62, 63]. DTT is a well-suited reducing agent in proteomics sample preparation due to its rapid and complete reduction of disulfide groups. Furthermore, its great water solubility, relatively low toxicity (compared to other thiol reducing agents) and little odor makes it convenient to handle [64, 65]. The reaction mechanism of disulfide bonds by DTT is depicted in **Figure 15**.

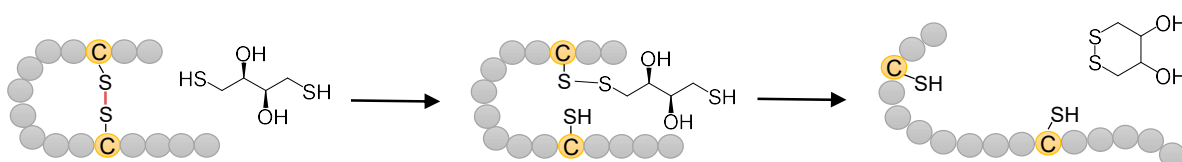


Figure 15: The reduction of a disulfide bridge between two cysteine residues by DTT. DTT forms a disulfide bond with the substrate, resulting in the formation of one thiol group. The sulfur on the opposing side of DTT attacks the sulfide bond, resulting in the ring formation of DTT and the completion of the reduction of the cysteine residues.

A reformation of the protein is prevented if an alkylation step immediately follows the reduction. Alkylation involves “capping” the catalytic cysteine residues with a nucleophile substitution (SN_2) of the thiol groups. The reaction mechanism with iodoacetamide (IAM) as the electrophile and a cysteine residue as the nucleophile attacker is represented in **Figure 16**.

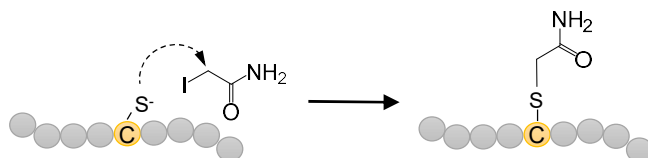


Figure 16: The free thiol groups attack carbon on IAM, resulting in the alkylation of the free thiol groups by nucleophile substitution.

2.7.5 Enzymatic digestion

The enzymatic digestion of the intact proteins enables the detection of pre-fragmented peptides by cleaving the amide bonds at specific cleavage sites. The enzyme trypsin is considered the gold standard in bottom-up targeted proteomics, especially due to its high cleavage specificity [66]. It is a serine protease that cleaves at the carboxyl side of arginine and lysine through a two-step hydrolysis. The cleavage takes place at the catalytic triad (three amino acid residues) on the active site of trypsin. The generally accepted reaction mechanism is complex but can, in short, be described as follows: The carbon of the carbonyl group of the peptide bond is attacked by the catalytic triad (nucleophilic attack) forming an aryl-enzyme intermediate and an amide which can depart from the protein. In the second step, a water molecule, assisted by the catalytic triad, attacks the carbon group of the carbonyl group and forms a carboxylic acid which releases the C-terminal of the peptide and completes the tryptic cleavage [67-69]. **Figure 17** shows the simplified reaction mechanism of the trypsin-mediated hydrolysis of amide bonds.

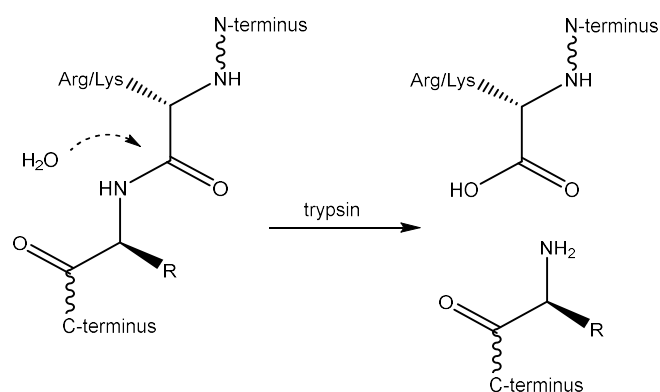


Figure 17: Simplified reaction of the trypsin-mediated hydrolysis of amide bonds on the carboxyl side of lysine and arginine. Water attacks the carbon of the carbonyl group, as indicated by the arrow, and the formation of a carboxylic acid releases the C-terminal of the peptide, completing the tryptic cleavage.

2.7.6 Sample clean-up

Salts and buffers added during sample preparation must be removed to avoid interferences with MS-detection. C18 silica-based solid-phase extraction (SPE) columns or microextraction tips (fixed C18 silica-based material in a pipette tip) are usually employed in peptide sample clean-up [70]. Microextraction is well-suited for small sample sizes and follows the same principles as conventional SPE. **Figure 18** shows the four basic steps of reversed-phase SPE. The column is conditioned with an organic solvent to activate the collapsed C18 chains and then washed with water to remove the organic solvent. The sample is then applied and compounds having Van der Waals interactions with the stationary phase are retained on the column (blue and red particles). The column is then washed with an aqueous solution, to remove unwanted hydrophilic substances, like salts (blue particles). And finally, the analytes (red particles) are eluted with an organic solvent. It is important to perform the extraction at an appropriate pH to avoid secondary ionic interactions [71].

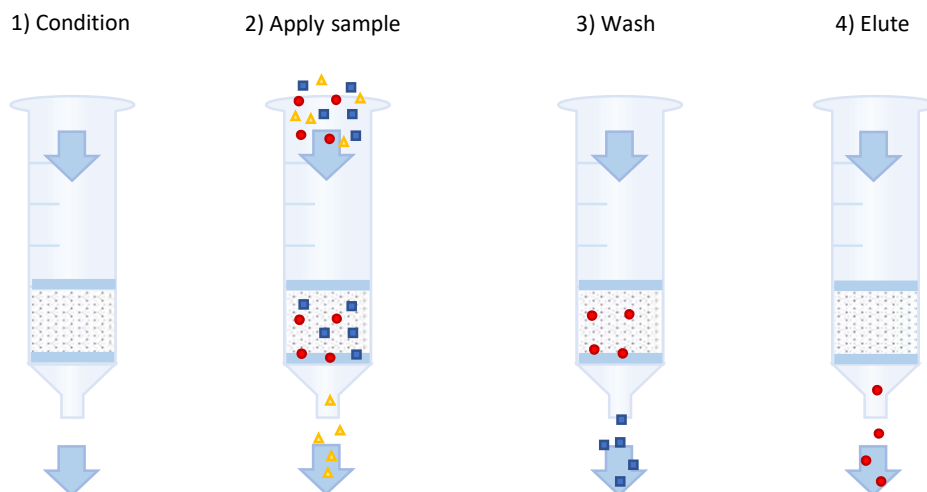


Figure 18: Solid-phase extraction in sample preparation. The column conditioned and washed, thereafter the sample is applied, and salts are removed. The remaining compounds including the analyte are eluted last. *The figure was created by the author of this document and adapted from [71]*

2.7.7 Bicinchoninic acid (BCA) assay for total protein determination

The BCA assay is a colorimetry-based method that utilizes the strong absorbance of light from a protein-BCA complex to measure the total protein concentration in a sample. The concept is based on the well-known Biuret reaction, where the reduction of Cu^{2+} to Cu^+ in the presence of proteins (peptide bonds) in an alkaline environment produces a protein/ Cu^+ complex that gives of a characteristic purple color [72].

In the BCA assay, bicinchoninic acid is added to the solution to intensify the color and thereby decrease the detection limits of the proteins. Two BCA molecules and one Cu^+ ion form a dark purple-colored chromophore with an absorbance maximum at 562 nm as depicted in **Figure 19**. The BCA/ Cu^+ complex absorbs much more strongly than the protein/ Cu^+ complex, hence intensifying the signal for colorimetric measurement. Protein quantification is obtained by constructing an external calibration curve with a standard protein source like bovine serum albumin (BSA) [73]. BCA assays are a useful implementation in a targeted proteomics sample preparation workflow to estimate the amount of trypsin added to a sample, as its cleaving efficiency is dependent on the right trypsin/protein ratio.

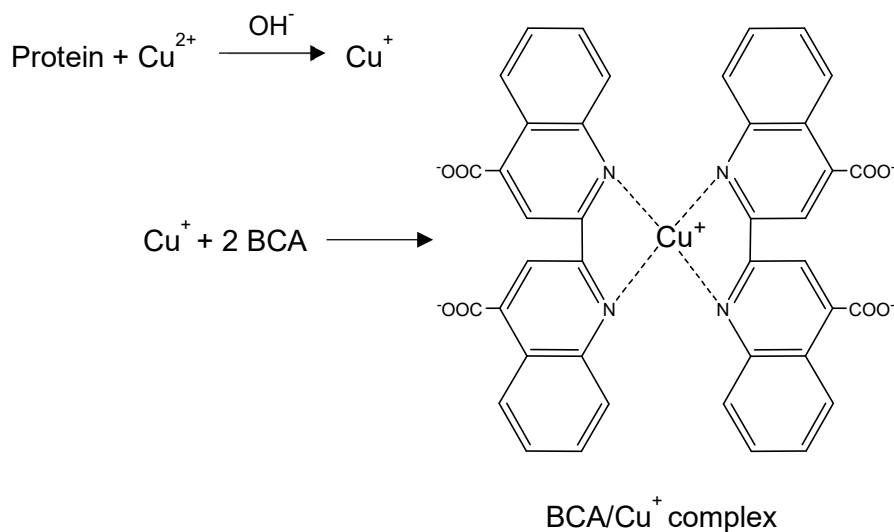


Figure 19: Mechanism of the BCA/Cu⁺ complex formation. Cu²⁺ is reduced to Cu⁺ in the presence of proteins followed by the formation of a BCA/Cu⁺ complex. Adapted from [74].

2.8 Chromatographic separation

Subjecting a biological sample to enzymatic digestion results in a complex pool of thousands of peptides. Reversed-phase liquid chromatography (RP-HPLC) plays a vital role in the separation of peptides before protein identification and quantification with mass spectrometry. Reversed-phase chromatography is a versatile and selective separation principle yielding the highest resolving capability and repeatability compared to other separation principles [75]. These separation features are especially useful for peptides similar in structure. RP-HPLC can separate peptides only differing by a single amino acid [76].

During RP-LC compounds are separated based on their hydrophobic interactions with the stationary phase (SP). More hydrophobic compounds are more strongly retained by the SP, hence eluting later than less hydrophobic compounds. Packed columns are commonly employed with RP due to commercial availability and physical robustness. The silica particles are coated with the stationary phase through chemical attachment. For RP-LC the attachment of linear, aliphatic eighteen carbon chains (C₁₈) is the most common. If however, limitations in column backpressure become an issue, columns with monolithic structures of silica can be employed for peptide separation [77].

The mobile phase is usually a mixture of water with an organic modifier and a buffer or acid. The organic modifier of choice is usually acetonitrile (ACN), because (1) it has a low viscosity, thus resulting in lower column backpressures and (2) is volatile, which is preferable when coupled to electrospray ionization (ESI). The drawbacks of using ACN are its high cost and moderate toxicity. Other organic modifiers, such as isopropanol, can sometimes be employed with very hydrophobic peptides [76].

A gradient elution, where the MP composition is steadily changed, is almost always employed when eluting peptides. Generally, it is beneficial due to the narrowing of peak width for late eluting peptides. Peptides (and proteins) have a unique adsorption/desorption mechanism which greatly benefits from gradient elution. While small molecules change retention time slowly with an increase in the organic solvent, peptide retention times change abruptly when the required concentration of organic modifier is reached, hence giving sharp peaks and increased resolution/peak capacity with gradient elution [76].

2.8.1 Nano-liquid chromatography for downscaling

Conventional LC platforms have traditionally been employed with 3-5 mm ID columns, however, great benefits come from downscaling to a nano-LC platform, where 0.01-0.1 mm ID columns are employed. The main advantage of downscaling is the significant increase in sensitivity when coupled to a concentration sensitive detector like an electrospray ionization (ESI)-MS.

The signal enhancement is attributed to the reduction in radial dilution which is directly proportional to the square of the ID, as depicted in **Figure 20**. The theoretical maximal gain in sensitivity when narrowing ID can be expressed with the downscaling factor:

$$\text{downscale factor} = d_{c1}^2 / d_{c2}^2 \quad (\text{Equation 2})$$

, where d_{c1} and d_{c2} are the ID of two columns, $d_{c1} > d_{c2}$, and the injection volume is constant [78]. The downscaling factor can also be used to calculate the downscaled linear flow rate ($\mu\text{L}/\text{min}$) in the same manner as with column ID. Lowering the flow rate leads to a reduced mobile phase consumption, which is beneficial from an environmental and economic aspect.

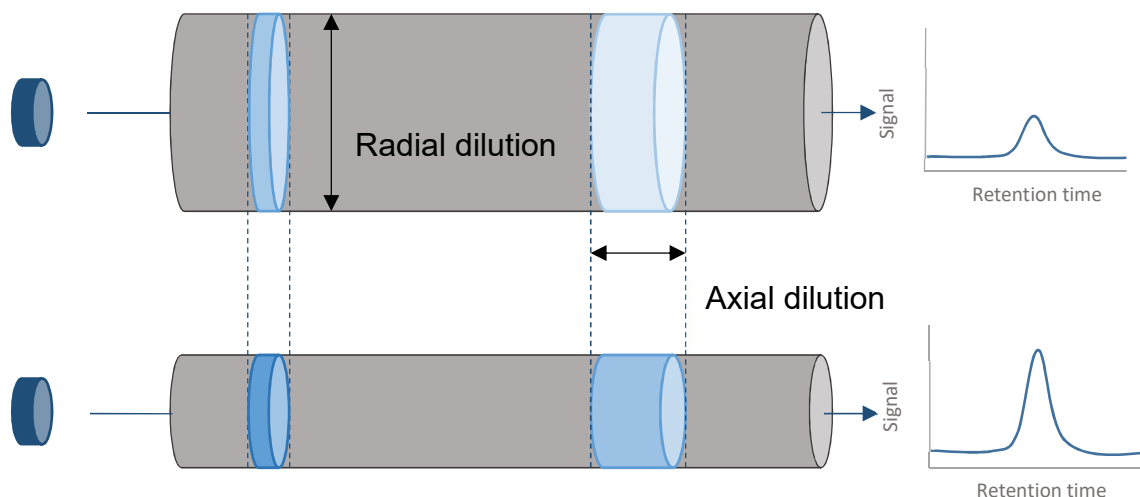


Figure 20: Downscaling the inner diameter of the column results in a reduced radial dilution which enhances analyte sensitivity. *The figure was created by the author of this document and adapted from [78]*

2.9 Mass spectrometric detection

A mass spectrometer (MS) is not only a detector but also an additional dimension of separation based on the mass to charge ratio (m/z) of the ion. It offers excellent sensitivity and selectivity, suitable for complex biological matrices. It is a favorable instrument connected to RP-LC, as the separation principles are orthogonal. The MS instrument is composed of (1) lenses and skimmers which focus the ions from an ion source into a concentrated ion beam, (2) one or several mass analyzers, which filters or transmits ions of specific m/z , and (3) a detector which measures the current induced by the ions [79].

2.9.1 Triple quadrupole mass spectrometer

The triple quadrupole (TQ) MS is a powerful instrument in peptide-based protein quantification. The TQ-MS comprises three quadrupoles, where Q1 and Q3 operate as mass analyzers, while Q2 is used for ion transfer or ion fragmentation (**Figure 22**). A single quadrupole consists of four hyperbolic or cylindrical rod electrodes extending in the z -direction and are assembled in a square configuration in the xy -plane, as illustrated in **Figure 21**. A direct current (DC) voltage and a

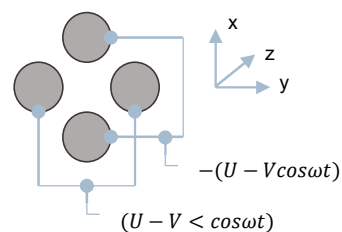


Figure 21: The quadrupole unit of a triple quadrupole mass spectrometer. Opposing rods have the same applied potential.

radio frequency (RF) voltage of $(U - V\cos\omega t)$ and $-(U - V\cos\omega t)$ are applied to opposing rods, respectively [80, 81]. The pairs of rods are held at the same potential, generating an electrical field where ions of a specific m/z value have a stable trajectory through. The remaining ions will strike the rods, get neutralized, and are pumped away. Changing the ratio of U and V , will change the m/z value of the ions allowed through the quadrupole [81].

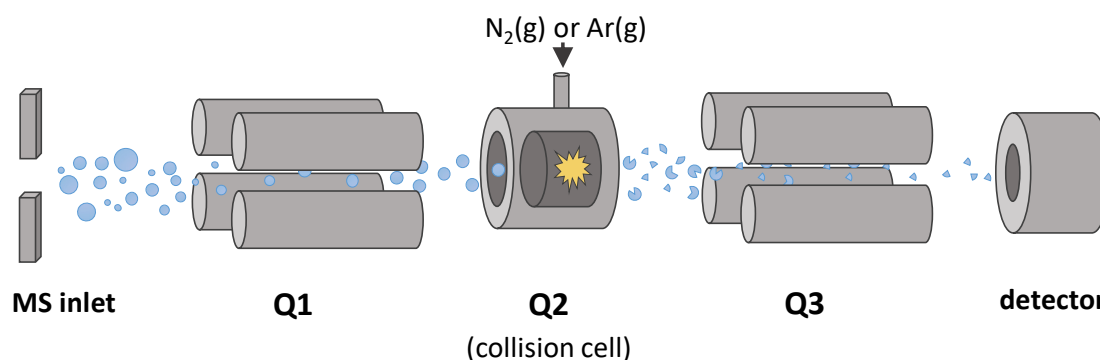


Figure 22: Schematic illustration of a triple quadrupole mass spectrometer. In multiple reaction monitoring ions of different m/z value are accelerated towards Q1 where the filtering of these ions enables ions of one specific m/z value to enter the collision cell (Q2). Upon collision in the Q2, fragment ions of different m/z value are accelerated towards Q3, where the filtering of these fragments enables the detection of fragments of specific m/z values. *The figure was created by the author of this document and was adapted from [82].*

The Q1 and Q3 filter ions by an adjustment of U and V , while the Q2 operates as a transmission device in a broad m/z range. The Q2 is placed inside a chamber pressurized with either nitrogen or argon gas, which assembly is often referred to as the collision cell of the TQ-MS. Molecular ions that enter the collision cell collide with the gas in the chamber and induce fragmentation of the molecular ion through the lowest energy dissociation pathways. This is accomplished when some of the kinetic energy from the gas molecules is converted to internal energy, causing bond breakage and dissociation of the molecular ion [83].

Multiple reaction monitoring

The TQ-MS can run in different modes, depending on the degree of ion filtering that is desired. Selected reaction monitoring (SRM) offers the highest degree of filtering (**Figure 22**). Here, ions of different m/z value are accelerated towards Q1 where the filtering of these ions enables ions of one specific m/z value to enter the collision cell (Q2). Upon collision in the Q2, fragment ions of different m/z value are accelerated towards Q3, where the filtering of these fragments

enables the detection of fragments of a specific m/z value [50, 84]. If several product ions are monitored simultaneously, multiple reaction monitoring (MRM) is the preferred term.

In peptide fragmentation, the lowest energy dissociation is characteristically observed along the peptide backbone, as depicted in **Figure 23**. The rich fragmentation pattern produced by collision-induced dissociation (CID) is commonly designated according to the Roepstorff–Fohlmann–Biemann nomenclature, where ions including the original N-terminal are referred to as a-, b- and c-ions and ions including the original C-terminal are referred to as x-,y- and z-ions [53].

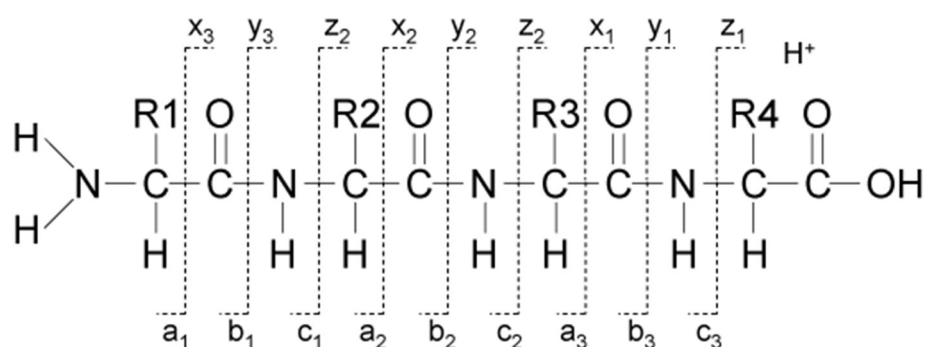


Figure 23: The characteristic dissociation of the peptide backbone during CID. The resulting ions are named according to the Roepstorff-Fohlmann-Biemann nomenclature [53].

The utilization of MRM is pivotal for the reliable detection of peptides. This can be illustrated by the following example: Without fragmentation, an average tryptic peptide constructed from 9 amino acid residues can give rise to 38 2880 different sequence combinations detected by the same m/z value. By introducing the monitorization of a single fragment, the uncertainty of detection can be reduced by up to 99 %².

2.9.2 Electrospray ionization and nanoelectrospray

ESI is an excellent technique to afford the ion transfer of ions in solution to the isolated gaseous state at atmospheric pressure. Employing an ESI interface when coupling LC and MS allows for a ‘soft ionization’, which primarily produces molecular mass information [85]. Soft ionization is accomplished by a gradual desolvation, with an energy transfer that, in principle, does not exceed the dissociation energy of the analyte [86]. ESI serves well for a variety of

² Calculations are provided in **Appendix, Figure 54**.

analytes but has been especially useful in the bioanalysis of large, polar, and non-volatile analytes [87].

Figure 24 shows a schematic illustration of the ESI in positive ion-mode. The ESI interface can be viewed as an electrolytic flow cell, wherein positive mode, the ESI needle is the positive electrode and the MS inlet acts as the negative counter electrode. A high electric potential of 3-5 kV is typically applied; thus, caution is advised during handling. Under the influence of increasing field strength, ions that enter the needle immediately initiate a charge separation: Positive ions are drawn towards open-end of the needle, closer to the negative electrode, while the negative ions are withheld in the needle. At one point, the mutual repulsion of the positive ions at the meniscus overcomes the surface tension of the liquid and the liquid starts to expand. The liquid expansion evolves into the formation of the so-called Taylor cone when a critical field strength is reached. This was theoretically described by Geoffrey Taylor in 1964, hence the name, Taylor cone [88].

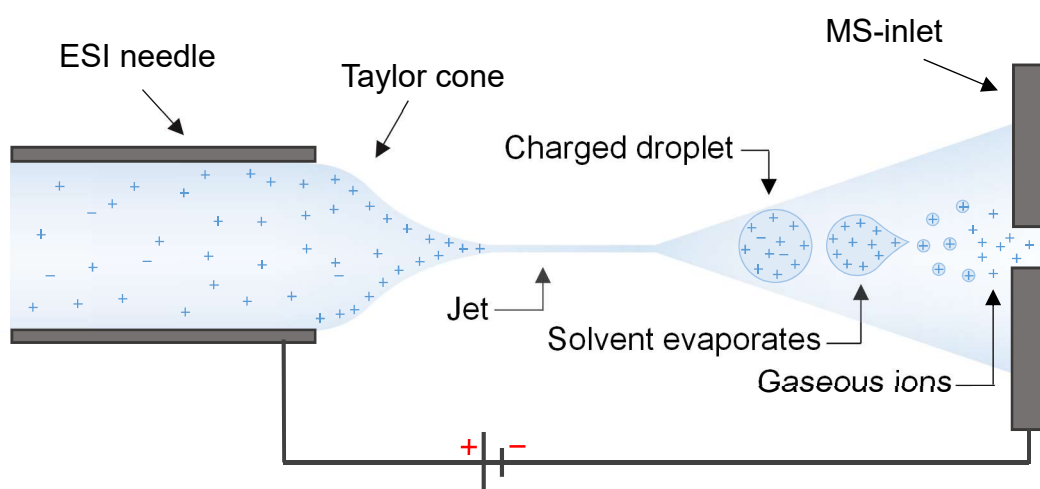


Figure 24: The mechanism of ion transfer in electrospray ionization. The ESI needle acts as the positive electrode and the MS inlet as the negative electrode. Upon the application of an electric field, the positive ions move towards the MS inlet, causing the formation of a fine plume, from where droplet desolvation causes the isolation of gaseous ions. *The figure has been created by the author of this document and was adapted from [89].*

From the apex of the cone, a fine jet with high charge density emerges. The high charge density destabilizes the jet and causes a rapid expansion into a plume of charged microdroplets. As the solvent evaporates from the droplets, the charge remains, and charge density increases. At the Rayleigh instability limit, the electrostatic forces overcome the surface tension causing the

droplets to disintegrate into smaller units. A repeating cascade of disintegration eventually leaves the ions in an isolated gaseous state [90]. It was originally believed that the process of Coulomb fission leads to the disintegration of droplets into equally, smaller-sized droplets. Later, however, this theory was displaced by empirical evidence showing that the larger droplets eject a series of smaller droplets that carry 1-2% of the mass of the parent droplet and 10-18% of the charge; it is from these smaller droplets that gaseous ions are formed [90]. Two theories have been proposed for the formation of gaseous ions; (i) the charged residue model, which assumes that complete successive desolvation of solvent molecules leaves only the gaseous ions behind and (ii) the ion evaporation model, which describes the formation of gaseous ions as direct evaporation from the highly charge microdroplets [86]. Although neither of the theories can fully account for all aspects of the process, the ion evaporation model seems to gain more support in the scientific community.

Nanoelectrospray

Conventional ESI runs at flow rates from 1 $\mu\text{L}/\text{min}$ up to 1 mL/min . The high volume passing through the needle often requires the help of drying gas or the addition of heat to aid desolvation. With nanoESI, lower flow rates, in the range from 10 nL/min to 1000 nL/min facilitates the formation of smaller droplets. NanoESI operates at flowrates that are compatible with nanoLC. This facilitates the formation of droplets that are 100 – 1000 times smaller in volume than droplets formed with conventional ESI. This, in turn, eases solvent evaporation and analyte desolvation. NanoESI also tolerates a wider range of mobile phase composition, even allowing aerosol formation with pure water. This is a very helpful feature for hydrophilic peptide analysis [91, 92]. The nanoESI needle/capillary is better at concentrating the analyte at the emitter tip, which has shown to produce a significant increase in sensitivity [92].

2.10 MRM assay development for absolute quantitation

Quickly recapitulating, the quantification of the protein biomarker ALT1 with MRM targeted proteomics in liver organoid medium can aid in the early identification of DILI (e.g APAP-ILI) potential. To implement this theory in practice, a strategic plan to assure quality of the results is necessary. Kuzyk et. al have presented a strategical approach for MRM-based protein quantification which also aligns with guidelines from other renowned authors [93-95]. **Figure 25** describes the key elements of MRM-based targeted proteomics.

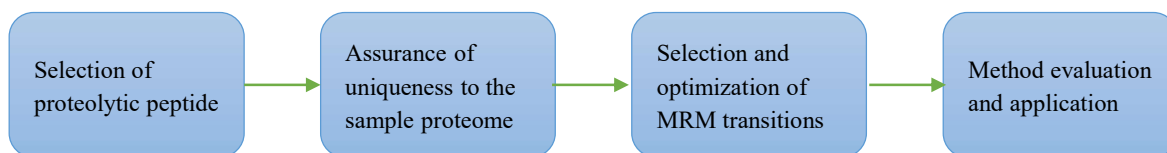


Figure 25: The key elements of MRM-based protein quantification, based on [93].

For MRM based protein quantification, the concentration of a single peptide is used to infer the absolute concentration of the target protein. This peptide is referred to as the signature peptide. The selection process must ensure that the signature peptide is representative of the target protein. This includes that the peptide should be unmodifiable post protein translation and should remain stable during the entirety of the workflow. The signature peptide should be unique, in other words, only trace back to the target protein and the uniqueness can be limited to the sample proteome or can be extended as appropriate. Once the signature peptide is selected, MRM transitions must be carefully selected and optimized for low detection limits. Lastly, a suitable method of quantification must be decided upon and the final method must be evaluated and tested.

2.11 Aim of study

DILI has been a major concern in drug development and has been the number one cause for drug withdrawals in the last 50 years. Current practices in preclinical safety assessment cannot detect all potential DILI drug candidates and hence impede the early termination of these drug candidates. Recent advances in liver-emulating models with the development of hepatic organoids combined with well-studied DILI biomarkers might offer an opportunity to improve the current practices for preclinical safety assessment.

The aim of this study was to develop a nanoLC-MS MRM assay for the absolute quantitation of the DILI biomarker ALT1. The optimized method was to be applied for the investigation of APAP- and NAPQI-induced ALT1 release in hepatic organoids.

3 Experimental

3.1 Software, online tools and databases

Skyline 20.1 has been used as the primal tool to generate unique MRM transitions, store proteome databases and spectral libraries, and process spectra from qualitative and quantitative peptide data. *Uniprot* has been used to retrieve protein isomer information, subcellular locations, and accession numbers. The *BLAST sequence analysis tool* has been used to verify the uniqueness of peptides that were generated in *Skyline*. *PeptideAtlas* has been used to retrieve peptide observability scores based on compiled scientific literature. Protein sequences were retrieved from the *Swissprot human proteome* database. The spectral libraries NIST Iontrap and NIST Orbitrap-HCD were retrieved from the *National Institute of Standards and Technology (NIST)*.

QR codes to the websites or spectral libraries are found in **Appendix**.

3.2 Chemicals, materials, and equipment

Chemicals

Sequencing Grade Modified Trypsin (V5111) was purchased from Promega Corporations (Fitchburg, WI, US). Formic acid (FA, LiChropur, $\geq 98\%$), acetone, trifluoroacetic acid (TFA), ammonium bicarbonate (ABC), IAM, DTT, urea, Protease Inhibitor Cocktail tablets (Roche), acetaminophen (APAP, N-(4-hydroxyphenyl)acetamide, analytical grade) and N-acetylbenzoquinoneimine (NAPQI) was purchased from Sigma Aldrich (St. Louis, MO, US). NuPAGE™ LDS sample buffer (4x, Invitrogen™), Bolt™ MOPS SDS Running Buffer (20x, Invitrogen™), Imperial™ protein stain, Pierce® RIPA Lysis, and Extraction Buffer, Novex® Sharp Pre-Stained Protein Standard and the Pierce® BCA Protein Assay Kit were purchased from Thermo Fisher Scientific (Waltham, MA, US). Acetonitrile (HiPerSolv CHROMANORM®, $\geq 99.9\%$) and water (HiPerSolv CHROMANORM® for LC-MS) were purchased from VWR (Radnor, PA, US). FBS (fetal bovine serum) free cell medium was kindly provided by PhD candidate Frøydis Sved Skottvoll. Type 1 water was obtained from a Milli-Q® Integral water purification system from Merck Millipore (Billerica, MA, US).

Protein and peptide standards

Human serum albumin (recombinant source, lyophilized powder, $\geq 99\%$) was purchased from Sigma Aldrich and stored at $-20\text{ }^{\circ}\text{C}$. Alanine aminotransferase isoform 1 (recombinant source, lyophilized powder, $99\%^3$) was purchased via Sigma Aldrich from the European Commission Joint Research Centre (EC JRC, Geel, Belgium). The starting material was produced and processed by Asahi Kasei Pharma Corporation (Tokyo, Japan) and enzyme activity was validated by EC JRC. The protein standard was stored at $-80\text{ }^{\circ}\text{C}$. The peptides LLVAGEGHTR and LLVA* $(^{13}\text{C}_3\ ^{15}\text{N})$ GEGHTR (lyophilized powder, 95%) were purchased from Biomatik (Wilmington, DE, US). Hepatic organoids cultured from pluripotent stem cells were kindly provided by Postdoctoral Fellow Sean Harrison (Suvillian Group, University of Oslo).

Consumables

Microcentrifuge tubes (1.5 mL) and Protein Lobind microcentrifuge tubes (1.5 mL) were purchased from Eppendorf (Hauppauge, NY, US). Sterile pipette tips with extended length and ultrafine point and 96-micro well plates were purchased from VWR. Bolt™ 4-12% Bis-Tris Plus gels (Invitrogen™), Finntip pipette tips in various volumes and solid-phase micro extraction tips (ZipTip, C18) were purchased from Sigma Aldrich. Insoluble SPE columns (100 mg C18 3 mL) were purchased from Biotage (Uppsala, Sweden).

Lab equipment

The analytical balance used was an AT200 DeltaRange from Mettler-Toledo (Columbus, OH, US), the vortex mixer used was a MS” Mini shaker from KIA (Wilmington, NC, US), the ultrasonic cleaner used was a Branson 200 from ORCA (Albertville, AL, US), the incubator used was a PHMT Series Thermoshaker For Microtubes and Microplates from Grant Instruments (Shepreth Cambridgeshire, UK). The oven used was a GC-17A from SHIMADZU (Kyoto, Japan). The evaporator used was a Vacufuge plus basic device from Eppendorf. A mini Gel Tank from Thermo Fisher Scientific was used during gel-electrophoresis. The autopipettes used were FinnpiPETTE™ F2 Variable Volume Single-Channel Pipettes from Thermo Scientific. The benchtop microcentrifuge used was a Mini Star Silverline purchased from VWR.

³ The purity was guaranteed by the provider as containing no other enzyme with a relative catalytic activity concentration of more than 1.0 % of the total catalytic activity concentration.

3.3 Spectrophotometric determination of total protein

Total protein determination was performed with the Pierce BCA Protein Assay Kit. Sample preparation was based on the Pierce BCA Protein Assay Kit (Reducing agent compatible) – User Guide [73] and modified for compatibility with subsequent analysis employing the NanoDrop 2000 spectrophotometer from Thermo Fisher Scientific. The kit contains 5 reagents: BCA reagent A, BCA reagent B, Albumin standard, Compatibility reagent, and Reconstitution buffer. The compositions of these reagents, as stated by the manufacturer, are as follows: The BCA reagent A contains sodium carbonate, sodium bicarbonate, BCA, and sodium tartrate in 0.1 M sodium hydroxide. BCA reagent B contains 4 % cupric sulfate. The albumin standard contains bovine serum albumin at 2mg/mL in 0.9 % saline and 0.05% sodium azide. The composition for the Compatibility reagent and Reconstitution Buffer was not stated.

Preparation of BCA assay reagents

The Working Reconstitution Buffer was prepared by adding 600 μ L Reconstitution Buffer to 600 μ L HPLC grade water. The Compatibility Reagent Stock Solution was prepared by adding 1 mL Working Reconstitution Buffer to one tube of Compatibility Reagent and vortex for 30s at high speed. The solution was stored at 4 °C until use. The BCA Working Reagent was prepared by mixing 9412 μ L BCA Reagent A with 188 μ L BCA Reagent B and vortexed vigorously before use. All reagents were freshly prepared for that day.

Preparation of BSA standard solutions

The external calibration curve was established using standard solutions of BSA stock solution diluted with ABC buffer and prepared in microcentrifuge tubes or in a well plate. BSA standard solutions were prepared in the concentration range from 125 – 2000 μ g/mL and diluted accordingly, see **Appendix, Table 15**. Two replicates for each concentration were prepared. The calibration curve was established for each measurement session.

Preparation of samples

A 100 μ L sample aliquot of reduced and alkylated protein sample or untreated protein sample was thawed on ice and dilutions were performed as appropriate, see **Appendix, Table 16**. Two replicates of each sample were prepared in 0.5 mL microcentrifuge tubes. Untreated protein samples were not treated with compatibility reagent.

Protein quantification

10 μL of standard solution and samples were transferred to clean 1.5 mL microcentrifuge tubes. 10 μL of Compatibility Reagent Stock Solution was added to each tube and vortex at low speed for 20 s. The samples were incubated with closed lids in a GC-oven at 37 °C for 15 min. This step was skipped for untreated protein samples. 100 μL of BCA working reagent was added to each tube and incubated with closed lids in a GC oven at 37 °C for 30 min followed by 5 min of cooling at room temperature. The absorbance of the Cu-BCA chelate was measured at its maximum at 562 nm within 10 min after cooling. The analysis was performed by pipetting 3 μL of blank/standard/sample/ onto the pedestal of the instrument. Standards and samples were analyzed by increasing order of concentration. The pedestal was wiped with a dry tissue in-between application.

For smaller sample sizes down to 5 μL the sample preparation was prepared in 96-well plates and BCA reagent was added in a sample-reagent ratio of 1/8 (vol/vol). Sample preparation in well-plates was only performed for samples not treated with DTT and IAM.

3.4 Sample preparation for protein samples

3.4.1 Protein precipitation

The protein precipitation procedure was kindly provided by PhD candidate Frøydis Sved Skottvoll and was based on a protocol from Promega [96]. Protein precipitation was performed for organoid samples.

Neat acetone (-20 °C) was added to the protein solution at a ratio of 4/1 (vol/vol) in LoBind microcentrifuge tubes. The sample was mixed with a vortex mixer and kept at -80 °C for 20 min. The sample was subsequently centrifuged at 14 000 g for 10 min at 4 °C. If the pellet formation was unsuccessful, centrifugation was repeated. The supernatant was discarded, and the pellet was dried in a fume hood and stored at -80 °C until used.

3.4.2 In-solution digestion

The following procedure was adapted from a previously developed method kindly provided by Tore Vehus and edited by Henriette Engen Berg. In-solution digestion was performed for HSA standard, ALT standard, cell medium, and organoid samples.

Solutions

50 mM ABC was prepared by dissolving 0.20 g in 50 mL and stored at room temperature (rt.) 8 M urea in 50 mM ABC was prepared by dissolving 2.40 g of urea in 5 mL 50 mM ABC and stored at rt. 1 M DTT, 10 mg/mL trypsin and 1 M IAM were prepared by PhD candidates Henriette Engen Berg and Frøydis Sved Skotvoll and stored at - 80 °C. 10 % TFA was prepared by diluting 1 mL TFA in 9 mL HPLC grade water and was stored at rt.

Reduction and alkylation

The protein source was solubilized in 1 mL 8 M urea/50 mM NH_4HCO_3 to a final concentration of 1 mg/mL and divided into two aliquots of 0.5 mL. One aliquot was stored at - 80 °C until use. 2.5 μL 1 M DTT was added to a final concentration of 5 mM, mixed with a vortex mixer for approx. 20 s and incubated in a Thermoshaker at 37 °C for 30 min. 7.5 μL 1 M IAM was added to a final concentration of 15 mM, mixed and incubated in the dark at room temperature for 30 min. The mixture was divided into 100 μL aliquots and stored at -80 °C if not used immediately.

Protein digestion

700 μL of 50 mM NH_4HCO_3 was added to one aliquot of reduced and alkylated sample until the urea concentration was reduced to less than 1M. 10 mg/mL sequence grade trypsin was added to a final protease/protein ratio of 1/20 (w/w) and incubated in a Thermoshaker at 37 °C for at least 18 h. The protease activity was terminated by the addition of 7 μL 10% TFA in HPLC water to a final concentration of 0.1 % TFA.

3.4.3 Gel electrophoresis

Gel electrophoresis was performed per Mini Gel Tank – User Guide [97]. Staining and detaining were performed per Imperial Protein Stain – User Guide [98].

Solutions

1x LDS Sample buffer (4x) was prepared by dilution with HPLC grade water. 1x MES SDS Running buffer (20x) was prepared by dilution with HPLC grade water.

The protein sample was redissolved in 1x Sample buffer and cooked at 92 °C for 2 min in a GC-oven. Precasted gels were placed into the gel tank and 1x Running buffer was added to the

fill line. 60 μL of the sample was added with sterilized pipette tips into the wells and gel electrophoresis was performed at 200 V for 24 min. The finished gel was removed from the frame and the foot and wells of the gel were excised and discarded.

Staining and destaining

The gel was placed into a plastic container and type I water was filled into the container to cover the gel piece and the container was placed onto a Thermoshaker at around 300 rpm for 5 min. The liquid was poured off and replaced by fresh type I water. This step was repeated five times. Staining was performed by pouring the stain into the container until the entire gel was covered before placing in onto a shaker for approximately 20 min or until the protein lanes were clearly visible. The gel was washed with Type I water, the liquid was poured off and replaced by fresh water three times. If not used immediately, the gel was placed covered in the fridge overnight.

Excising of protein bands

The gel was placed onto Parafilm and wetted with type I water to prevent the gel from drying. The excised areas from a lane were cut into 1x1 mm squares and transferred to microcentrifuge tubes and spun down on a benchtop microcentrifuge. For the excision of bands for ALT1 for hepatic organoids, two lanes were pooled into one microcentrifuge tube.

3.4.4 In-gel digestion

In-gel digestion was based on an in-gel digestion protocol developed by Shevchenko et al. [99].

Solutions

100 mM ABC was prepared by dissolving 158 mg ABC in 20 mL HPLC grade water. 13 ng/ μL trypsin in 10 mM ABC with 10 % (vol/vol) ACN was prepared by diluting 13 μL of 1 $\mu\text{g}/\text{mL}$ trypsin in 100 μL 100 mM ABC, 100 μL ACN and 787 μL HPLC grade water to a total volume of 1000 μL . 10 mM DTT in 100 mM ABC was prepared by diluting 10 μL 1 M DTT in 990 μL 100 mM ABC. 55 mM IAM in 100 mM ABC was prepared by diluting 55 μL 1 M IAM in 945 μL 100 mM ABC.

Reduction and alkylation

500 μL of neat ACN was added to the tubes which were subsequently incubated at room temperature for 10 min. The gel pieces were spun down for approximately 20 s and all liquid was removed with a pipette (Step 0). 100 μL of DTT was added (or enough to cover the gel pieces completely) and the tubes were incubated for 30 min at 56 °C. The tubes were covered with foil during incubation to avoid gradient heating within the tubes. Step 0 was repeated. 100 μL IAM was added and the tubes were incubated at rt. for 20 min in the dark. Step 0 was repeated.

Destaining

100 μL (or enough to cover the pieces) of 100 mM ABC/ACN (v/v,1/1) was added and the tubes were incubated for 30 min with occasional vortexing. The step was repeated if staining was not removed sufficiently.

Trypsinization

Trypsinization was performed by adding 200 μL (or enough to cover the pieces) of trypsin solution to the tubes and placing them on ice for 30 min. More trypsin was added to saturate the pieces. The tubes were placed back on ice for 90 min and 20-50 μL of 100 mM ABC buffer was added to cover the pieces. The tubes were incubated overnight at 37 °C with 500 rpm.

Extraction of digested peptides

Extraction buffer was added to the tryptic digest followed by incubation for 15 min at 37 °C. The gel pieces were spun down, and the supernatant was collected. An additional 100 μL of extraction buffer was added followed by 15 min incubation at 37 °C. The extract was dried in a vacuum centrifuge and stored at -20 °C until used. The sample was reconstituted in 0.1 % FA in H_2O .

3.4.5 Peptide desalting

The solid-phase extraction procedure was performed for desalting of HSA- and ALT standards. The solid-phase microextraction was performed for organoid samples and cell medium.

Solutions

0.1% TFA in ACN was prepared by diluting 20 μL in ACN to a final volume of 20 mL. 2% ACN and 0.1% TFA in water was prepared by diluting 400 μL ACN and 20 μL TFA in water to a final volume of 20 mL. 0.1 % TFA in water was prepared by diluting 20 μL in HPLC grade water to a final volume of 20 mL.

Solid-phase extraction procedure

The SPE-column was activated with 1 mL 0.1% TFA in ACN followed by 3 x 1 mL 2% ACN and 0.1% TFA in water. The sample was added to the SPE-column – flow-through was collected and passed through the column one more time. The column was washed with 1 mL 0.1% TFA in HPLC grade water. The analytes were eluted with 1 mL 0.1% TFA in ACN and dried in a SpeedVac at 30 °C. The samples were reconstituted in the desired volume of 0.1% FA in HPLC grade water.

Solid-phase microextraction procedure

Aspiration of solutions was performed by first pressing firmly down on the pipette plunger to create negative pressure and thereafter slowly aspirating the solutions without introducing air into the pipette tip. The solutions were pipetted by pressing down on the plunger and the plunger was held fixed in that position for the next aspiration. The ZipTips were activated with neat ACN (2x) followed by 0.1 % TFA in water. The sample was applied by repeatedly (10x) drawing the sample solution through the ZipTip. The ZipTip was washed with 0.1 % TFA in water (2x) and eluted into 400 μL 60 % ACN and 0.1 % TFA in water by drawing the elution solution through the ZipTip 3-4 times. The samples were dried in a SpeedVac at 30 °C and reconstituted in the desired volume of 0.1 % FA in HPLC grade water.

3.5 Preparation of peptide standard solutions

A stock solution of 950 μM LLVAGEGHTR was prepared by dissolving 1.0 mg, aliquoted by the manufacturer, in 1000 μL of HPLC grade water. Further dilutions were performed as appropriate, see **Appendix, Table 17**.

946 μM LLVA*GEGHTR was prepared by dissolving 1.0 mg, aliquoted by the manufacturer, in 1000 μL of HPLC grade water. Further dilutions were performed as appropriate, see **Appendix, Table 18**.

Standard solutions for establishing the calibration curve in the concentration range from 0.1 – 10 fmol/ μL with and without cell medium (matrix) were prepared as appropriate, see **Appendix, Table 19**. 1.25 $\mu\text{g}/\mu\text{L}$ cell medium was prepared by dissolving 1 mg of digested cell medium in 800 μL 0.1 % FA in water.

3.6 Liquid chromatography-mass spectrometry platform

Figure 26 depicts the analytical platform on which samples were analyzed.

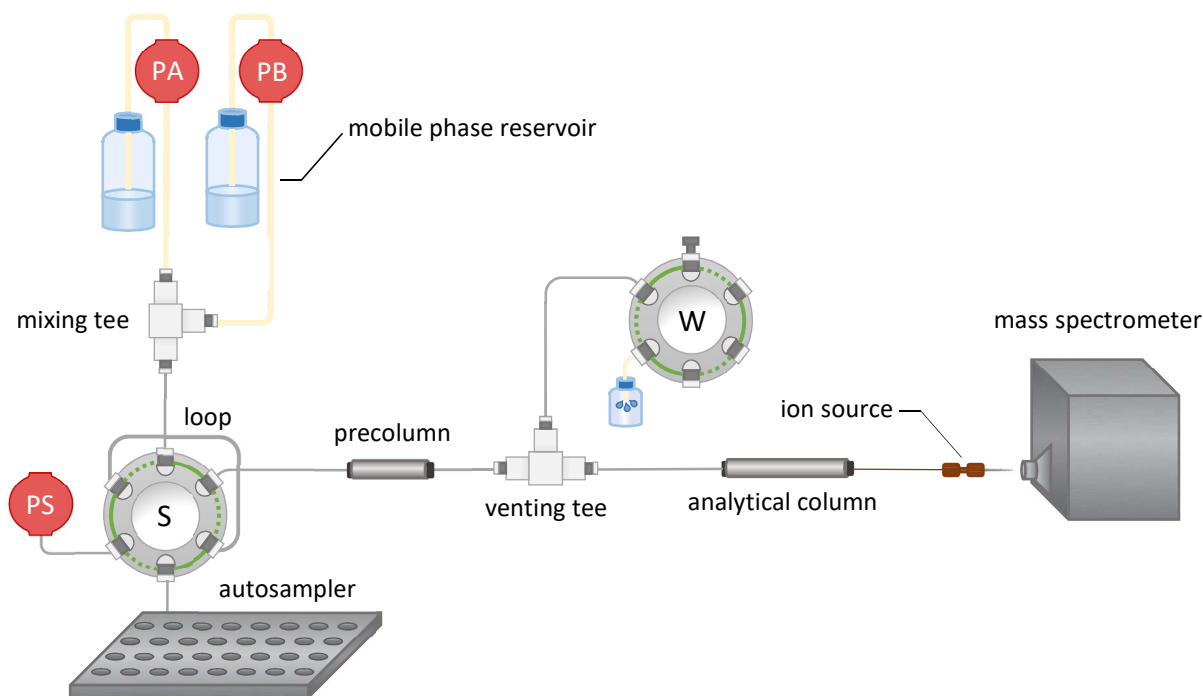


Figure 26: Illustrative figure of the nanoLC-MS platform for targeted protein analysis. A run is a three-step process: 1) a precolumn equilibration (dotted alignment in both valves), 2) an analytical column equilibration (solid alignment) and 3) the sample application (dotted alignment in both valves). The components of the platform are not in proportion. Mobile phase valves are not shown.

Table 2 lists the hardware components of the nanoLC-ESI-MS analytical platform and the analytical columns with dimensions sorted by manufacturer.

Table 2: Hardware specification of nanoLC-ESI-MS analytical platform and analytical columns sorted by manufacturer.

Generic name	product
Thermo Fisher Scientific (Waltham, MA, US)	
Liquid chromatograph	Easy-nLC 1000 liquid chromatograph w/ 96-well autosampler
Ion source	Nanospray Flex ion source
Mass spectrometer	TSQ Triple-stage quadrupole mass spectrometer
Analytical column	Acclaim PepMap™ 100, 75 µm x 5 cm, nanoViper, C18, 3 µm, 100Å
Precolumn	Acclaim PepMap™ 100, 75 µm ID x 5 cm L, nanoViper, C18, 3 µm, 100Å
Tubing to precolumn	nanoViper (PEEK shielded fused silica) w/ fingertight fitting, 20µm ID x 550 mm L
Tubing to waste	nanoViper (PEEK shielded fused silica) w/ fingertight fitting, 75µm ID x 550 mm L
IDEX Health & Science (Oak Harbor, WA, US)	
Fitting to spray emitter	Microtight PEEK fitting
Union to spray emitter	Microtight PEEK ZDV union
Valco Instruments (Huston, TX, US)	
Union to precolumn	Stainless steel union
Venting tee	Stainless steel Tee
In-house	
Analytical column	Accucore, 75 µm ID x 5 cm L, C18, 2.6 µm, 150 Å. Column was kindly provided and packed by Ph.D candidate Henriette Engen Berg [100]
Analytical column	Accucore, 50 µm ID x 5 cm L, C18, 2.6 µm, 150 Å. Column was kindly provided and packed by Ph.D candidate Henriette Engen Berg [100]

3.6.1 Sample run conditions

The mobile phase consisted of solvent A (water/FA, 99.9/0.1 %, v/v) and solvent B (ACN/water/FA, 89.9/10/0.1 %, v/v/v). Solvents were degassed with helium before use. The analyses were performed with different linear gradients and analytical columns; which combinations are summarized in **Table 3**. **Figure 27** visualizes the gradients that were used for the respective analytical columns. A 120 min linear gradients from 3-60% B was also employed to map retention times of HSA peptides (Acclaim 75 µm). A column-compatible flow rate of 400

nL/min and 250 nL/min was employed for the columns with ID 75 μm and ID 50 μm , respectively. The injection volume was 1 or 10 μL .

Table 3: Sample run conditions (SRC) including the analytical column and the linear gradient that was employed.

Running condition (#)	Analytical column	Linear gradient (%B, min)
1	Acclaim 75 μm	3-60, 120
2	Acclaim 75 μm	1-15, 40
3	Accucore 75 μm	3-25, 56
3	Accucore 75 μm	3-15, 40
4	Accucore 50 μm	13-23, 8

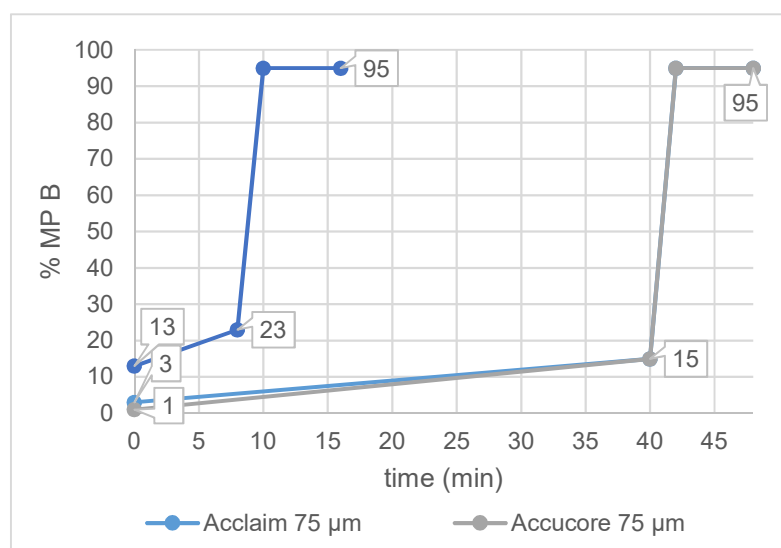


Figure 27: The linear gradients (including washing steps) that were applied during runs with different columns.

3.7 Software settings

3.7.1 Peptide and MRM selection criteria - Skyline settings

The selection criteria for the signature peptides of HSA and ALT were based on recommendation guidelines from Kuzyk et al. [93].

The protein was selected as a target in Skyline and the sequence was extracted from the Swissprot human proteome database previously uploaded to the software. Skyline Peptide Settings were adjusted to filter the peptide sequence following the recommended guidelines. Mentionable settings are listed in **Table 4**. MRM transitions were selected based on the criteria listed in **Table 5**. The top 5 spectral library matches from the filtered results were chosen to further limit the number of transitions.

Table 4: Peptide settings implemented for *in silico* peptide filtering in Skyline.

Feature	Setting
Enzyme	Trypsin [KR P]
Max missed cleavages	0
Background proteome	Human proteome
Min length	5
Max length	25
Structural modifications	Carbamidomethyl (C)
Peptides excluded containing	Cys, Asp-Pro, Met, N(Gly) ¹ and Trp

¹Was not a predefined option in Skyline and had to be added with the regular expression ^Q

Table 5: MRM transition settings implemented for *in silico* product ion filtering in Skyline.

Feature	Setting
Precursor charges (+)	2,3
Ion charges (+)	1,2
Product ion selection	From: ion 1, To: last ion
Ion types	y, b

3.7.2 MRM transitions

Table 6 and **Table 7** hold the MRM transitions recorded for HSA and ALT isoform 1, respectively, which were generated from the NIST Iontrap spectral library by Skyline based on peptide and MRM selection criteria.

Table 6: MRM transitions for human serum albumin retrieved from the NIST Iontrap spectral library.

#	Peptide including cleaved amino acid (a.a)	Precursor	Product ion (+)				
1	K.DLGEENFK.A	479.2(++)	229.1	415.2	537.3	666.3	723.3
2	K.LVNEVTEFAK.T	575.3(++)	213.2	555.3	595.3	694.4	937.5
3	K.SLHTLFGDK.L	509.3(++)	338.2	409.2	466.2	680.4	817.4
4	K.SLHTLFGDK.L	339.9(+++)	233.8	262.1	319.2	409.2	466.2
5	K.DDNPLNLPR.L	470.73(++)	272.2	345.1	355.7	596.4	669.3
6	K.DDNPLNLPR.L	314.2(+++)	272.2	278.6(++)	335.1(++)	385.3	556.2
7	K.YLYEIAR.R	464.3(++)	277.2	359.2	440.2	488.3	651.3
8	R.HPYFYAPELFFAK.R	470.7(++)	272.2	345.1	355.7	596.4	669.3
9	R.HPYFYAPELFFAK.R	314.2(+++)	272.2	278.6	335.1	385.3	556.2
10	K.AEFAEVSK.L	440.7(++)	201.1	348.2	462.3	533.3	680.4
11	K.LVTDLTK.V	395.2(++)	213.2	361.2	476.3	577.3	676.4
12	K.TYETLEK.C	494.4(++)	265.1	394.2	591.3	720.4	838.4
13	K.FQNALLVR.Y	480.8(++)	276.1	387.3	500.4	571.4	685.4
14	K.LVAASQAALGL.-	507.3(++)	189.1	570.3	712.4	825.5	882.5
15	R.HPDYSVVLRL.L	656.4(++)	235.1	587.8	962.6	1077.6	1174.7
16	R.HPDYSVVLRL.L	437.9(+++)	399.7	401.3	514.4	456.2	699.3
17	K.VFDEFKPLVEEPQNLK.Q	1023.1(++)	712.4	848.5	970.5	1279.7	1333.7
18	K.VFDEFKPLVEEPQNLK.Q	682.4(+++)	667.3	712.4	777.9	842.5	900.0
19	K.VPQVSTPTLVEVSR.N	756.4(++)	706.9	900.5	1001.6	1088.6	1187.7
20	K.VPQVSTPTLVEVSR.N	504.6(+++)	361.2	490.3	576.3	589.3	1187.7

Table 7: MRM transitions for ALT isoform 1 retrieved from the NIST Iontrap spectral library.

#	Peptide including cleaved a.a	Precursor	Product ion (+)				
1	R.ALELEQELR.Q	550.8(++)	288.2	674.3	787.4	916.5	926.5
2	K.LLVAGEGHTR.T	526.8(++)	413.2	470.2	656.3	727.3	826.4
3	R.FAFEER.L	399.7(+++)	219.1	366.2	433.2	580.3	651.3
4	R.LFLLADEVYQDNVYAAGSQFHSFK. K	921.5(+++)	931.4 (++)	1103.0 (++)	1138.5 (++)	1195.1 (++)	1251.6 (++)

Table 8 holds the MRM transitions recorded for ALT isoform 1, which were generated from the NIST Iontrap and Orbitrap spectral library by Skyline based on peptide and MRM selection criteria.

Table 8: MRM transitions for ALT isoform 1 retrieved from the combined NIST Iontrap and Orbitrap spectral library.

#	Peptide including cleaved a.a	Precursor	Product ion (+)				
1	R.ALELEQELR.Q	550.8(++)	157.6	185.1	674.3	787.4	916.5
2	K.LLVAGEGHTR.T	526.8(++)	199.1	227.2	656.3	727.3	826.4
3	R.FAFEER.L	399.7(+++)	219.1	366.2	433.2	580.3	651.3

3.8 Elution time prediction

Target peptide retention times were predicted based on the SSRCalc calculator integrated into Skyline. Empirical retention time data from HSA tryptic peptides were plotted against SSRCalc values (sequence-specific hydrophobicity index) and linear regression was applied to generate a retention-time expression specific to the analytical platform. This expression in combination with the SSRCalc values of target peptides was used to predict target peptides retention time, within a 2 min prediction window.

3.9 Collision energy optimization

Collision energies (CEs) for all peptides were simultaneously optimized through CE gradient steps with MRM scheduling generated in Skyline. The CE gradient had step size 1V and ranged from (-) 5 V to (+) 5 V from a default CE generated from a predefined CE regression equation for Thermo TSQ Vantage provided by Skyline. Product ion m/z values were respectively stepped by 0.01 m/z to associate each CE step. MRM scheduling was accomplished by utilizing retention times for each peptide (precursor) from a previously recorded chromatogram. The best peak from two replicates was selected. CE steps associated with one precursor were recorded in a time window of 2 min. The CE step resulting in the greatest peak intensity for each peptide was plotted against its respective m/z value. A linear regression analysis was performed to produce a linear regression equation that was entered into Skyline to generate new optimized CE energies for peptides based on their m/z value. The best peak from two replicate was used in the regression analysis.

3.10 APAP- and NAPQI induced DILI in hepatic organoids

This experiment was performed together with PhD candidate Frøydis Sved Skottvoll and PhD Sean Harrison at the lab of Rikshospitalet.

Stock solutions

6 M stock solution of APAP was prepared by dissolving 453.6 mg lyophilized powder in DMSO. 0.6 M NAPQI was prepared by dissolving 1 mg lyophilized powder, as received by the manufacturer, in 11.02 μ L DMSO. The APAP stock solution was prepared a day in advance and stored in the fridge until used. The NAPQI stock solution was prepared right before use. The stock solutions of 6 M APAP and 0.6 M NAPQI in DMSO were further diluted in cell medium (1:30) to 0.2 M and 20 mM, respectively. Further dilution was performed right before use. Stock solutions were prepared under sterilized conditions.

Sample preparation

APAP and NAQI were added to wells with cell medium or organoids in the concentration range of 50 – 20 nM and 5 – 2 nM, respectively, to a final volume of 100 μ L, see **Appendix, Table 20**. Three replicates were prepared. Sample preparation was performed under sterilized conditions. The samples were incubated for 24 h. The supernatant was carefully removed from the wells and transferred to Lobind microcentrifuge tubes. The finalized samples were stored at -80 °C until used. Protein precipitation was performed as per section 3.4.1. The total protein content was determined for R.1.1-3 as per section 3.3. Samples were prepared for LC-MS analysis as per section 3.4.2 and 3.4.5.

3.11 Statistics

Grubb's test

A Grubb's test (two-sided, $\alpha = 0.05$) was used to remove outlying datapoints, assuming a normal distribution. For supplementary theory see Appendix, section 7.1.3.

Single-factor ANOVA

A single-factor ANOVA test (two-sided, $\alpha = 0.05$) was used to test the following hypothesis:

H₀: The average of the peak area for fragment y₈₊, y₇₊, and y₇₊₊ are the same for all groups.

*H_a The average of the peak area for fragment y₈₊, y₇₊, and y₈₊₊ is **not** the same for all groups.*

The null hypothesis was rejected in favor of the alternative hypothesis if $P(t_{\text{calc}} \geq t_{\text{crit}}) < \alpha$.

T-test

A one-sample student-test (two-sided, $\alpha = 0.05$) was used to test the following hypothesis:

H₀: The intercept for the linear equation for the calibration curves for fragment x is equal to zero

*H_a The intercept for the linear equation for the calibration curves for fragment x is **not** equal to zero*

The null hypothesis was rejected in favor of the alternative hypothesis if $P(t_{\text{calc}} \geq t_{\text{crit}}) < \alpha$.

A two-sample Welch's t-test (two-sided, $\alpha = 0.05$) was used to test the following hypothesis:

H₀: The mean slope of the calibration for fragment y₈₊₊ is the same for standard solutions prepared with or without cell medium.

*H_a The mean slope of the calibration for fragment y₈₊₊ is **not** the same for standard solutions prepared with or without cell medium.*

The null hypothesis was rejected in favor of the alternative hypothesis if $P(t_{\text{calc}} \geq t_{\text{crit}}) < \alpha$.

Access normality and equal variance

The normality of the data was assessed by testing if the skewness of the sample data points significantly differed from zero at $\alpha = 0.05$ (two-sided). The skewness was assessed for the residuals of the linear regression for fragment y₈₊, y₈₊₊, and y₇₊ with or without cell medium and for the fragment peak area for LLVA*GEGHTR.

Equal variance was assumed if group variances differed by more than 2-fold.

4 Results and discussions

The primary objective of this study was to develop a nanoLC-MS/MS MRM assay for the absolute quantification of ALT1, with the final goal to highlight the causal relation between ALT1 and APAP toxicity in hepatic organoids. A targeted proteomics approach for the absolute quantification of ALT1 was developed through a thorough assessment of signature peptide candidates and corresponding multiple reaction monitoring (MRM) transitions. Human serum albumin (HSA) was used as a protein model in preliminary experiments. The planned workflow of experiments is presented in three parts, as illustrated in **Figure 28**. At the end of this section, the figure will be revisited for a summary of the obtained results.

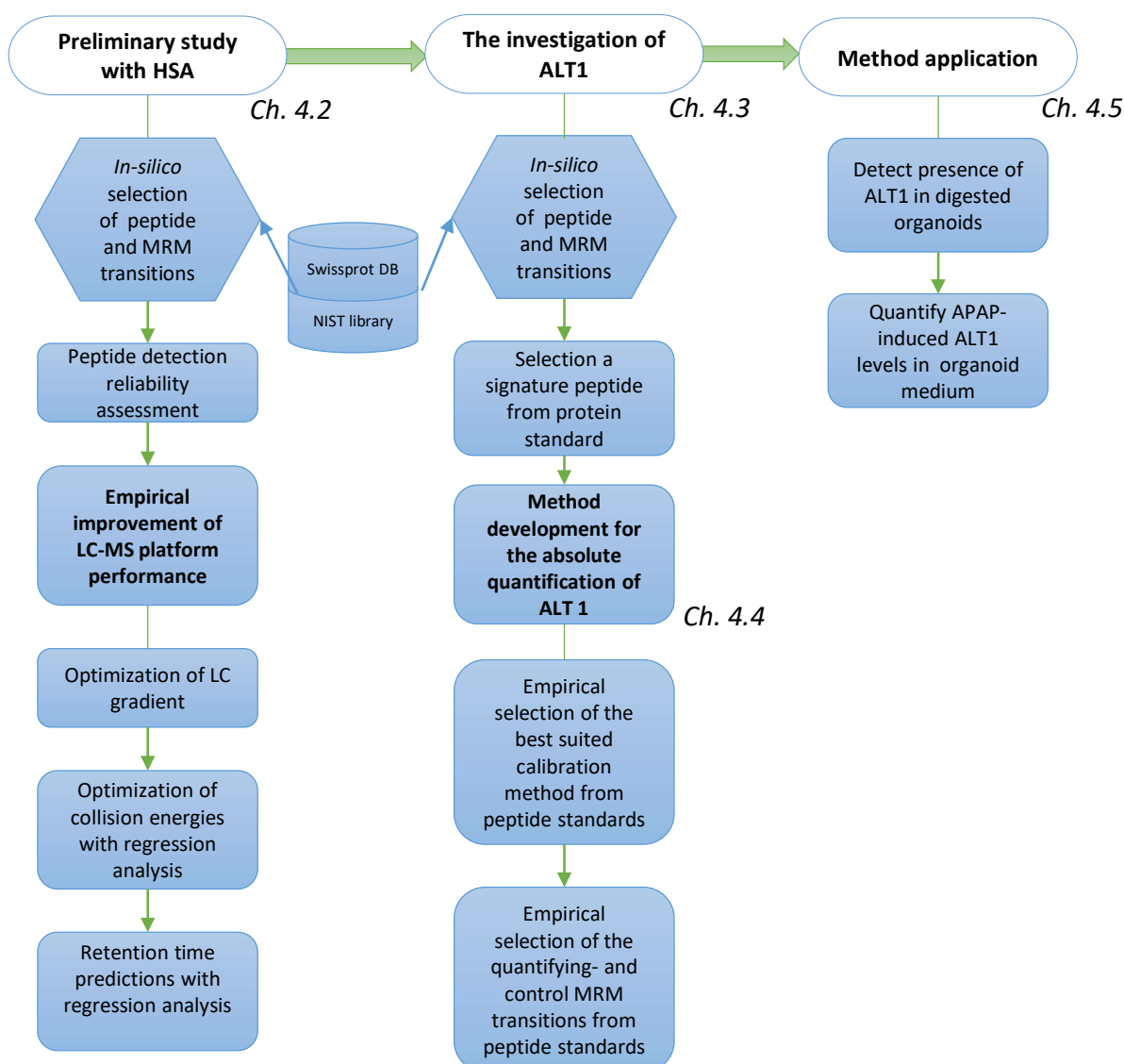


Figure 28: The planned workflow of experiments.

4.1 The selection of a suitable biomarker

The selection of a suitable biomarker for MRM assay development was made based on several considerations. It has been emphasized that the major trigger point for the withdrawal of marketing authorization of drugs has been attributed to idiosyncratic DILI – which is almost impossible to detect in clinical trials due to its low incident rates [11, 12]. The pathogenesis of idiosyncratic DILI is currently not completely uncovered, in turn, weakening the reliability of its associated biomarkers. It was therefore decided to develop an MRM assay for a biomarker associated with an intrinsic toxic response. Biomarkers from clinical DILI investigations are already successfully implemented when assessing the hepatic system in clinical phases of drug development and are strong candidates regarding their diagnostic potential [12]. It was therefore decided that a clinical biomarker should be targeted in the detection of DILI. This decision was also supported by the current uncertainties surrounding the liver-emulating features of hepatic organoids. These uncertainties are easier to assess or control when investigating fundamental toxic responses. Alanine aminotransferase isoform 1 meets the described requirements and was therefore chosen with approval from all supervisors.

4.2 Platform performance optimization with serum albumin

Before the investigation of a suitable signature peptide for ALT1, a pilot study with HSA was conducted. HSA was used for preliminary studies as it was readily available in pure form and saved unnecessary use of ALT1 standard. Gradient optimization, collision energy optimization, and elution time predictions were performed. How well the recommended MRM transitions from the NIST spectral library could detect HSA, was also investigated. The objective was not to select a signature peptide for HSA, but rather to perform software setting adjustments and platform optimization so that the ALT1 signature peptide could be selected on a proper platform foundation.

The uniqueness of HSA was defined at the protein level and was therefore not isoform-specific. This was done to increase the peptides meeting inclusion criteria, so that platform optimization could be performed on a bigger set of peptides. HSA is a post-translationally modified protein, where the 24 first amino acids (0,24), counting from the N-terminal, are not present in the mature form of the protein [48]. This section of the protein sequence was not included in the

peptide selection. Spectrophotometric determination of the total protein content (BCA Assay) of the HSA standard was omitted as the protein/trypsin ratio had already been established by PhD candidate Henriette Engen Berg. **Figure 29** shows the chromatogram of 10 HSA tryptic peptides.

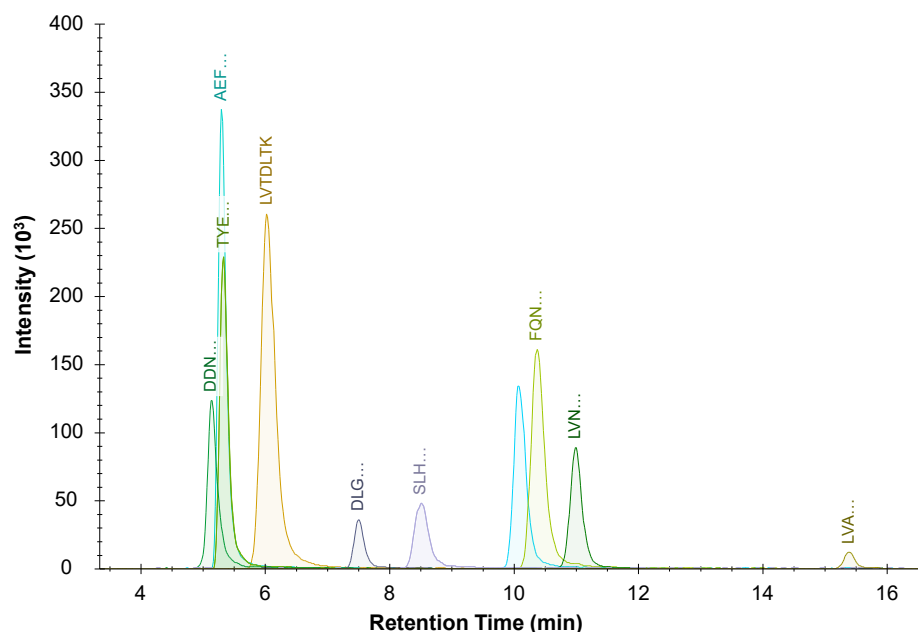


Figure 29: Total chromatogram of 10 HSA tryptic peptides from 100 pg HSA standard on-column (n=1). The chromatogram was acquired with SRC#1 (see section 3.6.1) and raw data is found in Appendix, Table 27.

The peak shapes were relatively symmetrical, indicating that the sample load of 100 pg on-column was within the loading capacity of the column. The peptides HPDYSVLLLR, VFDEFKPLVEEPQNLIK, HPYFYAPPELLFFAK, and VPQVSTPTLVEVSR could not be detected (see **Table 6** for all recorded peptides). It was suspected that the hydrophobic properties of these peptides caused strong retention on the column, which prevented the elution within the applied gradient. This was a reasonable assumption given that the retention time is linearly proportional to the peptides hydrophobicity index [101]. The linear relation between retention times and the hydrophobicity of the peptides was also observable from empirical data for the detected HSA tryptic peptides, as depicted in the linear regression in **Figure 30**. If linearity was assumed across the entire gradient, the recorded but not detected peptides should hypothetically have had eluted within 22 min of the gradient, as the green dots in **Figure 30** indicate. This demonstrated a contradiction with the leading hypothesis. Another hypothesis was that the hydrophobic peptides were insoluble or only partly soluble in the final

reconstitution solution before instrument injection. This could be combatted by adding an organic solvent to the reconstitution solution, but possibly at the expense of the chromatographic systems separation power. If the percentage of organic solvent of the reconstitution solution exceeds the starting concentration of organic modifier in the linear gradient, the peptides could be susceptible to plug elution where a loss of retention on the precolumn causes all separation to be lost. No action was taken to further investigate the cause of the recorded, but not detected peptides.

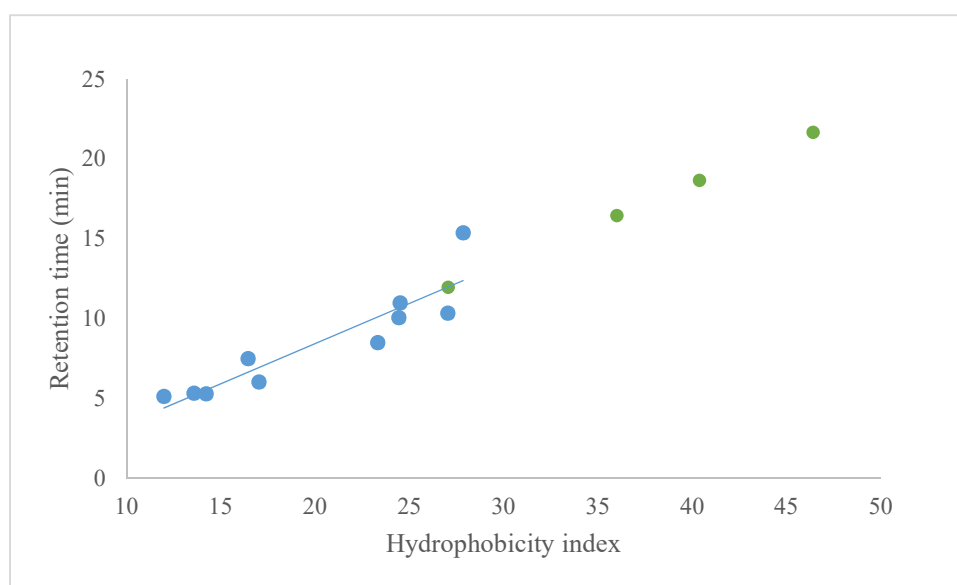


Figure 30: The linear relationship between measured retention times of the 10 detected HSA peptides (blue dots) acquired with SRC#1 vs their respective hydrophobicity index. The green dots indicate where the recorded, but not detected peptides HPDYSVLLLLR, VFDEFKPLVEEPQNLIK, HPYFYAPELLFFAK, and VPQVSTPTLVEVSR should have had eluted according to their hydrophobicity index.

Peptide identity indication

The rich peptide fragment pattern obtained by CID can be utilized to indicate peptide identity. Since CID is downstream of chromatographic separation, having several product ions (fragments) aligning in the chromatogram is a good indicator that the product ions originate from the same peptide, or phrased differently – is a good indicator that the targeted peptide is present in the sample. Simultaneously assessing the dotp-values⁴ for the individual peptides can help increase the confidence in true peptide picking.

⁴ The dotp-value ranges from 0 to 1 and numerically represents how well the product peak areas of an acquired peptide MS spectrum correspond to respective intensities in a library spectrum.

Peptide identity indication has been demonstrated with the HSA peptide LVTDLTK in **Figure 31**. Indicators that support true peptide assignment are a gaussian-like peak shape, good signal intensity, and aligning product ion retention times. A dotp value of 0.87 was also considered a good indicator that the peak has been assigned to its true peptide identity. Peptide identity assessment was performed for all HSA peptides. **Figure 32** shows the overall distribution of dotp values for all identified HSA peptides with a mean of 0.89. Retention time alignments across all identified HSA peptides were also considered satisfactory (not shown).

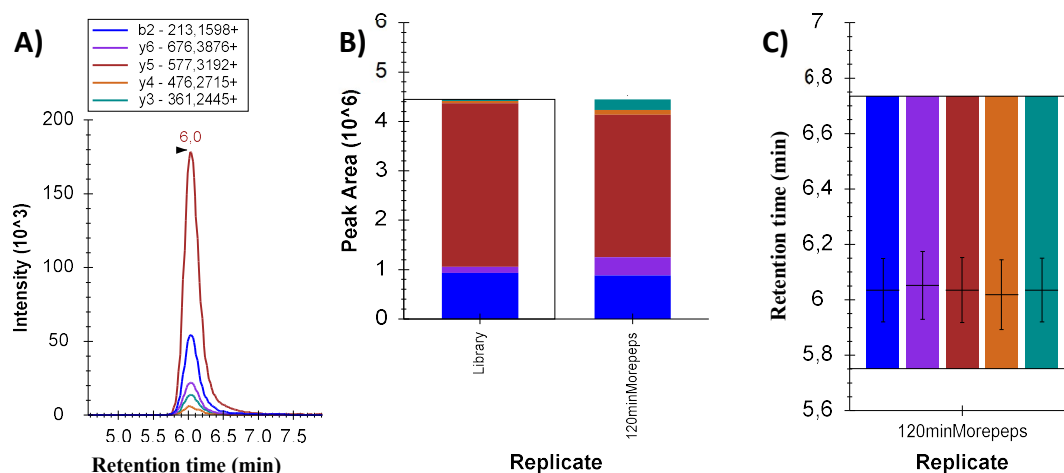


Figure 31: Peptide identity assessment demonstrated with peptide LVTDLTK. The colors represent each recorded MRM transition. A) MRM chromatogram of peptide DLGEEENFA acquired with SRC#1. B) The product ion area ratios of LVTDLTK (dotp = 0.87) compared to the best matching NIST spectral library entry. C) Retention time comparison of MRM transitions. The retention time is indicated by the black vertical line and is measured at max peak height.

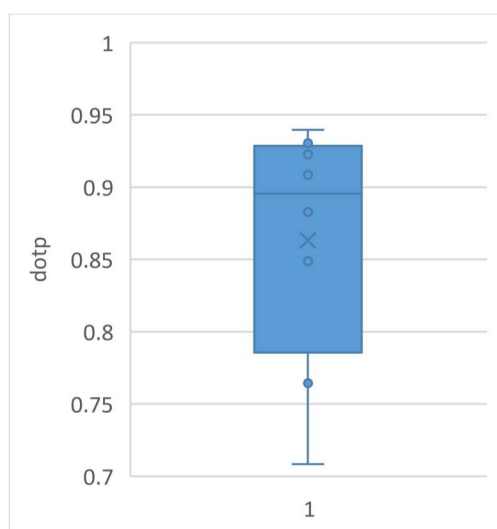


Figure 32: Average value distribution of identified HSA tryptic peptides (n=3). Raw data is found in Appendix, Table 32.

4.2.1 Gradient optimization

The last eluting peptide with SRC#1 was the basis for subsequent gradient optimization. Assuming the actual LC-pump MP delivery corresponds to the gradient as it was programmed, the last peptide eluted at ~12% B. The employment of the new and adjusted gradient, running from 1-15% B (SRC#2) with 100 pg of HSA standard on-column (**Figure 33**) positively impacted the separation of early eluting peptides. The enhanced peak separation was due to a decrease in the gradient steepness from 0.35 Δ [%B/min] in the new gradient compared to 0.51 Δ [%B/min] in SRC#1.

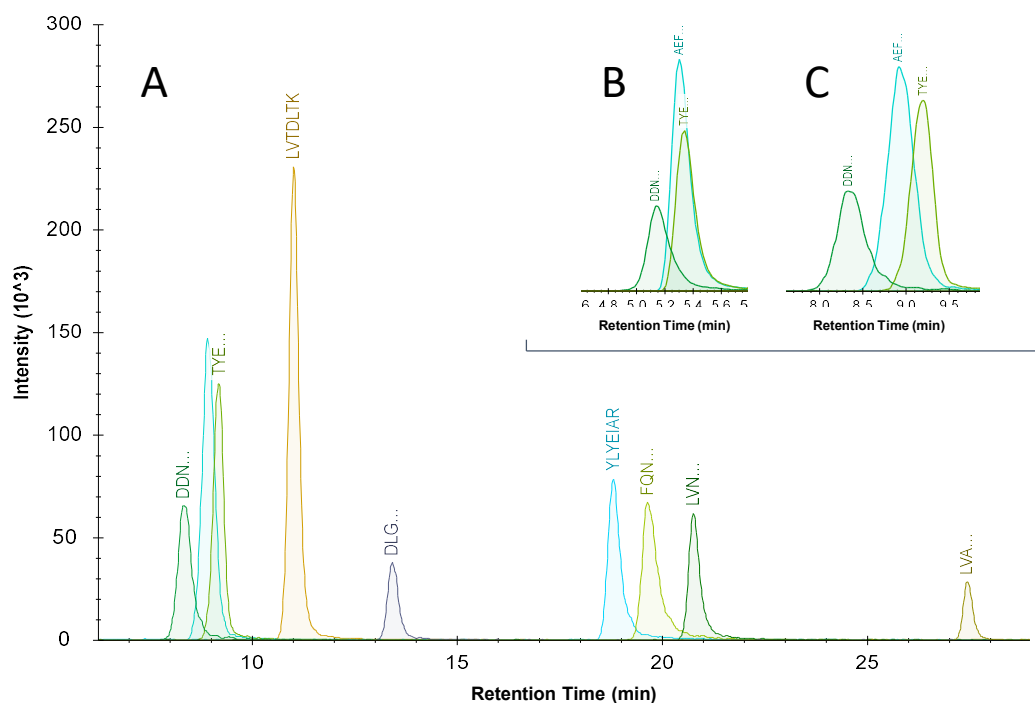


Figure 33: Chromatogram collection. A) Total chromatogram of HSA tryptic peptides from 100 pg of HSA standard on-column (n=1), recorded employing SRC#2. B) Separation of the partially coeluting peptide DDN..., TYE..., and AEF... employing SRC#1. C) Separation of the partially coeluting peptide DDN..., TYE..., and AEF... employing SRC#2.

Gradient length testing

The effect of the gradient steepness was further tested to investigate its effect on peak separation, signal intensity, and ion suppression. Gradient steepness was altered by changing the length of the linear gradient. It was suspected that a decrease in gradient steepness would

improve peak separation which in turn would reduce ion suppression and improve signal intensity.

The effects of $\Delta[\%B/\text{min}]$ were investigated by monitoring **A)** the total peptide peak area calculated by the sum of fragment peak areas and **B)** the change in the fragment peak area ratio distribution, which can indicate changes in ion suppression effects. Band broadening was additionally monitored by **C)** the full width at half maximum (FWHM). The magnitude of impact on these parameters by changing gradient steepness has been summarized in **Figure 34**.

From the charts in **Figure 34** it was concluded that further decreasing the $\Delta(\%B/\text{min})$, within the range that was tested, would not benefit the system performance. There was no observable effect on the total peak area (chart **B**) or the transition peak area ratio distribution (chart **C**). A decrease in $\Delta[\%B/\text{min}]$ was accompanied by an increase in band broadening (chart **A**), which counteracted any additional separation benefit. SRC#2 was kept unaltered for future analysis.

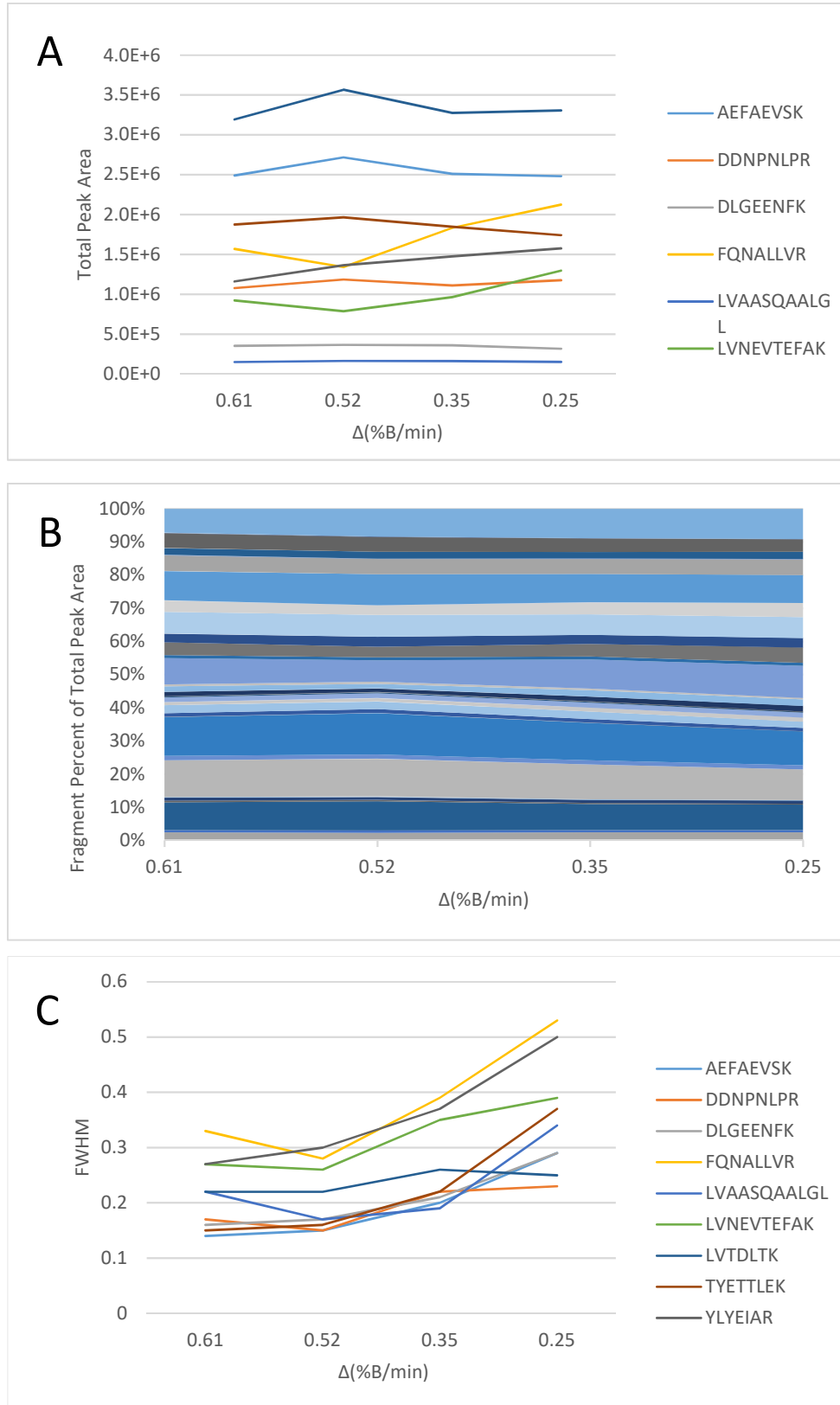


Figure 34: Effects of $\Delta[\%B/\text{min}]$ (x-axis) on platform performance endpoints with chromatographic data from 9 tryptic HSA peptides (100 pg HSA standard on-column, $n=1$) for **A**) the total peptide peak area. **B**) the fragment peak area ratio distribution and **C**) the effect of $\Delta[\%B/\text{min}]$ on the FWHM. Raw data is found in Appendix, Table 34, and Table 35.

4.2.2 Collision energy optimization

CE optimization of detectable peptides of HSA was performed to estimate the best CEs for ALT1 peptide determination based on their m/z value. **Figure 35** depicts the CE regression analysis results. The figure on the left (A) compares the optimized linear equation, in blue, to the “Thermo TSQ Quantiva” default equation in black. This default setting was already a good basis for CE generation, given that this exact instrument was employed. The chromatogram on the right (B) illustrates how the most intense signal (yellow peak, Step 5) from the CE ladder for a specific peptide was selected as a data point for the regression analysis.

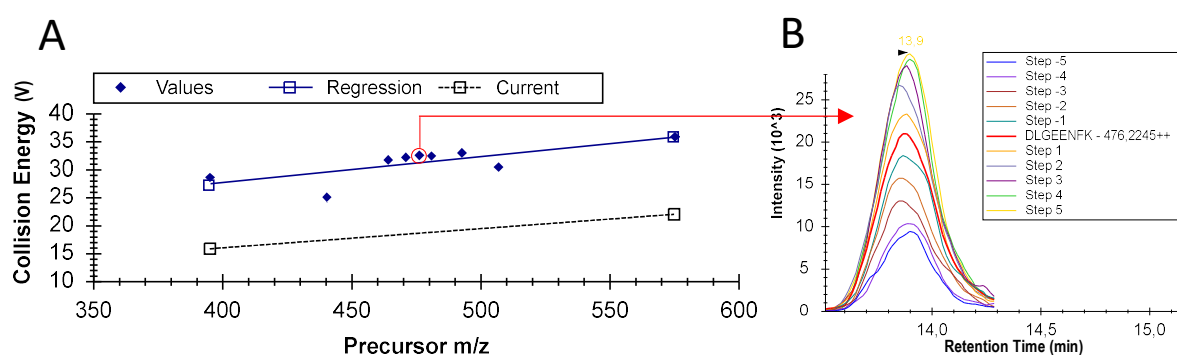


Figure 35: CE optimization with regression analysis for 9 HSA peptides from 100 pg HSA standard on-column ($n=2$). A) The bold line indicates the optimized equation for automated CE value generation, while the dotted line illustrates the Skyline default equation. B) Example MRM chromatogram of peptide DLGEENFK. Each color represents the signal intensity for a specific CE step. Chromatograms were acquired with SRC#2.

CE optimization achieved an average increase in signal intensity of 22%. Acquiring spectra with the individually optimized CE, that is, the individual CE constituting the data points in the linear regression analysis, was calculated to increase the signal intensity with an additional 5.7 % (see **Figure 36**). It was decided that the optimized CE equation should be used for CE generation for ALT peptides. The additional 5.7 % gain in signal intensity was not considered enough to perform separate optimization for ALT peptides.

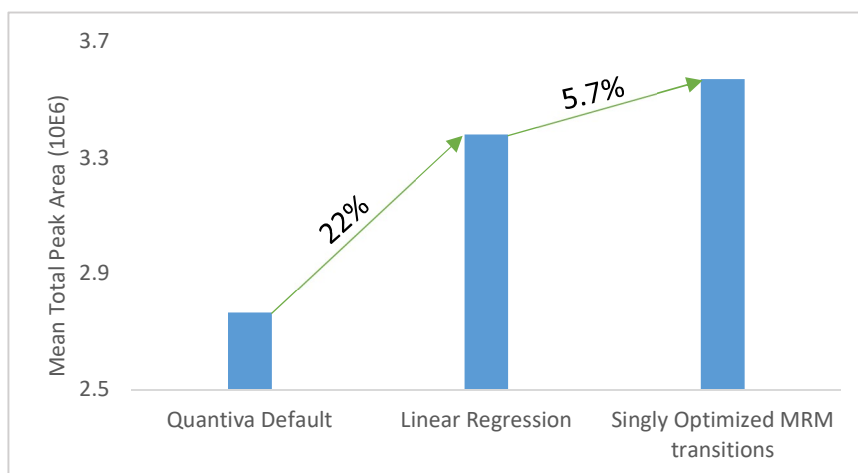


Figure 36: The effect of CE optimization on the mean total peak area (sum of MRM transitions) of 9 HSA peptides from 100 pg HSA standard on-column (n=1).

4.2.3 Retention time prediction

The built-in Skyline retention time prediction tool was employed for HSA peptides to perform retention time predictions of ALT1 peptides based on their SSRCalc values (see Appendix, section 7.1.4 for supplementary theory) for the same chromatographic conditions. The retention time regression analysis results for SRC#2 are presented in **Figure 37**. The coefficient of determination (R^2) was calculated to 0.941, which indicates that the linear equation offers a moderately good fit for the data points. The fit of the regression line was considered satisfactory for its purpose, given that it should only be used to supplement ALT peptide peak identification and determine if ALT peptides are expected to elute within the applied gradient.

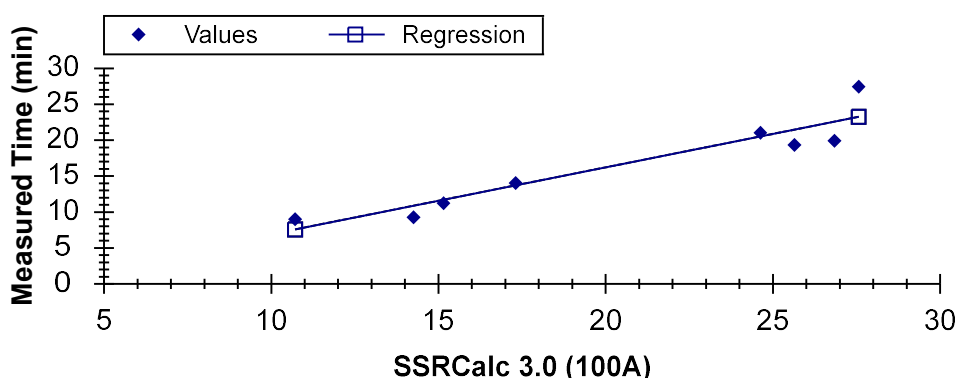


Figure 37: Linear regression analysis for measured elution times for 9 HSA peptides from 100 pg HSA standard on-column (n=1) Data was obtained with SRC#2. Data obtained from one replicate. Raw data is found in Appendix, Table 32.

In summary

An approach for optimizing LC-MS conditions has been established. The optimized conditions enabled the sensitive detection of signature peptide candidates and should now be applied for subsequent investigation of ALT1.

4.3 The investigation of alanine aminotransferase isof. 1

Having an optimized analysis platform established, subsequent steps were focused on ALT1 detection from a recombinant ALT protein source. Recombinant proteins are synthesized in non-human host cells, and are great high purity standards to establish signature peptides without matrix interferences [102]. The objective of these experiments was to confidently identify signature peptide candidates for ALT1 and select a signature peptide based on peptide abundance. Initial peptide selection was executed as per section 3.7.1 and the uniqueness was defined at the isoform level. The total protein content of recombinant ALT1 standard was estimated as per section 3.3 for preparative reagent adjustments and column-load estimation, see **Table 9**.

Table 9: Total protein concentration of ALT1 standard, n=2, two measurements per sample calculated from the calibration curve based on BSA absorption.

	Average total protein cons. (mg/mL)	Relative Std. (%)	n
Recombinant ALT standard	7.7	19	2

Initial peptide selection resulted in four peptides that qualified as signature peptides. The peptide sequences with their respective MRM transitions are listed in **Table 7**. Several attempts were made to detect these peptides. One of these detection attempts, for 2.5 ng ALT1 standard on-column, has been described in **Appendix**, section 7.4.7. Based on the estimation for the total protein content for the ALT1 standard, detection should be feasible with 2.5 ng protein column-load. A thorough investigation of the protein standard source documents revealed that the ALT standard, as delivered by the manufacturer, was solubilized in a buffer containing among others bovine serum albumin (BSA) to stabilize ALT enzyme activity. The concentration of ALT or the ALT-to-buffer ratio was not stated. The initial column load, which was based on the total protein content of the sample was thereby misinterpreted. The source document could, however, verify that only ALT isoform 1 was present in the sample. Increasing the protein column-load

incrementally from 2.5 ng to 250 ng and running an additional full scan (not shown) did neither produce an analyte signal.

An undiluted ALT1 standard sample, corresponding to a sub- μg protein column-load, was analyzed. **Figure 38** shows the total chromatogram and **Figure 39** shows the chromatograms for the individual peptides. All signature peptide candidates were detected.

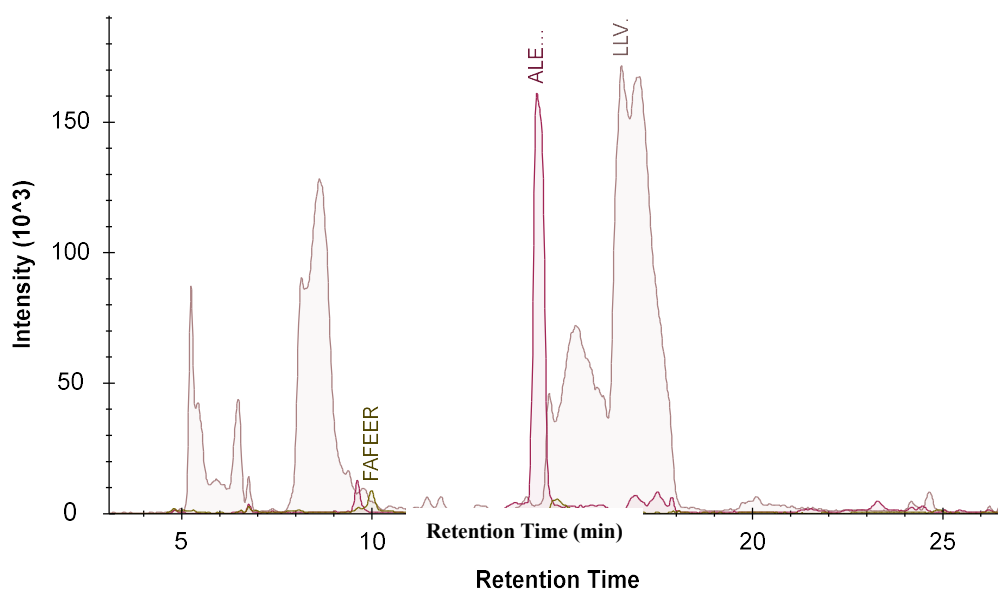


Figure 38: Total chromatogram of ALT1 signature peptide candidates from sub- μg ALT1 standard (n=1) acquired with SRC#2. Raw data is found in Appendix, Table 28.

The peak shapes for ALELEQERL and FAFEER were symmetrical and the MRM transitions generated an analyte signal with relatively low noise. The peak area for ALELEQERL was 19.4-fold greater than for FAFEER. The MRM transitions for peptide LLVAGEGHTR had a relatively high signal intensity and relatively high noise as depicted in **Figure 38**. The peak assigned to LLVAGEGHTR had poor peak shape for all MRM transitions, possibly caused by a column-overload.

The peptide ALELEQERL had a dotp value of 0.73 and eluted close to the predicted elution time. These factors gave confidence in the trueness of the peak assignment. The peptide FAFEER eluted within the predicted elution window, however, no dotp value was automatically displayed for the assigned peak. The low peak intensity might have caused the Skyline algorithm to disregard the peak due to fragment ratios measurements of too great uncertainty. The dotp value and retention time for peptide LLVAGEGHTR were considered

non-assessable due to the irregular peak shape. Thus, column-load adjustments had to be made before making a final decision on what peptide should represent ALT1. From current observations, LLVAGEGHTR was considered to have the greatest signal intensity.

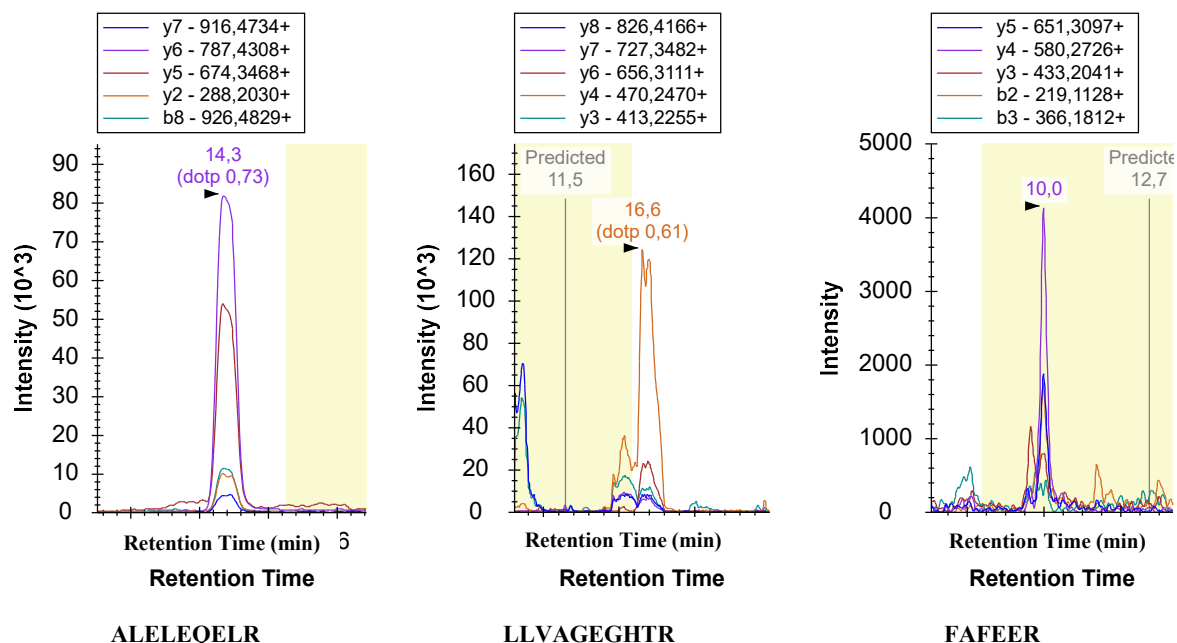


Figure 39: MRM chromatograms of ALT1 signature peptide candidates from sub- μ g column-load of ALT1 standard (n=1) acquired with SRC#2. Raw data is found in Appendix, Table 28.

When comparing the signal intensities in the total chromatogram to the signal intensities in the MRM chromatograms for the individual peptides, it was discovered that a bug in the Skyline software caused these to differ significantly. This was especially noticeable for the peptide ALELEQELR which had a signal intensity above 150 (10^3) in the total chromatogram, compared to a signal intensity of 80 (10^3) in the individual chromatogram. By looking at the raw output file for the max peak heights (**Table 10**) it became evident that the individual chromatograms constitute a more accurate representation of the raw data, and should therefore, be used for visual peptide abundance estimation. Peptide eliminations were however not affected by this, as peak area was used to quantify peptide abundance.

Table 10: Max peak height of ALT signature peptide candidates acquired with SRC#2 from undiluted ALT standard (n=1).

Peptide	Max Height
ALELEQELR	81658
LLVAGEGHTR	124490
FAFEER	4141

Necessary change of analytical column

The commercial column used with SRC#2 (Acclaim PepMap™ 100, 75 µm x 5 cm, nanoViper, C18, 3 µm, 100Å) was no longer operative due to a column defect. Going forward, in-house packed columns were employed (Accucore, 75 µm ID x 5 cm L, C18, 2.6 µm, 150 Å) with SRC#3 and (Accucore, 50 µm ID x 5 cm L, C18, 2.6 µm, 150 Å), with SRC#4. A reduction in particle size from 3.0 µm for the commercial column down to 2.6 µm for the in-house packed columns, would theoretically decrease the size of the eddy dispersion, in turn improving the column efficiency [103]. A reduction in column ID from 75 µm to 50 µm would theoretically increase the sensitivity of the method. Both these improved features were desirable for ALT1 detection. A column replacement did require gradient adjustments, which also caused elution time predictions to become invalid.

Figure 40 shows the chromatogram for a 500 ng protein column-load of ALT1 standard obtained from a new trypsination batch. **Figure 41** shows the chromatograms for the individual ALT1 peptide candidates recorded with their respective MRM transitions. The peptides LLVAGEGHTR and FANFEER had dotp values of 0.52 and 0.53, respectively. The relatively low dotp values did neither add confidence in peptide peak assignment, nor did they disprove the presence of the peptides. The peak shape was considered symmetrical for both peptides and the overall noise was lowered compared to the previous run (**Figure 39**). It was noticed that the signal intensity of peptide ALELEQELR was much lower compared to the previous run and no dotp value could be assigned to this peak. Although, the retention times were non-comparable due to the column replacement, the retention order should be unaffected, if equal selectivity of the C18 materials for the respective columns is assumed. This, however, was not the case for ALELEQELR, which eluted last in the chromatogram in **Figure 40**, but second in the previous run (**Figure 39**).

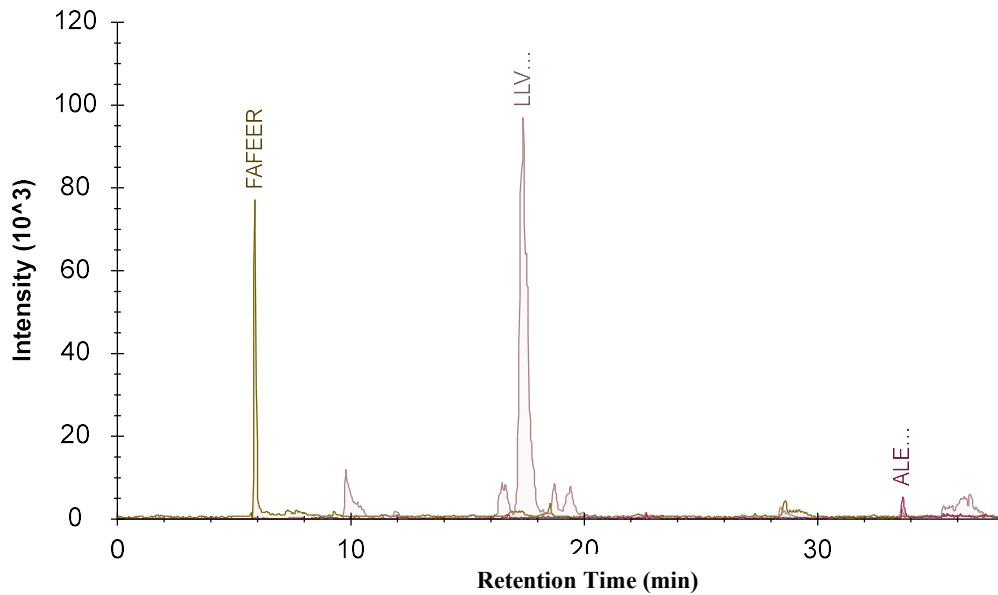


Figure 40: Total chromatogram of ALT1 signature peptide candidates from 500 ng ALT1 standard on-column, n=1, acquired with SRC#3. Raw data is found in Appendix, Table 29.

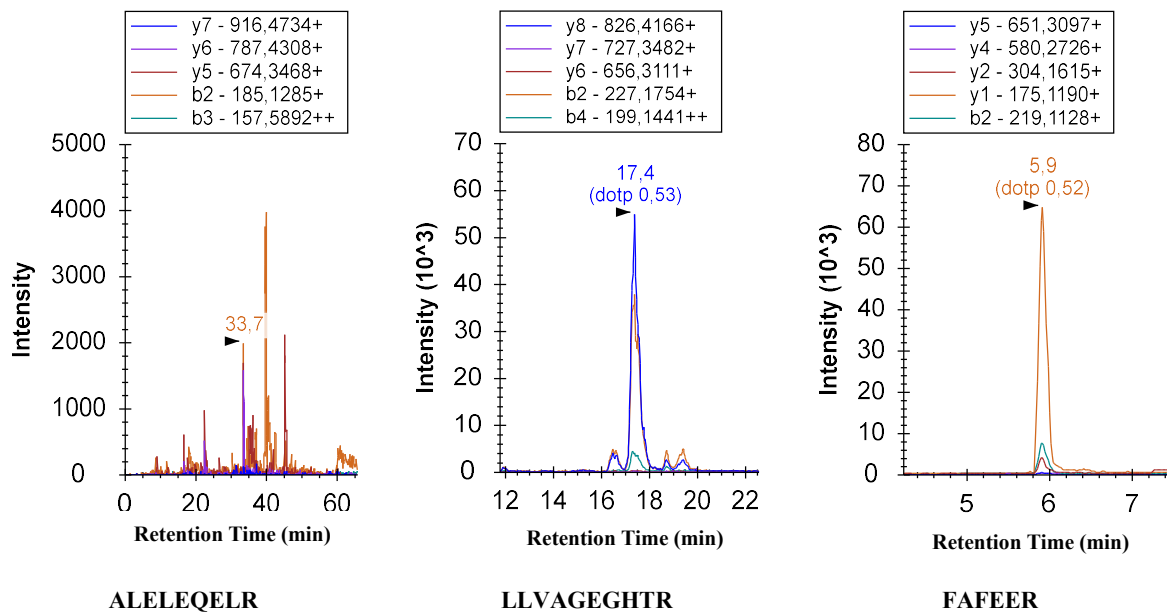


Figure 41: Individual MRM chromatograms of ALT1 signature peptide candidates from 500 ng ALT1 standard on-column, n=1, acquired with SRC#3. Raw data is found in Appendix, Table 29.

A second library (NIST HCD-orbitrap) was imported into Skyline, which was intended to add transitions to the current spectral library (NIST Iontrap) so that improved MRM selections for ALT1 peptides could be performed. It was discovered post-analysis, that the import of the new spectral library replaced MRM transitions recorded from previous runs, instead of

supplementing to the already existing MRM transitions. **Table 11** contains information on what fragments that were replaced with the import of the NIST HCD-orbitrap spectral library. The import of the new library does not explain the poor signal for ALELEQELR, given that the two most abundant fragments were recorded in both runs.

Table 11: Replacements of fragments from NIST Iontrap spectral library to NIST HCD-orbitrap spectral library for peptide MRM transitions of ALT isoform 1. The abundance rank is based on the fragment peak area.

Peptide	Original fragments [abundance rank based on peak area, Figure 39]	Replaced by [abundance rank based on peak area, Figure 41]
ALELEQELR	b8+[3], y2+[4]	b2+[n/a], b4+[n/a]
LLVAGEGHTR	y4+[1], y3+[2]	b2+[2], b4++[3]
FAFEER	y3+[2], b3+[5]	y1+[1], y2+[3]

The chromatogram was recorded as a part of a dilution series, and only one replicate was recorded. The remaining samples from the dilution series did not produce any analyte signal. Drawing conclusions to the absence of ALELEQELR could not be justified from one chromatogram only. Due to time constraints with ordering internal standards for the signature peptide, a decision had to be made based on the available data, which meant that ALELEQELR was eliminated from this selection. Based on the recorded chromatograms and the peak areas obtained from the latter chromatogram (**Figure 42**) it was decided that LLVAGEGHTR should be the signature peptide for ALT1. The total peak area for LLVAGEGHTR was greater and the bulk of the area stemmed from two MRM transitions rather than from one, as for FAFEER, resulting in a more reliable detection of the peptide. Ideally, the experiment should have been repeated with more replicates.

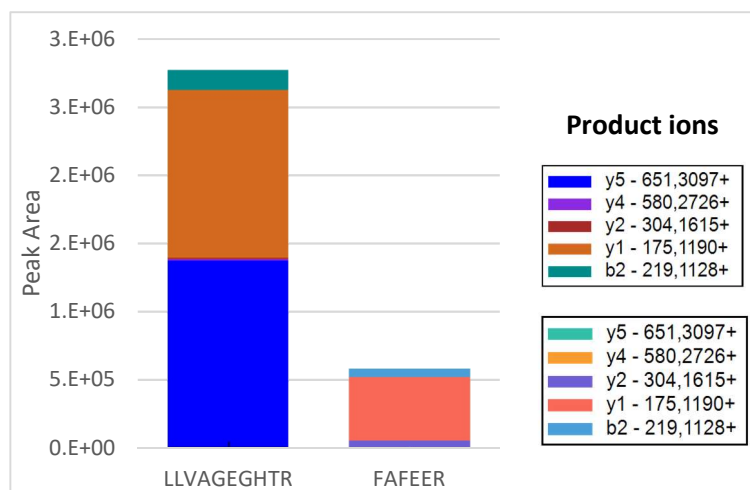


Figure 42: Peak area of ALT1 peptides LLVAGEGHTR and FAFEER including product ion peak area distribution from 500 ng ALT1 standard on column (n=1). Acquired with SRC#3. Raw data is found in Appendix, Table 29.

In summary

From the investigation of ALT1, four signature peptide candidates were identified. Based on having the largest peak area, LLVAGEGHTR was selected as the signature peptide to infer the presence of ALT1. Proceeding experiments focused on quantitative aspects of MRM assay development for LLVAGEGHTR.

4.4 Quantification using signature peptide – LLVAGEGHTR

The objective of proceeding experiments was to develop a method for ALT1 absolute quantification. This involved, choosing a suitable quantification method and decide on what peptide fragments for LLVAGEGHTR should infer the concentration of ALT1 in an unknown sample. These experiments were performed with LLVAGEGHTR peptide standards.

As confusion with MRM generation had arisen during ALT1 standard analysis (see section 4.3), a new Skyline file was created for quantitative purposes and MRM selection was repeated using both the NIST Iontrap and NIST HCD-orbitrap spectral libraries. The most abundant fragments

for LLVAGEGHTR from three replicates after MRM reselection were determined to be fragment y8⁺, y7⁺, and y8⁺⁺, as depicted in **Figure 43**. These fragments became the potential candidates for ALT1 absolute quantification. Selecting appropriate transitions is, at least, as important as selecting a signature peptide. This is to assure that quantification results are interpreted without the influence of mass interferences from the matrix.

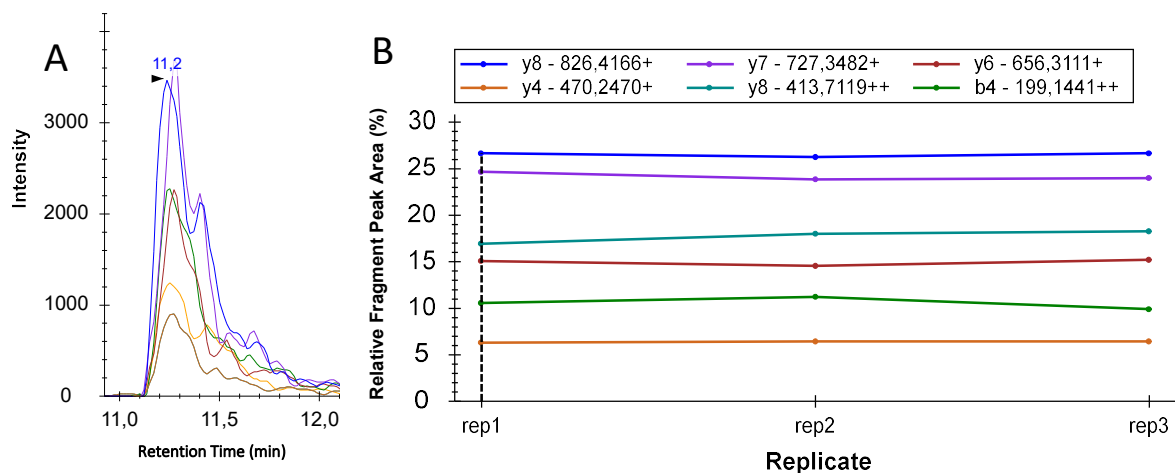


Figure 43: Analysis of 1.0 fmol LLVAGEGHTR standard on-column (n=3), acquired with SRC#4 A) MRM chromatogram of LLVAGEGHTR with color corresponding transitions B) Relative fragment peak area (%) to total peak area for LLVAGEGHTR. Acquired with SRC#4. Raw data is found in Appendix, Table 30.

4.4.1 Considerations with quantification

Matrix-matched and non-matrix matched external calibration was considered for the absolute quantification of ALT1. Standard addition was not considered due to requirements of larger sample sizes not available for the hepatic organoids that were used for upcoming experiments. For the comparison of calibration methods, cell medium was selected as the matrix. This decision was based on a secondary study objective to produce an ALT1 release in hepatic organoids upon exposure to toxic doses of APAP, which “release” should be quantifiable in the cell medium where the organoids are stored. Matrix matched and non-matrix matched calibration solutions were compared to determine whether the amount of signal suppression and mass interferences in the matrix-matched calibration solutions significantly impacted the quantification of ALT1. Signal suppression effects were quantified by the change in the slope of the calibration curve for the respective fragment candidates. The standard BC3 was removed due to problems with the autosampler injection.

Statistics were performed for the calibration curves having the greatest slope deviation in the organoid medium compared to that of the aqueous standards (Fragment y8⁺⁺). The test outcome was assumed valid for the remaining fragments, as the impact of matrix distortion was less evident for these fragments. A Welch's t-test for unequal variances was selected, as the group variances (non-matrix vs matrix-matched) for the slope of the calibration curve differed by more than 2-fold. With a P-value ($T \leq t$, two-tailed) of 0.53 it was concluded that the slopes of the calibration curves did not significantly differ from each other, hence the suppression effects and mass interferences were not statistically significant for ALT1 quantification. The statistical hypothesis is found in section 3.11. Raw data and the test output is found in **Appendix, Table 40** and **Table 41**, respectively. Going forward, non-matrix matched calibration standards were used for the quantification of ALT1.

4.4.2 MRM transition qualifier- and qualifying ion

As suggested by Kuzyk et. al (2013) one ion should be selected for the quantifying MRM transition and one ion for a qualifying MRM transition [93]. The qualifying transition is useful if an unexpected interference, having equal m/z value as the analyte, coelutes with the analyte/IS. This can then be detected by comparing the intensities of the quantifying transition with the qualifying transition in the standard solution and sample, as depicted in **Figure 44**. If the peak area ratio of these ions differs in the standard solution compared to the sample, matrix ion suppression effects may be present.

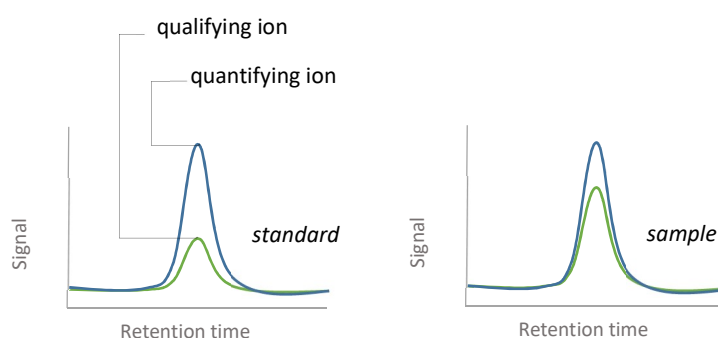


Figure 44: Example of how the qualifying ion can be used to detect unexpected interferences in the sample. The figure in the left shows the peak area ratio of the quantifying and qualifying ion in a standard solution. The figure on the right shows the ratio between the same ions in a sample.

The assignment of the quantifying and control transition was determined by 1) the fragment signal intensity and 2) the “quality” of the calibration curve. The latter will be explained in more detail in an upcoming section. These test variables were considered the most important, because, 1) the signal intensity defines the detection limits for the quantification method, and 2) the quality of the calibration curve defines the reliability of the quantification results. The best candidate was assigned to the quantifying transition and the second best was assigned the control transition.

Fragment signal intensity

The fragment having the greatest signal intensity was determined by the fragment peak area. The sample F2 was identified as an outlier in the dataset for fragment y8+, as depicted in the boxplot in **Figure 45**. The replicate was validly removed with a Grubb’s test (see section 3.11 and Appendix, section 7.4.6). Boxplot descriptives can be found in Appendix, section 7.1.3.

A single-factor ANOVA test (statistical hypothesis in section 3.11) with a P-value ($F_{crit} \leq F$) of $6.1 \cdot 10^{-9}$ for the between-group variances of the three datasets showed a statistical difference in the fragment peak areas. The raw data is found in **Appendix, Table 42** and the ANOVA raw output is presented in **Appendix, Table 43**. The ANOVA test did not identify the significantly outlying datasets, which suggested to run a least significance difference (LSD) test to identify the outlying dataset. The fragment y8++ had the lowest average fragment peak area. The LSD test confirmed that the average of the peak areas for the y8++ fragment was significantly different from the peak areas for fragment y8+ and y7+. The calculation method for the LSD is found in Appendix, section 7.4.6. Based on these results, the fragment y8++ was eliminated as a contender for the qualifying- and control MRM transition.

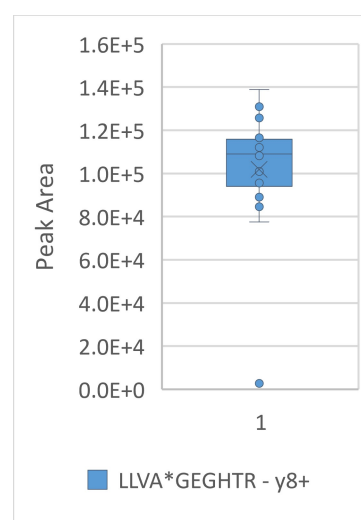


Figure 45: Boxplot of Peak Area for LLVA*GEGHTR -> y8+, 1.0 fmol on-column (n=18), recorded with SRC#4. Raw data is found in Appendix, Table 36.

Calibration curve

The next factor which was assessed was the “quality” of the calibration curve. The quality was determined by the goodness-of-fit (R-squared), the sensitivity of detection (slope) and the significance of the intercept, which has been summarized for fragment y8+ and y7+ in **Table 12**; In addition to the distribution of the relative standard deviation (rel. std.) of the data points, the distribution of regression residuals and lastly the prediction interval.

Table 12: Linear regression analysis - Quality of calibration curve parameters. Comparison of y8+ and y7+ (0.1-10 fmol LLVAGEGHTR standard on column, n=3, SRC#4)

Fragments	Slope	Intercept	R ²	P-value for intercept
y8+	0.9541	-0.0612	0.990	0.8
y7+	0.9998	-0.1512	0.986	0.6

There was no conspicuous difference in the data from the regression analysis for the two fragments (**Table 12**). The slope of 0.9998, and hence the sensitivity of detection for the y7+ fragment was slightly better than the slope of 0.9541 for fragment y8+; The R-squared of 0.990, however, was marginally greater for y8+. The P-value, which denotes the significance of the intercept being different from zero, was above 0.05 for both calibration curves – this is a coveted feature since a zero-stimulus on the x-axis should produce zero response on the y-axis.

The calibration curves (**A**), including the boxplot for the relative standard deviation (**B**) and the regression residuals chart (**C**) for fragment y8+ and y7+ has been summarized in **Figure 46**. The relative std. should ideally be approximately equal, and small for all data points across the calibration curves. The distribution of rel. std. behaves similarly for both fragments, but the mean was shifted upwards for y7+. This trend was also observed in the distribution of the regression residuals, which ideally should be evenly distributed around the x-axis. Since the distribution was approximately the same for both fragments, this data did not impact the assignment of the fragments. The data only showed that measurement precision was better for y8+. Statistical analysis was not feasible, since only one set of rel. std. and regression residuals were available for the three replicate data sets.

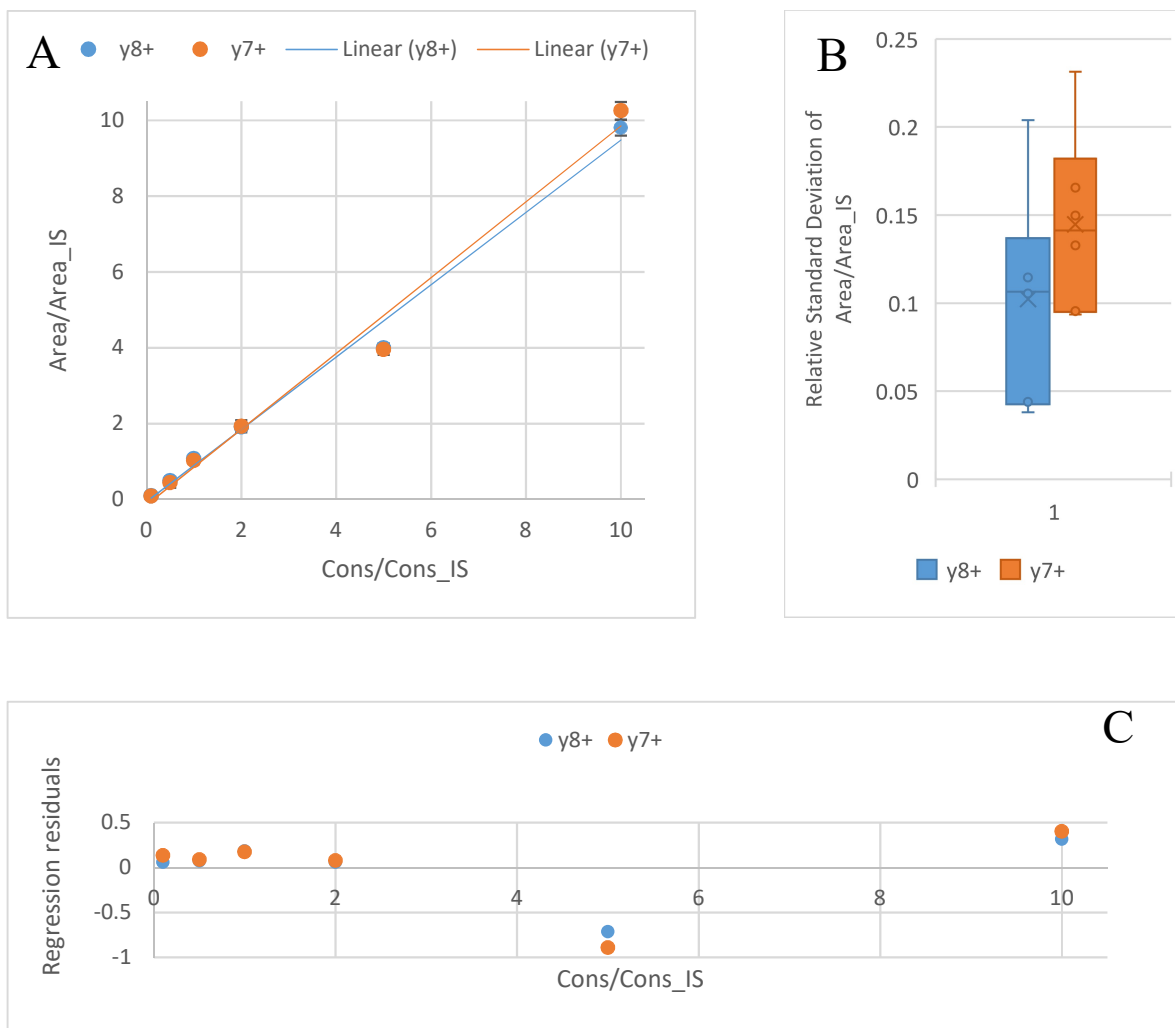


Figure 46: Quality of calibration curve test parameters for LLVAGEGHTR fragment y8+ and y7+ from 0.1-10 fmol LLVAGEGHTR standard on column, n=3, SRC#4 A) Calibration curves for fragment y8+ and y7+. Raw data in Appendix, Table 38. B) Boxplot of the relative standard deviation of the Analyte to IS ratio. Raw data in Appendix, Table 38 C) Distribution of regression residuals for y8+ and y7+. Raw data in Table 37.

Lastly, the prediction interval was assessed. Prediction interval descriptives are found in **Appendix**, section 7.1.3. The prediction interval is also affected by the nature of the sample measurement. That is, the peak area ratio mean (\bar{y}_{obs}) and the number of observations (n). Since no unknown sample was measured, these were held at the arbitrary numbers 5 and 3, respectively, see **Table 13**. The calculation method for the prediction interval is demonstrated in **Appendix**, section 7.4.6.

Table 13: Prediction intervals for fragment y8+ and y7+ from 0.1-10 fmol LLVAGEGHTR standard on column, n=3, SRC#4

Fragment ion	\bar{y}_{obs}	n	$x_{predicted}$	Prediction (95% CI)
y8+	5	3	5.06	± 0.89
y7+	5	3	5.15	± 1.05

A smaller prediction interval of ± 0.89 for y8+ compared to ± 1.05 for y7+, suggests that quantification using the y8+ fragment was more precise and hence better suited for quantification of ALT1. It was decided that the fragment y8+ was the best suited quantifying ion and that the fragment y7+ was best suited as the qualifying ion based on the prediction interval. Given that the other test parameters (e.g. the slope of the calibration curve and the distribution of regression residuals) showed similar outcomes for both fragments, these did not affect the identity assignment of the two fragments. Although only the prediction interval showed decisive results that affected decision making, it does not imply that the other factors assessed were less important. The prediction interval cannot reflect how the datapoints are distributed, like the regression residual, and the goodness-of-fit, can.

In summary

From the investigation of LLVAGEGHTR fragment candidates it was established that non-matrix matched calibration was sufficient for ALT1 quantification in organoid medium. Furthermore, it was established that fragment y8+ and y7+ were best suited as the quantifying and qualifying MRM transition, respectively. With all premises for ALT1 quantification in place, proceeding experiments focused on method application for biological samples.

4.5 ALT1 in biological samples

The Covid-19 pandemic – deviations from planned works

On the *12-Mar.-2020* the government implemented strict measures to protect the population at large from the ongoing SARS-CoV-2 virus outbreak. These measures, including the shutdown of the University of Oslo, unfortunately, impeded the progression of this work. Concisely formulated, the completion of LC-MS determination of ALT1 in hepatic organoids and the completion of sample preparation of APAP/NAPQI-induced ALT1 in organoid medium including the subsequent LC-MS analysis, could not be proceeded due to government restrictions. This section will consequently primarily discuss experimental design considerations.

4.5.1 The presence of ALT1 in organoids

The objective of this experiment was to document the presence of ALT1 in hepatic organoid cell cytosol. This finding would then justify the conducting of experiments of APAP-induced ALT1 release from hepatic organoids. **Figure 47** includes the chromatogram of LLVAGEGHTR measured in lysed hepatic organoids (n=1), with chromatographic data shown in **Appendix, Table 31**. The signal intensity and peak area was too low to reliable state that the signal can be attributed to the presence of ALT1, and not being a result of instrument noise. Since the sample was diluted 100X, it was planned to increase the concentration in a future experiment, to see if the signal intensity would increase correspondingly.

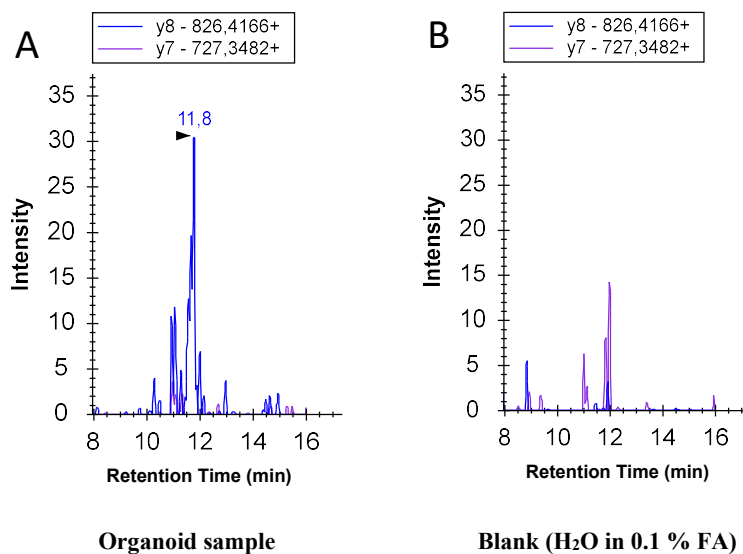


Figure 47: MRM chromatograms of LLVAGEGHTR vs blank. A) Chromatogram of signature peptide LLVAGEGHTR recorded for ALT1 from in-gel digestion of hepatic organoids (n=1, ~ 60 organoids, excised from gel ~60 kDa, reconstituted in 500 μ L H₂O in 0.1 % FA and diluted 100x). B) Chromatogram of blank sample (H₂O in 0.1 % FA). Acquired with SRC#4. Raw data in Appendix, Table 31.

4.5.2 APAP- and NAPQI-induced ALT1 release in hepatic organoids

The objective of this experiment was to determine a possible APAP and NAPQI concentration-dependent release of ALT1 in hepatic organoids, measuring ALT1 in organoid medium. The final incubation concentration ranges of APAP and NAPQI with hepatic organoids were 20 - 50 mM and 2 – 5 mM, respectively. The concentration range for APAP was chosen based on a study by Gamal, W., Treskes, P., Samuel, K. et al., where 5 – 20 mM of APAP was incubated with HepaRG cells (immortalized cell line). In the study, they found that only the higher doses of APAP (10 and 20 mM) significantly compromised cell membrane integrity (~70% vs control) [104]. It was therefore decided to test concentrations in the range of 20 to 50 mM.

APAP-induced toxicity is dependent on CYP2E1 and CYP1A2 activity for the conversion of APAP to its toxic metabolite NAPQI (see section 2.3.1). For the organoids that were used during this experiment, the expression of these enzymes was yet not established. It was therefore decided to incorporate NAPQI-induced ALT1 release, as well. The NAPQI concentration range chosen based on studies showing an *in vivo* conversion ratio from APAP to NAPQI of approximately 5 – 10% [105, 106]. Taking a conservative stance and assuming the “worst case scenario”, the upper limit of conversion from APAP to NAPQI was chosen for

this experiment, resulting in a respective concentration range of 2 – 5 mM. Upon incubation with the respective compounds, it was planned to perform an in-solution digestion of the samples followed by quantification of ALT1 with the finalized MRM assay. The outcome of this experiment would demonstrate the applicability of the finalized MRM method for ALT1 quantification. Additionally, it could reveal if a linear relation between the concentration of ALT1 in organoid medium and the concentration of APAP and NAPQI can be established. The concentration of ALT1 in the APAP-incubated samples would also reveal if the CYP2E1 and CYP1A2 activity in hepatic organoids would convert enough APAP to NAPQI to subsequently produce a toxic response inducing the release of ALT1. If, that was the case, it would argue in favor of the implementation of hepatic organoids in preclinical DILI assessment.

In summary

Applying the here described MRM assay for the analysis of hepatic organoids, could indicate the presence of ALT1. Given that the signal was low, further testing is needed to confidently state the presence of ALT1. No statement could be made about APAP- and NAPQI-induced ALT release in hepatic organoids.

4.6 Experimental achievements – A summary

A revisit of the planned workflow of this study is presented in **Figure 48** and includes the results which were achieved during the preliminary study with HSA and the investigational experiments with ALT1. Experiments planned for the method application part of this workflow were unfortunately impeded, but will hopefully be proceeded in the future.

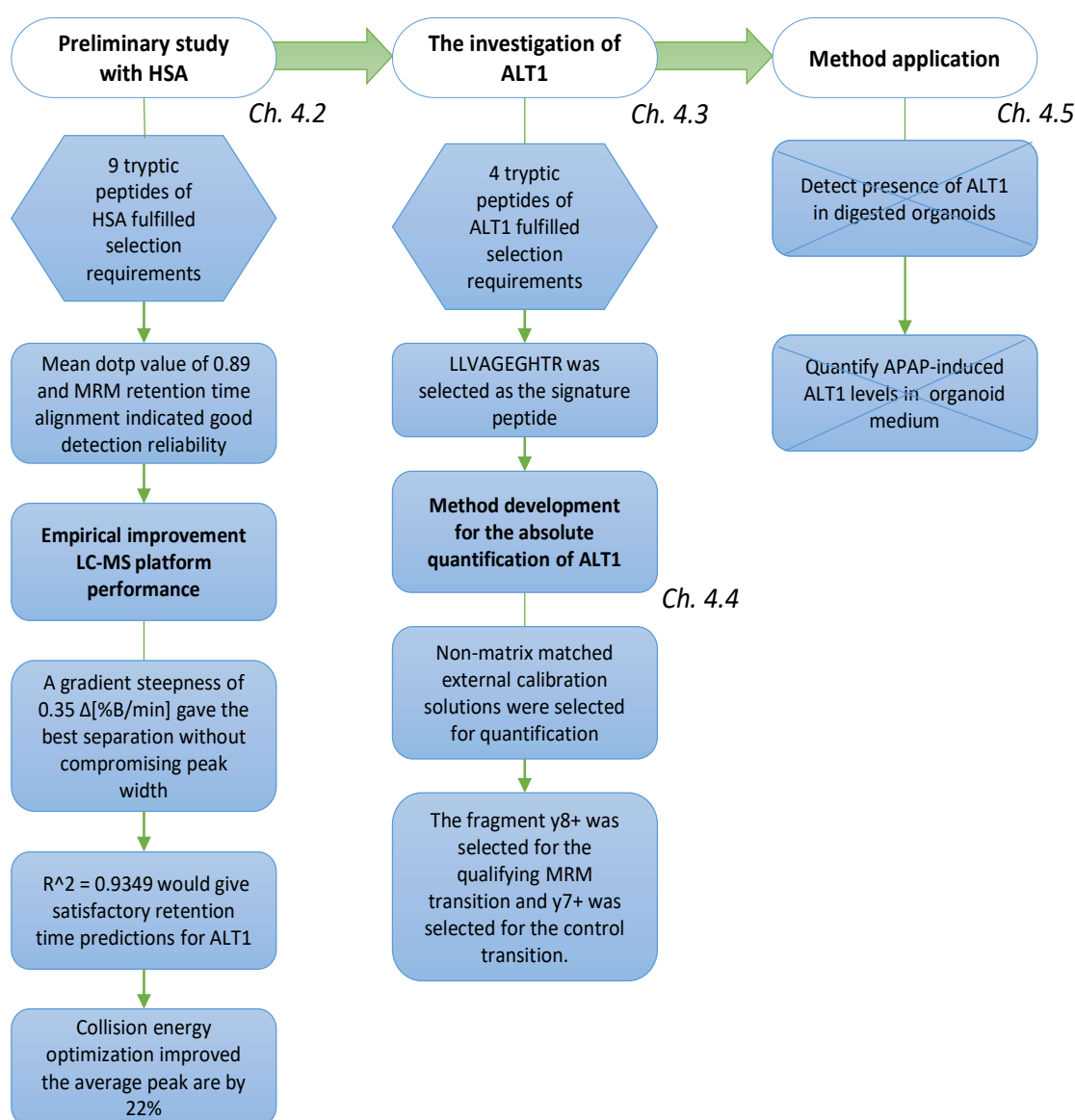


Figure 48: Experimental achievements of this thesis for ALT1 MRM method development.

5 Concluding remarks and further work

This thesis was devoted to the development of a sensitive nanoLC-MS MRM assay for the absolute quantification of the DILI biomarker ALT1. In an effort to provide a supplementary or alternative approach for preclinical animal studies, MRM assay development was tailored for the detection of DILI in the advanced cell-based model organoids. To demonstrate the practical applications for the here described method, a correlation between APAP toxicity and ALT1 release was to be established. This work demonstrated that MRM assays are suitable for ALT1 quantifications through a thorough assessment of signature peptide candidates and corresponding MRM fragments. More specifically, the peptide LLVAGEGHTR with the corresponding fragments y8+ and y7+ were selected as the best candidates for selectively infer the presence of ALT1. It should also be highlighted that the successful incorporation of an optimized nanoLC-MS platform will allow for the analysis of small and valuable samples. This study was not able to establish a correlation between APAP toxicity and ALT1 release in organoids, due to extraordinary circumstances that affected the planned workflow of experiments.

The here described method can quantify proteins on an isoform level. This feature is uncommon for currently existing ALT assays. As the two isoforms of ALT are expressed in different organs, their distinction can help to prevent the confusion of hepatic injury with extrahepatic injury. Furthermore, the general workflow of method development is easily adaptable, which enables the assay to incorporate several protein biomarkers for DILI assessment. Covering the assessment of multiple biomarkers in one single assay, can help to simplify DILI detection in the future.

Further work

Further work should focus on method application to established if a relation between APAP and ALT1 in hepatic organoids is achievable. This would not only demonstrate method applicability but would also argue for the implementation of organoids for preclinical safety assessment. Furthermore, method validation in line with FDA guidelines [107] alongside method limitations regarding detection limits should be implemented.

6 References

1. Amaratunga, D., H. Göhlmann, and P.J. Peeters, 3.05 - *Microarrays*, in *Comprehensive Medicinal Chemistry II*, J.B. Taylor and D.J. Triggle, Editors. (2007), Elsevier: Oxford. p. 87-106.
2. Pharmaceutical Research and Manufacturers of America. *Drug Discovery and Development: Understanding the R&D Process*. (2007) [cited 2019/10/10]; Available from: http://cmidd.northwestern.edu/files/2015/10/Drug_RD_Brochure-12e7vs6.pdf.
3. European Medicines Agency. *ICH M3 (R2) Non-clinical safety studies for the conduct of human clinical trials for pharmaceuticals*. (2013); Available from: <https://www.ema.europa.eu/en/ich-m3-r2-non-clinical-safety-studies-conduct-human-clinical-trials-pharmaceuticals>.
4. U.S Food and Drug Administration. *Investigational New Drug (IND) Application*. [cited 2019/06/11]; Available from: <https://www.fda.gov/drugs/types-applications/investigational-new-drug-ind-application>.
5. U.S Food and Drug Administration. *The Drug Development Process*. [cited 2019/10/01]; Available from: <https://www.fda.gov/patients/learn-about-drug-and-device-approvals/drug-development-process>.
6. Junhee, S., H.S. Warren, G.C. Alex, et al., *Genomic responses in mouse models poorly mimic human inflammatory diseases*. *Proceedings of the National Academy of Sciences*, (2013). 110(9): p. 3507.
7. Martignoni, M., G.M.M. Groothuis, and R. de Kanter, *Species differences between mouse, rat, dog, monkey and human CYP-mediated drug metabolism, inhibition and induction*. *Expert Opinion on Drug Metabolism & Toxicology*, (2006). 2(6): p. 875-894.
8. van Tonder, J.J., V. Steenkamp, and M. Gulumian, *Pre-Clinical Assessment of the Potential Intrinsic Hepatotoxicity of Candidate Drugs*, in *New Insights into Toxicity and Drug Testing*. (2013), IntechOpen.
9. Weaver, R.J. and J.-P. Valentin, *Today's Challenges to De-Risk and Predict Drug Safety in Human "Mind-the-Gap"*. *Toxicological Sciences*, (2018). 167(2): p. 307-321.
10. Watkins, P.B., *Drug safety sciences and the bottleneck in drug development*. *Clinical Pharmacology & Therapeutics*, (2011). 89(6): p. 788-90.
11. Need, A.C., A.G. Motulsky, and D.B. Goldstein, *Priorities and standards in pharmacogenetic research*. *Nature Genetics*, (2005). 37(7): p. 671-81.
12. U.S Food and Drug Administration. *Guidance for Industry Drug-Induced Liver Injury: Premarketing Clinical Evaluation* (2009) [cited 2020/01/01]; Available from: <https://www.fda.gov/media/116737/download>.
13. Berne, R.M., M.N. Levy, B.M. Koeppen, et al., *Berne & Levy physiology*. (2008), Philadelphia, PA: Mosby/Elsevier.
14. Arjun Kalra, F.T., *Physiology, Liver*. StatPearls Publishing.
15. Robertson, D., *First pass metabolism*. *Nurse Prescribing*, (2017). 15(6): p. 303-305.
16. King, D. *Liver*. [cited 2020/10/01]; Available from: <http://www.siumed.edu/~dking2/erg/liver.htm>.
17. Lammert, C., E. Bjornsson, A. Niklasson, et al., *Oral medications with significant hepatic metabolism at higher risk for hepatic adverse events*. *Hepatology*, (2010). 51(2): p. 615-620.

18. Taxak, N. and P.V. Bharatam, *Drug metabolism*. Resonance, (2014). 19(3): p. 259-282.
19. Le, J. *Drug metabolism (Professional Version)*. [cited 2019/10/09].
20. David, S. and J.P. Hamilton, *Drug-induced Liver Injury*. US gastroenterology & hepatology review, (2010). 6: p. 73-80.
21. Roth, R.A. and P.E. Ganey, *Intrinsic versus Idiosyncratic Drug-Induced Hepatotoxicity—Two Villains or One?* Journal of Pharmacology and Experimental Therapeutics, (2010). 332(3): p. 692.
22. Kaplowitz, N., *Chapter 1 - Drug-Induced Liver Injury: Introduction and Overview*, in *Drug-Induced Liver Disease (Third Edition)*, N. Kaplowitz and L.D. DeLeve, Editors. (2013), Academic Press: Boston. p. 3-14.
23. Kullak-Ublick, G.A., R.J. Andrade, M. Merz, et al., *Drug-induced liver injury: recent advances in diagnosis and risk assessment*. Gut, (2017). 66(6): p. 1154-1164.
24. Mosedale, M. and P.B. Watkins, *Drug-induced liver injury: Advances in mechanistic understanding that will inform risk management*. Clinical Pharmacology & Therapeutics, (2017). 101(4): p. 469-480.
25. Nourjah, P., S.R. Ahmad, C. Karwoski, et al., *Estimates of acetaminophen (paracetamol)-associated overdoses in the United States*. Pharmacoepidemiology and Drug Safety, (2006). 15(6): p. 398-405.
26. Jaeschke, H., Y. Xie, and M.R. McGill, *Acetaminophen-induced Liver Injury: from Animal Models to Humans*. Journal of clinical and translational hepatology, (2014). 2(3): p. 153-61.
27. Ramachandran, A. and H. Jaeschke, *Acetaminophen Toxicity: Novel Insights Into Mechanisms and Future Perspectives*. Gene expression, (2018). 18(1): p. 19-30.
28. Kim, E., S. Wong, and J. Martinez, *Programmed Necrosis and Disease: We interrupt your regular programming to bring you necroinflammation*. Cell Death And Differentiation, (2019). 26(1): p. 25-40.
29. Zhang, Y., X. Chen, C. Gueydan, et al., *Plasma membrane changes during programmed cell deaths*. Cell Research, (2018). 28(1): p. 9-21.
30. Lewis, T., *Will Organs-in-a-Dish Ever Replace Animal Models?* The Scientist, (2016).
31. Carter, M. and J.C. Shieh, *Chapter 13 - Cell Culture Techniques*, in *Guide to Research Techniques in Neuroscience*, M. Carter and J.C. Shieh, Editors. (2010), Academic Press: New York, US. p. 281-296.
32. Saito, J., A. Okamura, K. Takeuchi, et al., *High content analysis assay for prediction of human hepatotoxicity in HepaRG and HepG2 cells*. Toxicology in Vitro, (2016). 33: p. 63-70.
33. Van Summeren, A., J. Renes, F.G. Bouwman, et al., *Proteomics Investigations of Drug-Induced Hepatotoxicity in HepG2 Cells*. Toxicological Sciences, (2011). 120(1): p. 109-122.
34. Xu, J., S. Oda, and T. Yokoi, *Cell-based assay using glutathione-depleted HepaRG and HepG2 human liver cells for predicting drug-induced liver injury*. Toxicology In Vitro, (2018). 48: p. 286-301.
35. Kuna, L., I. Bozic, T. Kizivat, et al., *Models of Drug Induced Liver Injury (DILI) - Current Issues and Future Perspectives*. Current drug metabolism, (2018). 19(10): p. 830-838.
36. Oesch, F., M. Lafranconi, and H.R. Glatt, *Role of parenchymal versus non-parenchymal cells in the control of biologically reactive intermediates*. Advances in Experimental Medicine and Biology, (1986). 197: p. 53-61.
37. Palma, E., E.J. Doornebal, and S. Chokshi, *Precision-cut liver slices: a versatile tool to advance liver research*. Hepatology International, (2019). 13(1): p. 51-57.

38. van Midwoud, P.M., J. Janssen, M.T. Merema, et al., *On-line HPLC Analysis System for Metabolism and Inhibition Studies in Precision-Cut Liver Slices*. Analytical Chemistry, (2011). 83(1): p. 84-91.
39. Cyranoski, D., *Race to mimic human embryonic stem cells*. Nature, (2007). 450(7169): p. n/a.
40. Lancaster, M.A. and J.A. Knoblich, *Organogenesis in a dish: modeling development and disease using organoid technologies*. Science, (2014). 345(6194): p. 1247125.
41. Prior, N., P. Inacio, and M. Huch, *Liver organoids: from basic research to therapeutic applications*. Gut, (2019). 68(12): p. 2228.
42. Biomarkers Definitions Working Group, *Biomarkers and surrogate endpoints: preferred definitions and conceptual framework*. Clinical Pharmacology & Therapeutics, (2001). 69(3): p. 89-95.
43. McGill, M., B. Woolbright, J. Weemhoff, et al., *Mechanistic Biomarkers in Liver Diseases*, in *Biomarkers in Liver Disease*, V.R.P. Vinood B. Patel, Editor. (2017), Springer: Dordrecht. p. 71-97.
44. McLntyre, N. and S. Rosalki, *22 - Tests of the Functions of the Liver*, in *Scientific Foundations of Biochemistry in Clinical Practice (Second Edition)*, D.L. Williams and V. Marks, Editors. (1994), Butterworth-Heinemann: Oxford, England. p. 383-398.
45. The Universal Protein Resource Knowledge Base. *P05186 (PPBT_HUMAN)*. [cited 2020/05/04]; Available from: <https://www.uniprot.org/uniprot/P05186>.
46. Engelmann, G., *Biomarkers in Focus: Alanine Aminotransferase*, in *Biomarkers in Liver Disease*, V.B. Patel and V.R. Preedy, Editors. (2017), Springer Netherlands: Dordrecht. p. 267-280.
47. Hasan, N., *Nitrogen metabolism and regulation of urea cycle*. (2018).
48. The Universal Protein Resource Knowledge Base. *UniProtKB - P02768 (ALBU_HUMAN)*. [cited 2020/02/12]; Available from: <https://www.uniprot.org/uniprot/P02768#sequences>.
49. Rafter, I., T. Graberg, A. Kotronen, et al., *Isoform-specific alanine aminotransferase measurement can distinguish hepatic from extrahepatic injury in humans*. International Journal of Molecular Medicine, (2012). 30(5): p. 1241-9.
50. Borrás, E. and E. Sabido, *What is targeted proteomics? A concise revision of targeted acquisition and targeted data analysis in mass spectrometry*. Proteomics, (2017). 17(17-18).
51. Gregorich, Z.R., Y.-H. Chang, and Y. Ge, *Proteomics in heart failure: top-down or bottom-up?* Pflugers Archiv : European journal of physiology, (2014). 466(6): p. 1199-1209.
52. McLafferty, F.W., K. Breuker, M. Jin, et al., *Top-down MS, a powerful complement to the high capabilities of proteolysis proteomics*. Febs journal, (2007). 274(24): p. 6256-68.
53. Steen, H. and M. Mann, *The ABC's (and XYZ's) of peptide sequencing*. Nature Reviews Molecular Cell Biology, (2004). 5(9): p. 699-711.
54. Wehr, T., *Top-down versus bottom-up approaches in proteomics*, in *LC GC N. AM*. (2006). p. 1004-+.
55. Kurien, B.T. and R.H. Scofield, *Introduction to Protein Blotting*, in *Protein Blotting and Detection: Methods and Protocols*, B.T. Kurien and R.H. Scofield, Editors. (2009), Humana Press: Totowa, NJ. p. 9-22.
56. Aebersold, R., A.L. Burlingame, R.A. Bradshaw, et al., *Western blots versus selected reaction monitoring assays: time to turn the tables?* Molecular & cellular proteomics, (2013). 12(9): p. 2381-2382.

57. Shehadul Islam, M., A. Aryasomayajula, and P.R. Selvaganapathy, *A Review on Macroscale and Microscale Cell Lysis Methods*. *Micromachines*, (2017). 8(3): p. 83.
58. Kopot, A. and A. Vovk. *SDS Polyacrylamide Gel Electrophoresis*. [cited 2020/03/16]; Available from: <https://aklectures.com/lecture/sds-polyacrylamide-gel-electrophoresis>.
59. Sun, S., J.Y. Zhou, W. Yang, et al., *Inhibition of protein carbamylation in urea solution using ammonium-containing buffers*. *Analytical Biochemistry*, (2014). 446: p. 76-81.
60. Bennion, B.J. and V. Daggett, *The molecular basis for the chemical denaturation of proteins by urea*. *Proceedings of the National Academy of Sciences*, (2003). 100(9): p. 5142-7.
61. Sevier, C.S. and C.A. Kaiser, *Formation and transfer of disulphide bonds in living cells*. *Nature Reviews Molecular Cell Biology*, (2002). 3(11): p. 836-847.
62. Cleland, W.W., *Dithiothreitol, a New Protective Reagent for SH Groups**. *Biochemistry*, (1964). 3(4): p. 480-482.
63. Muller, T. and D. Winter, *Systematic Evaluation of Protein Reduction and Alkylation Reveals Massive Unspecific Side Effects by Iodine-containing Reagents*. *Molecular & cellular proteomics*, (2017). 16(7): p. 1173-1187.
64. Jocelyn, P.C., *Chemical reduction of disulfides*, in *Methods in Enzymology*. (1987), Academic Press. p. 246-256.
65. Whitesides, G.M., J.E. Lilburn, and R.P. Szajewski, *Rates of thiol-disulfide interchange reactions between mono- and dithiols and Ellman's reagent*. *The Journal of Organic Chemistry*, (1977). 42(2): p. 332-338.
66. Zhang, Y., B.R. Fonslow, B. Shan, et al., *Protein Analysis by Shotgun/Bottom-up Proteomics*. *Chemical Reviews*, (2013). 113(4): p. 2343-2394.
67. Vandermarliere, E., M. Mueller, and L. Martens, *Getting intimate with trypsin, the leading protease in proteomics*. *Mass Spectrometry Reviews*, (2013). 32(6): p. 453-465.
68. Hedstrom, L., *Serine Protease Mechanism and Specificity*. *Chemical Reviews*, (2002). 102(12): p. 4501-4524.
69. Kopot, A. and A. Vovk. *Reaction Mechanism of Chymotrypsin*. [cited 2020/03/17]; Available from: <https://aklectures.com/lecture/enzyme-mechanisms/reaction-mechanism-of-chymotrypsin>.
70. Hustoft, H.K., H. Malerod, S.R. Wilson, et al., *A Critical Review of Trypsin Digestion for LC-MS Based Proteomics*, in *Integrative Proteomics*, H.-C. Leung, Editor. (2012), IntechOpen.
71. Lundanes, E., *9.3 Solid-Phase Extraction*, in *Chromatography : basic principles, sample preparations and related methods*, L. Reubsæet and T. Greibrokk, Editors. (2014), Wiley-VCH: Weinheim.
72. Gornall, A.G., C.J. Bardawill, and M.M. David, *Determination of serum proteins by means of the biuret reaction*. *The Journal of biological chemistry*, (1949). 177(2): p. 751-66.
73. Thermo Fisher Scientific Inc. *Pierce BCA Protein Assay Kit (Reducing Agent Compatible) - User Guide*. (2011).
74. Smith, P.K., R.I. Krohn, G.T. Hermanson, et al., *Measurement of protein using bicinchoninic acid*. *Analytical Biochemistry*, (1985). 150(1): p. 76-85.
75. Lundanes, E., *3.5 Stationary Phases and Their Properties in HPLC*, in *Chromatography : basic principles, sample preparations and related methods*, L. Reubsæet and T. Greibrokk, Editors. (2014), Wiley-VCH: Weinheim.
76. Carr, D., *A Guide to the Analysis and Purification of Proteins and Peptides by Reversed-Phase HPLC*. (2016): www.ace-hplc.com.

77. Liang, Y., L. Zhang, and Y. Zhang, *Recent advances in monolithic columns for protein and peptide separation by capillary liquid chromatography*. *Analytical and Bioanalytical Chemistry*, (2013). 405(7): p. 2095-106.
78. Wilson, S.R., T. Vehus, H.S. Berg, et al., *Nano-LC in proteomics: recent advances and approaches*. *Bioanalysis*, (2015). 7(14): p. 1799-1815.
79. Lundanes, E., *Chromatography : basic principles, sample preparations and related methods*, ed. L. Reubsæet and T. Greibrokk. (2014), Weinheim: Wiley-VCH.
80. Lundanes, E., 3.6.2.5 *Mass Analysis*, in *Chromatography : basic principles, sample preparations and related methods*, L. Reubsæet and T. Greibrokk, Editors. (2014), Wiley-VCH: Weinheim.
81. Gross, J.H., 4.4.2 *The Linear Quadrupole*, in *Mass Spectrometry : A Textbook*. (2017), Springer International Publishing : Imprint: Springer: Berlin, Germany.
82. Harris, D.C. and C.A. Lucy, *Chromatography - Mass Spectrometry Techniques*, in *Quantitative chemical analysis*. (2016), Freeman: New York.
83. Gross, J.H., 9.3.2 *Energy Transfer During Collisions*, in *Mass Spectrometry : A Textbook*. (2017), Springer International Publishing : Imprint: Springer: Berlin, Germany.
84. Harris, D.C., *Quantitative chemical analysis*, C.A. Lucy, Editor. (2016), Freeman: New York.
85. *Electrospray Ionization*, in *Encyclopedia of Cancer*, M. Schwab, Editor. (2011), Springer Berlin Heidelberg: Berlin, Heidelberg. p. 1216-1216.
86. Cole, R.B., *Chapter 1 - On the mechanism of Electrospray Mass Spectrometry*, in *Electrospray ionization mass spectrometry : fundamentals, instrumentation, and applications*. (1997), Wiley: New York.
87. Gross, J.H., 12 *Electrospray Ionization*, in *Mass Spectrometry : A Textbook*. (2017), Springer International Publishing : Imprint: Springer: Berlin, Germany.
88. Taylor, G., *Disintegration of Water Drops in an Electric Field*. *Proceedings of the Royal Society of London. Series A, Mathematical and Physical Sciences (1934-1990)*, (1964). 280(1382): p. 383-397.
89. Cole, R.B., *Electrospray Ionization Mass Spectrometry* *Electrospray ionization mass spectrometry : fundamentals, instrumentation, and applications*. (1997), New York: Wiley.
90. Gross, J.H., 12.4 *Ion Formation in ESI* in *Mass Spectrometry : A Textbook*. (2017), Springer International Publishing : Imprint: Springer: Berlin, Germany.
91. Gross, J.H., 12.3 *Nanoelectrospray* in *Mass Spectrometry : A Textbook*. (2017), Springer International Publishing : Imprint: Springer: Berlin, Germany.
92. Thermo Fisher Scientific Inc., *Chapter 1 Introduction*, in *Nanospray Flex Series Ion Source*. (2017), Thermo Fisher Scientific Inc.,.
93. Kuzyk, M.A., C.E. Parker, D. Domanski, et al., *Development of MRM-based assays for the absolute quantitation of plasma proteins*. *Methods in Molecular Biology*, (2013). 1023: p. 53-82.
94. Fu, Q., E. Grote, J. Zhu, et al., *An Empirical Approach to Signature Peptide Choice for Selected Reaction Monitoring: Quantification of Uromodulin in Urine*. *Clinical Chemistry*, (2016). 62(1): p. 198.
95. James, A. and C. Jorgensen, *Basic Design of MRM Assays for Peptide Quantification*, in *LC-MS/MS in Proteomics: Methods and Applications*, P.R. Cutillas and J.F. Timms, Editors. (2010), Humana Press: Totowa, NJ. p. 167-185.
96. Promega Corporation, *ProteaseMAX™ Surfactant, Trypsin Enhancer*. (2015). p. 12.
97. Thermo Fisher Scientific Inc., *Mini Gel Tank - User Guide*. (2014).
98. Thermo Fisher Scientific Inc., *Imperial Protein Stain - User Guide*. (2014).

99. Shevchenko, A., H. Tomas, J. Havli, et al., *In-gel digestion for mass spectrometric characterization of proteins and proteomes*. Nature Protocols, (2007). 1: p. 2856.
100. Berg, H.S., K.E. Seterdal, T. Smetop, et al., *Self-packed core shell nano liquid chromatography columns and silica-based monolithic trap columns for targeted proteomics*. Journal of Chromatography A, (2017). 1498: p. 111-119.
101. MB Centre for Proteomics and Systems Biology. *Sequence Specific Retention Calculator*. (2007) [cited 2020/02/12]; Version 3.2:[Available from: <http://hs2.proteome.ca/SSRCalc/SSRCalcXHHelp.htm>].
102. Overton, T.W., *Recombinant protein production in bacterial hosts*. Drug Discovery Today, (2014). 19(5): p. 590-601.
103. Lundanes, E., *1.3.1 Eddy diffusion*, in *Chromatography : basic principles, sample preparations and related methods*, L. Reubsæet and T. Greibrokk, Editors. (2014), Wiley-VCH: Weinheim.
104. Gamal, W., P. Treskes, K. Samuel, et al., *Low-dose acetaminophen induces early disruption of cell-cell tight junctions in human hepatic cells and mouse liver*. Scientific reports, (2017). 7(1): p. 37541-37541.
105. Mazaleuskaya, L.L., K. Sangkuhl, C.F. Thorn, et al., *PharmGKB summary: pathways of acetaminophen metabolism at the therapeutic versus toxic doses*. Pharmacogenetics and genomics, (2015). 25(8): p. 416-426.
106. Skolnik, A.B. and S.R. Wilcox, *Chapter 79 - Analgesics and Antidepressants*, in *Critical Care Secrets (Fifth Edition)*, P.E. Parsons and J.P. Wiener-Kronish, Editors. (2013), Mosby: Philadelphia. p. 552-557.
107. U.S Food and Drug Administration. *M3(R2) Nonclinical Safety Studies for the Conduct of Human Clinical Trials and Marketing Authorization for Pharmaceuticals*. (2010) [cited 2020/05/26]; Available from: <https://www.fda.gov/media/71542/download>.
108. Krokhin, O.V., *Sequence-specific retention calculator. Algorithm for peptide retention prediction in ion-pair RP-HPLC: application to 300- and 100-Å pore size C18 sorbents*. Analytical Chemistry, (2006). 78(22): p. 7785-95.
109. Biology, M.C.f.P.a.S. *Sequence Specific Retention Calculator*. (2003) [cited 2020/04/28]; Version 3.1:[Available from: <http://hs2.proteome.ca/SSRCalc/SSRCalcHelp.htm#REFS>].

7 Appendix

7.1 Supplementary theory

This section includes supplementary theory to support concepts introduced in section 2.

7.1.1 Molecular structure of amino acid

Figure 49 shows the structure of all 21 amino acids including their full name, abbreviation and single-letter notation, categorized by chemical property.

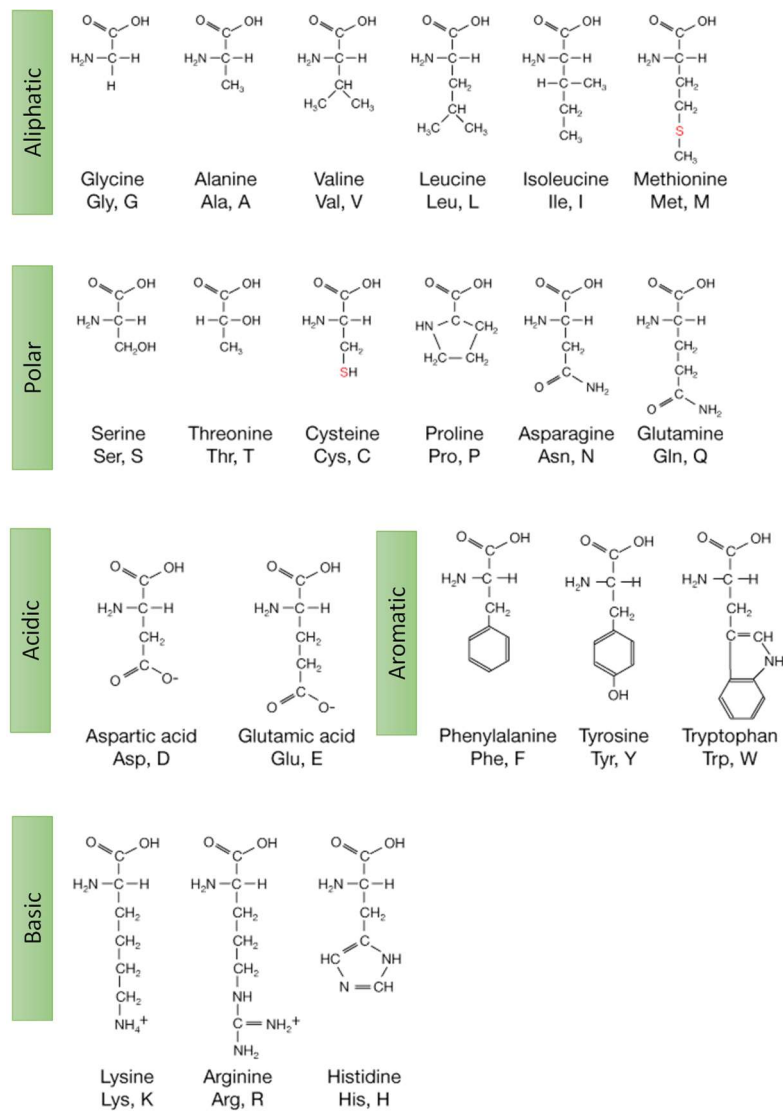


Figure 49: Chart of amino acids with full name, abbreviation and single-letter notation, categorized by their chemical property.

7.1.2 Protein structure

Proteins are built from amino acids linked together by amide bonds as illustrated in **Figure 50**.

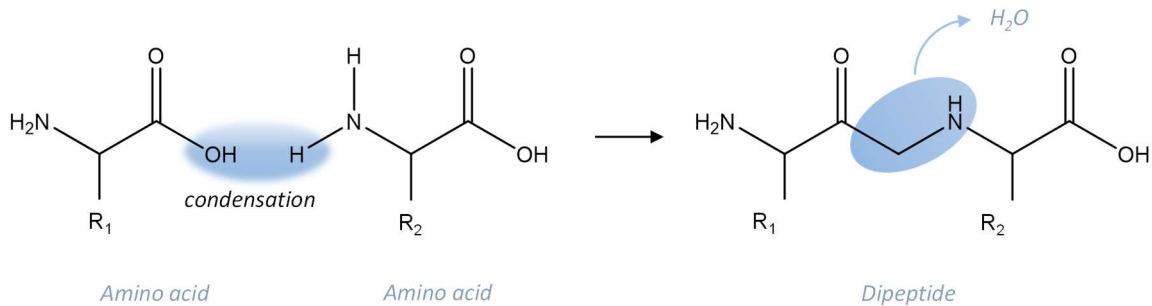


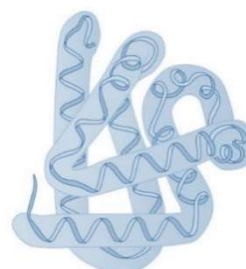
Figure 50: The formation of an amide bond between two amino acids from a condensation reaction to form a dipeptide

Proteins are characterized by different levels of structures as summarized on **Table 14**.

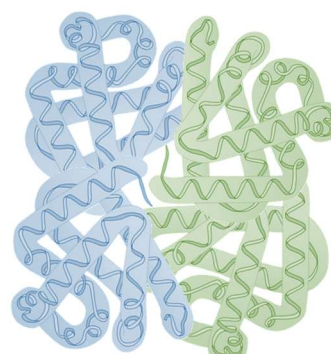
Table 14: Summary of protein structures.

Structure	Description	Illustration
Primary	The amino acid sequence linked together with amide bonds and sulfide bridges formed between cysteine residues in the peptide sequence.	
Secondary	Alpha helixes formed from hydrogen bonding in the peptide backbone. Beta sheets formed from hydrogen bonding between parallel or anti-parallel peptide ribbons.	<div style="display: flex; justify-content: space-around; align-items: center;"> <div style="text-align: center;"> <i>alpha-helix</i> </div> <div style="text-align: center;"> <i>beta-sheets</i> </div> </div>

Tertiary The structure describes protein describes how alpha-helices, beta-sheets and non-structured regions interact to form a completely folded protein.



Quaternary Individual proteins, and perhaps metal atoms and/or non-protein molecules (ligands) forming a complex.



7.1.3 Plots

Figure 51 contains boxplot descriptives. **Figure 52** shows a visual representation of the prediction interval for a calibration curve.

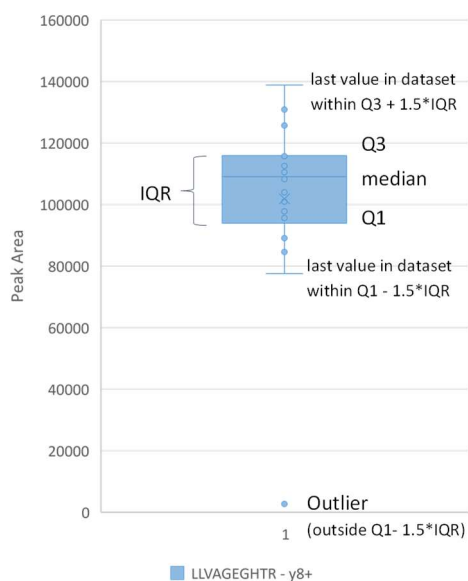


Figure 51: Descriptive figure of boxplot.

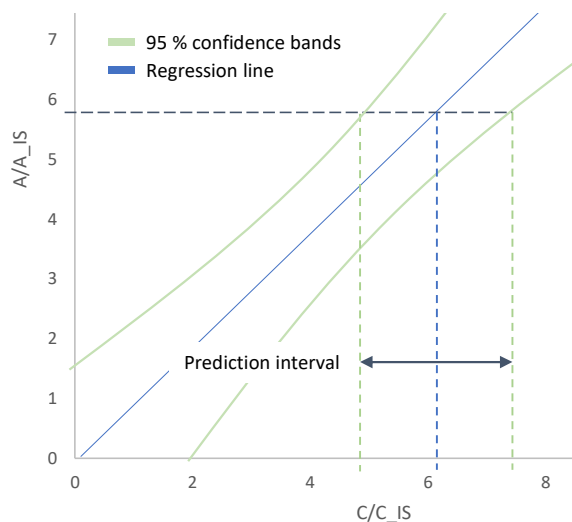


Figure 52: Visual representation of prediction interval for a calibration curve defined by linear regression.

7.1.4 SSRCalculator

The sequence specific retention (SSR) calculator version 3.0 is a model correlating hydrophobicity and retention time and was developed by Manitoba Centre for Proteomics and Systems Biology [108, 109].

The model was developed based on the empirical measurement of retention times of more than 2000 tryptic peptides in the 560-5000 Da mass range, derived from mixtures of a number of protein digests. The model relies on summation of the retention coefficients of the individual amino acids relating to the amino acids at the N-terminal and C-terminal of the peptide, peptide length, total peptide hydrophobicity, uniformity of distribution of the relatively hydrophobic amino acids along the peptide chain, the isoelectric point and the effect of missed cleavages [108, 109].

The resulting dependence of retention time (RT) vs. the hydrophobicity (HP) of the peptides is a linear function given by the formula:

$$RT = A + B * (HP), \quad (\text{Equation 2})$$

where the intercept A denotes the gradient delay time and the slope B is related to the slope of the gradient.

The SSRC calculator is applicable for water-ACN gradients on a reversed-phase C18 silica column with a pore size of 300 Å and 100 Å. Proteins or protein mixtures should be reduced, alkylated with iodoacetamide and digested with trypsin [108, 109].

7.2 Websites and downloads

Websites



Skyline



Uniprot



BLAST



PeptideAtlas

Spectral libraries



Iontrap



Orbitrap HCD

7.3 Dilutions of peptide and protein standards

Table 15: Serial dilution of standards for calibration curve from BSA stock solution for BCA assay.

Vial	ABC buffer (μL)	BSA source (μL)	Conc. ($\mu\text{g/mL}$)
A	0	60 of stock	2000
B	15	45 of stock	1500
C	24	24 of stock	1000
D	24	24 of vial B	750
E	24	24 of vial C	500
F	24	24 of vial E	250
G	24	24 of vial F	125

Table 16: Serial dilution of samples from protein stock solution for BCA assay.

Vial	ABC buffer (μL)	Protein source (μL)	Dilution factor
S1	0	35 of stock	1
S2	31.5	3.5 of S1	10
S3	32.5	2.5 of S2	100

Table 17: Dilution of stock solution for LLVAGEGHTR to a final volume of 1000 μL .

Cons (μM) → ↓	ID	V stock (μL)			V solvent (μL)
		950	100	10	
100				0.1	894
10		106	100		900
0.1	X			10	990
0.01	Y			1	999

Table 18: Dilution of stock solution for LLVA*GEGHTR to a final volume of 1000 μL .

Cons (μM) → ↓	ID	V stock (μL)			V solvent (μL)
		946	100	10	
100				0.1	895
10		105	100		900
0.1				10	990
0.01	Z			1	999

Table 19: Standard (calibration) solutions with (AC-FC) and without (A-F) cell medium to a final volume of 1000 μL . Three replicates of each standard solution were prepared.

Standard solution	cons. (fmol/ μL)		V_stock (μL)			V_solvent (μL)	
	LLVAGE...	LLVA*G...	X	Y	Z	0.1 % FA in water	1.25 $\mu\text{g}/\mu\text{L}$ cell medium
A	0.1	1.0	10		100	890	
B	0.5	1.0	50		100	850	
C	1.0	1.0	100		100	800	
D	2.0	1.0		20	100	880	
E	5.0	1.0		50	100	850	
F	10.0	1.0		100	100	800	
AC	0.1	1.0	10		100	790	100
BC	0.5	1.0	50		100	750	100
CC	1.0	1.0	100		100	700	100
DC	2.0	1.0		20	100	780	100
EC	5.0	1.0		50	100	750	100
FC	10.0	1.0		100	100	700	100

Table 20: Preparation of cell medium and organoid samples with APAP and NAPQI. Three replicates were prepared.

#sample	0.2 M APAP (μL)	20 mM NAPQI (μL)	medium (μL)	organoids (μL)	APAP cons. (mM)	NAPQI cons. (mM)
B1.1-B1.3				100	0	0
B2.1-B2.3			100		0	0
P1.1-P1.3	25		75		50	0
P2.1-P2.3	17.5		82.5		35	0
P3.1-P3.3	10		90		20	0
P4.1-P4.3	25			75	50	0
P5.1-P5.3	17.5			82.5	35	0
P6.1-P6.3	10			90	20	0
R1.1-R1.3		25	75		0	5
R2.1-R2.3		17.5	82.5		0	3.5
R3.1-R3.3		10	90		0	2.0
R4.1-R4.3		25		75	0	5
R5.1-R5.3		17.5		82.5	0	3.5
R6.1-R6.3		10		90	0	2.0

7.4 Raw data and calculations

Figure 53 contains the BLAST analysis output for ALT1 and ALT2.

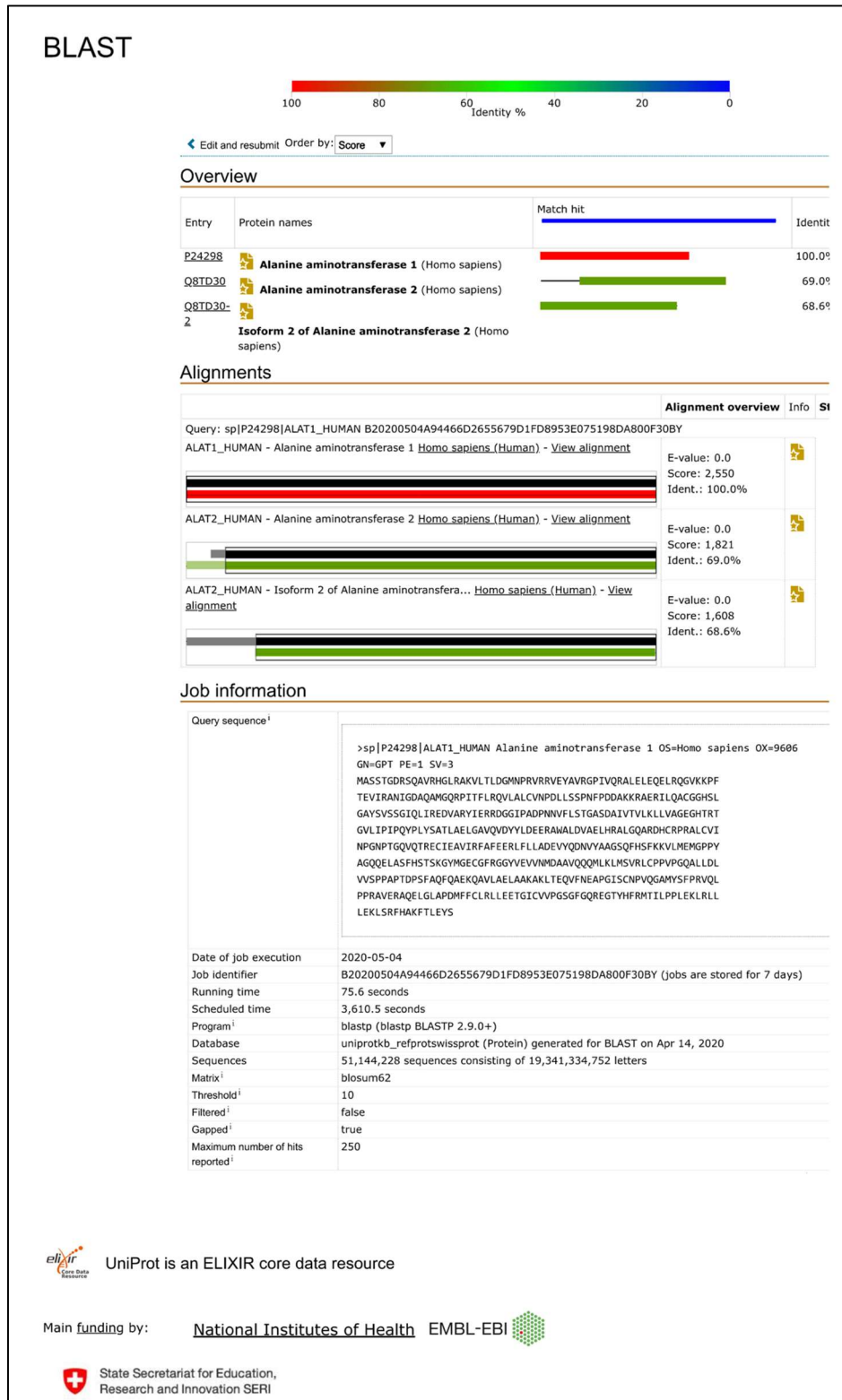


Figure 53: BLAST analysis output file for ALT1 and ALT2

Figure 54 contains an illustration for the number of sequence combinations that can be achieved from a 9 a.a. long peptide, with and without fragmentation.

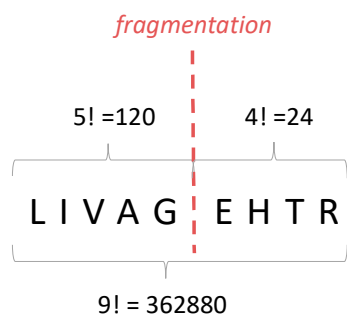


Figure 54: The number of sequence combinations for a 9 a.a. (unique) long peptide equals $9! = 362880$. Introducing the monitorization of a single peptide results in $5! * 4! = 120 * 24 = 2880$ sequence combinations. The reduction in sequence combinations is equal to $(362880 - 2880) / 362880 * 100\% = 99.2\%$.

7.4.1 BCA-assay with NanoDrop measurements

Table 21 and **Table 22** contain raw data for the determination of the total protein concentration in ALT1 standard.

Table 21: Absorbance at 563 nm for BSA standards for n=2, one measurement per standard.

Measure	BSA cons. µg/mL	Avg Abs.	#1	#2
Sample Blank	0	0.019	0.021	0.017
Standard G	125	0.002	0.003	0.001
Standard F	250	0.01	0.011	0.009
Standard E	500	0.027	0.027	0.028
Standard D	750	0.043	0.042	0.044
Standard C	1000	0.057	0.049	0.065
Standard B	1500	0.089	0.09	0.088
Standard A	2000	0.112	0.113	0.11

Table 22: Total protein concentration of ALT1 standard, n=2, two measurements per sample calculated from standard calibration curve. Automatically calculated in Nanodrop software.

Measure	Avg meas cons.	#1	#2
S3.1	66.726	69.146	64.306
S3.2	88.0575	92.435	83.68
Measure	Avg replicate Cons.	Std Dev.	Rel Std Dev. (%)
S3	77	15	19

S2 and up	out of range		
-----------	--------------	--	--

Table 23 and **Table 24** contain raw data for the determination of the total protein concentration in cell medium.

Table 23: Absorbance at 563 nm for BSA standards for n=2, one measurement per standard.

Measure	BSA cons. µg/mL	Avg Abs.
Standard F	125	0.013
Standard E	250	0.025
Standard D	500	0.04
Standard C	750	0.055
Standard B	1000	0.076
Standard A	1500	0.088

Table 24: Absorbance at 563 nm for cell medium, n=2, one measurement per sample. Protein concentration manually calculated below due to issues with calibration curve display in Nanodrop Software.

Measure	Avg abs	#1	#2
S1	0.08725	0.0825	0.092

Calculation of total protein concentration in cell medium

Linear regression equation: $a = 6.00E-05$, $b = 0.0111$

Average measured cons. (S1): $1.27E+03$ µg/mL

Final cons. (accounted for dilution): 1269 µg/mL

Table 25 and **Table 26** contain raw data for the determination of the total protein concentration in hepatic organoids.

Table 25: Absorbance at 563 nm for BSA standards for n=2, one measurement per standard.

Measure	V stock (µL)	m BSA (µg)	Avg Abs.
Standard F	1	2	0.028

Standard E	2	4	0.076
Standard D	4	8	0.136
Standard C	6	12	0.166
Standard B	9	18	0.275
Standard A	10	20	0.317

Table 26: Absorbance at 563 nm for lysed hepatic organoids, n=2, one measurement per sample. Protein concentration manually calculated below due to issues with calibration curve display in Nanodrop Software.

Measure	Avg abs	#1	#2
Sample	0.055	0.056	0.055

Calculation of the total protein concentration in hepatic organoids

Linear regression equation: $a = 0.0152$, $b = 0.0046$

Sample: 3.332 μg protein

V sample: 5 μL

cons 666.4 $\mu\text{g/mL}$

7.4.2 Gel electrophoresis

Figure 55 shows the gel slap for two lanes of hepatic organoids (L1 and L2) and a standard protein ladder. The reference could not be used as an overload of the wells for the hepatic organoids morphed the lane for the protein ladder. The excision of slabs for ALT1 were based on the bold band for the sample lanes, which was assumed to be from HSA (66.5 kDa), being the most abundant protein in organoids. The excised bands from both lanes were pooled to increase analyte abundance in the analysed sample.



Figure 55: Gel electrophoresis - gel slab of two lanes of 60 μ L lysed hepatic organoids in each well (L1, L2) compared to protein ladder reference. The reference could not be used as an overload of the wells for the hepatic organoids morphed the lane for the protein ladder. The excision of slabs for ALT1 were based on the bold band for the sample lanes, which was assumed to be from HSA (66.5 kDa), being the most abundant protein in organoids. The excised bands from both lanes were pooled to increase analyte abundance in the analyzed sample.

7.4.3 Chromatographic data

Table 27 contains chromatographic data for 100 pg on-column HSA standard, recorded with SRC#1.

Table 28 contains chromatographic data for undiluted ALT standard, recorded with SRC#2.

Table 29 contains chromatographic data for 500 ng ALT standard on-column, recorded with SRC#3.

Table 30 contains chromatographic data for 1.0 fmol LLVAGEGHTR standard on-column, recorded with SRC#4.

Table 31 contains chromatographic data for LLVAGEGHTR from ~ 60 organoids, excised from gel ~60 kDa, reconstituted in 500 μ L H₂O in 0.1 % FA and diluted 100X, and recorded with SRC#4.

Table 27: Recorded 2019-09-SEP-20, SRC#1, 100 pg on-column HSA standard

Peptide	Precursor Mz	Precursor Charge	Product Mz	Product Charge	Fragment Ion	Collision Energy	Retention Time	Area	Total Area	Fwhm
DLGEENFK	476.22	2	229.12	1	b2	18.5	7.49	96714	423111	0.17
DLGEENFK	476.22	2	723.33	1	y6	18.5	7.51	275024	423111	0.18
DLGEENFK	476.22	2	666.31	1	y5	18.5	7.52	15510	423111	0.15
DLGEENFK	476.22	2	537.27	1	y4	18.5	7.49	35864	423111	0.17
LVNEVTEFAK	575.31	2	213.16	1	b2	21.9	10.98	350885	1231495	0.2
LVNEVTEFAK	575.31	2	555.31	1	b5	21.9	10.98	20677	1231495	0.28
LVNEVTEFAK	575.31	2	937.46	1	y8	21.9	10.99	496063	1231495	0.2
LVNEVTEFAK	575.31	2	694.38	1	y6	21.9	10.99	159433	1231495	0.19
LVNEVTEFAK	575.31	2	595.31	1	y5	21.9	10.99	204438	1231495	0.2
DDNPNLPR	470.73	2	345.10	1	b3	18.3	5.14	76188	1449644	0.16
DDNPNLPR	470.73	2	669.28	1	b6	18.3	5.14	33269	1449644	0.14
DDNPNLPR	470.73	2	596.35	1	y5	18.3	5.14	849197	1449644	0.16
DDNPNLPR	470.73	2	272.17	1	y2	18.3	5.16	368651	1449644	0.16
DDNPNLPR	470.73	2	355.70	2	y6	18.3	5.16	122338	1449644	0.17
YLYEIAR	464.25	2	277.15	1	b2	18.1	10.07	313665	1911149	0.21
YLYEIAR	464.25	2	440.22	1	b3	18.1	10.14	15707	1911149	0.23

YLYEIAR	464.25	2	651.35	1	y5	18.1	10.07	1212450	1911149	0.2
YLYEIAR	464.25	2	488.28	1	y4	18.1	10.07	222426	1911149	0.2
YLYEIAR	464.25	2	359.24	1	y3	18.1	10.07	146901	1911149	0.22
AEFAEVSK	440.72	2	201.09	1	b2	17.3	5.3	1093722	3201070	0.13
AEFAEVSK	440.72	2	348.16	1	b3	17.3	5.3	162342	3201070	0.13
AEFAEVSK	440.72	2	680.36	1	y6	17.3	5.3	1468743	3201070	0.14
AEFAEVSK	440.72	2	533.29	1	y5	17.3	5.3	349975	3201070	0.13
AEFAEVSK	440.72	2	462.26	1	y4	17.3	5.3	126288	3201070	0.13
LVTDLTK	395.24	2	213.16	1	b2	15.8	6.04	879951	4229273	0.23
LVTDLTK	395.24	2	676.39	1	y6	15.8	6.05	366901	4229273	0.25
LVTDLTK	395.24	2	577.32	1	y5	15.8	6.04	2888784	4229273	0.23
LVTDLTK	395.24	2	476.27	1	y4	15.8	6.02	93636	4229273	0.25
FQNALLVR	480.78	2	276.13	1	b2	18.7	10.36	509868	2403697	0.21
FQNALLVR	480.78	2	685.44	1	y6	18.7	10.36	1218612	2403697	0.21
FQNALLVR	480.78	2	571.39	1	y5	18.7	10.36	235721	2403697	0.22
FQNALLVR	480.78	2	500.36	1	y4	18.7	10.37	245292	2403697	0.22
FQNALLVR	480.78	2	387.27	1	y3	18.7	10.36	194204	2403697	0.21
LVAASQAALGL	507.30	2	570.32	1	b6	19.6	15.46	5049	151226	0.21
LVAASQAALGL	507.30	2	712.40	1	b8	19.6	15.39	21469	151226	0.15
LVAASQAALGL	507.30	2	825.48	1	b9	19.6	15.39	9998	151226	0.22
LVAASQAALGL	507.30	2	882.50	1	b10	19.6	15.43	6509	151226	0.13
LVAASQAALGL	507.30	2	189.12	1	y2	19.6	15.38	108200	151226	0.19

Table 28: Recorded 2019-11-NOV-19, SRC#2, undiluted ALT standard.

Peptide	Precursor Mz	Precursor Charge	Product Mz	Product Charge	Fragment Ion	Collision Energy	Retention Time	Area	Total Area	Fwhm
ALELEQELR	550.8	2	916.5	1	y7	25.2	14.5	88260	3098013	0.31
ALELEQELR	550.8	2	787.4	1	y6	25.2	14.4	1575674	3098013	0.31
ALELEQELR	550.8	2	674.3	1	y5	25.2	14.4	1010597	3098013	0.31
ALELEQELR	550.8	2	288.2	1	y2	25.2	14.3	201676	3098013	0.31
ALELEQELR	550.8	2	926.5	1	b8	25.2	14.4	221806	3098013	0.31
LLVAGEGHTR	526.8	2	826.4	1	y8	24.4	15.5	1200210	16998972	1.49
LLVAGEGHTR	526.8	2	727.3	1	y7	24.4	15.4	1160293	16998972	1.53
LLVAGEGHTR	526.8	2	656.3	1	y6	24.4	16.9	1716557	16998972	1.11
LLVAGEGHTR	526.8	2	470.2	1	y4	24.4	16.6	10767897	16998972	1.09
LLVAGEGHTR	526.8	2	413.2	1	y3	24.4	15.4	2154015	16998972	1.56
FAFEER	399.7	2	651.3	1	y5	20.2	10.0	30392	168590	0.19
FAFEER	399.7	2	580.3	1	y4	20.2	10.0	58154	168590	0.18
FAFEER	399.7	2	433.2	1	y3	20.2	9.7	35230	168590	0.18
FAFEER	399.7	2	219.1	1	b2	20.2	10.0	31288	168590	0.20
FAFEER	399.7	2	366.2	1	b3	20.2	9.8	13527	168590	0.22

Table 29: Recorded 2020-02-FEB-15, SRC#3, 500 ng ALT standard on-column. Data in red cells has been retrieved from peaks with poor shape or low signal intensity.

Peptide	Precursor Mz	Precursor Charge	Product Mz	Product Charge	Fragment Ion	Collision Energy	Retention Time	Area	Total Area	Fwhm
ALELEQELR	550.8	2	916.5	1	y7	25.2	33.6	1238	42592	0.05
ALELEQELR	550.8	2	787.4	1	y6	25.2	33.7	15350	42592	0.08
ALELEQELR	550.8	2	674.3	1	y5	25.2	33.7	11259	42592	0.07
ALELEQELR	550.8	2	185.1	1	b2	25.2	33.7	14499	42592	0.06
ALELEQELR	550.8	2	157.6	2	b3	25.2	33.7	245	42592	0.05
LLVAGEGHTR	526.8	2	826.4	1	y8	24.4	17.4	1361628	2772505	0.27
LLVAGEGHTR	526.8	2	727.3	1	y7	24.4	20.0	6631	2772505	0.04
LLVAGEGHTR	526.8	2	656.3	1	y6	24.4	19.0	10989	2772505	1.65
LLVAGEGHTR	526.8	2	227.2	1	b2	24.4	17.4	1242839	2772505	0.21
LLVAGEGHTR	526.8	2	199.1	2	b4	24.4	17.4	150418	2772505	0.34
FAFEER	399.7	2	651.3	1	y5	20.2	5.9	3000	580282	0.09
FAFEER	399.7	2	580.3	1	y4	20.2	5.9	3816	580282	0.51
FAFEER	399.7	2	304.2	1	y2	20.2	5.9	39965	580282	0.08
FAFEER	399.7	2	175.1	1	y1	20.2	5.9	469811	580282	0.1
FAFEER	399.7	2	219.1	1	b2	20.2	5.9	63691	580282	0.09

Table 30: Recorded 2020-03-MAR-12, SRC#4, 1.0 fmol LLVAGEGHTR standard on-column.

Replicate	Precursor Mz	Precursor Charge	Product Mz	Product Charge	Fragment Ion	Collision Energy	Retention Time	Area	Background	Total Area	Fwhm
rep1	526.8	2	826.4	1	y8	24.4	11.2	61824	0	246515	0.15
rep2	526.8	2	826.4	1	y8	24.4	11.2	54288	0	219523	0.24
rep3	526.8	2	826.4	1	y8	24.4	11.3	52567	0	210637	0.16
rep1	526.8	2	727.3	1	y7	24.4	11.3	57020	0	246515	0.11
rep2	526.8	2	727.3	1	y7	24.4	11.2	49399	0	219523	0.12
rep3	526.8	2	727.3	1	y7	24.4	11.2	47599	0	210637	0.21
rep1	526.8	2	656.3	1	y6	24.4	11.3	34916	0	246515	0.18
rep2	526.8	2	656.3	1	y6	24.4	11.2	30077	0	219523	0.1
rep3	526.8	2	656.3	1	y6	24.4	11.2	30192	0	210637	0.13
rep1	526.8	2	470.2	1	y4	24.4	11.3	14577	451	246515	0.2
rep2	526.8	2	470.2	1	y4	24.4	11.2	12664	0	219523	0.08
rep3	526.8	2	470.2	1	y4	24.4	11.2	12444	0	210637	0.2
rep1	526.8	2	470.3	2	y9	24.4	11.3	14577	451	246515	0.2
rep2	526.8	2	470.3	2	y9	24.4	11.2	12664	0	219523	0.08
rep3	526.8	2	470.3	2	y9	24.4	11.2	12444	0	210637	0.2
rep1	526.8	2	413.7	2	y8	24.4	11.3	39319	203	246515	0.2
rep2	526.8	2	413.7	2	y8	24.4	11.2	36927	0	219523	0.25
rep3	526.8	2	413.7	2	y8	24.4	11.2	35717	70	210637	0.18
rep1	526.8	2	199.1	2	b4	24.4	11.3	24283	87	246515	0.17
rep2	526.8	2	199.1	2	b4	24.4	11.3	23503	0	219523	0.24
rep3	526.8	2	199.1	2	b4	24.4	11.2	19675	0	210637	0.17

Table 31: Recorded 2020-03-MAR-12, SRC#4 (n=1, ~ 60 organoids, excised from gel ~60 kDa, reconstituted in 500 µL H₂O in 0.1 % FA and diluted 100X). Data in red cells has been retrieved from peaks with poor shape or low signal intensity.

Peptide	Replicate	Product Mz	Fragment Ion	Collision Energy	Retention Time	Area	Background	Total Area	Fwhm
LLVAGEGHTR	blank	826.4	y8	24.4	11.93	15	0	111	0.03
LLVAGEGHTR	blank	727.3	y7	24.4	12	96	0	111	0.11
LLVAGEGHTR	P72L5	826.4	y8	24.4	11.78	355	0	363	0.03
LLVAGEGHTR	P72L5	727.3	y7	24.4	11.35	8	0	363	0.03

7.4.4 Regression analysis

Table 32 contains data points for the regression analysis of HSA measured retention times.

Table 32: Raw data for retention time regression analysis in Figure 37.

Peptide	Retention time
DLGEENFK	13,86
LVNEVTEFAK	20,95
DDNPNLPR	8,79
YLYEIAR	19,11
AEFAEVSK	9,25
LVTDLTK	10,98
FQNALLVR	19,66
LVAASQAALGL	27,35

7.4.5 Chart data

Table 33 contains raw data for the dotp value boxplot in **Figure 32**.

Table 34 and **Table 34** contain raw data for the graphical illustrations in **Figure 34**.

Table 36 contains raw data for the fragment y8⁺ peak area for boxplot in **Figure 45**.

Table 37 and **Table 38** contain raw data for graphical illustrations in **Figure 46**.

Table 33: Rawdata for dotp values in boxplot in **Figure 32**.

Peptide	rep1	rep2	rep3	mean
YLYEIAR	0.9113	0.9432	0.9138	0.922767
LVTDLTK	0.8706	0.9059	0.8715	0.882667
LVNEVTEFAK	0.8464	0.8518	0.8482	0.8488
LVAASQAALGL	0.6867	0.7286	0.7096	0.7083
FQNALLVR	0.935	0.9491	0.9348	0.939633
DLGEENFK	0.94	0.9148	0.9365	0.930433
DDNPNLPR	0.7513	0.7877	0.754	0.764333
AEFAEVSK	0.9095	0.9059	0.9103	0.908567

Table 34: Fragment peak area of 9 HSA tryptic peptides (100 pg HSA standard on-column) for graphical illustrations in **Figure 34**.

Peptide	Gradient steepness Δ[%B/min]				
	0.25	0.35	0.45	0.52	0.61
Fragments					
AEFAEVSK					
b2+	840015	818617	813569	898432	822555
b3+	140550	133608	122303	134698	126268
y4+	102677	97913	98487	102786	104692
y5+	278503	278919	268075	299435	282296
y6+	1120412	1180591	1112322	1281742	1155889
DDNPNLPR					
b3+	53784	53842	53911	67038	57605
b6+	23269	27087	23482	29409	24545
y2+	312018	287463	274266	307051	259784
y5+	689375	644003	586009	684810	644361
y6++	100250	99743	86441	97187	91927
DLGEENFK					
b2+	69925	79714	71287	78526	81506
y4+	23256	24534	25466	30528	25485
y5+	13682	16779	11300	17242	13314
y6+	210000	237888	210317	238824	232667
FQNALLVR					
b2+	463028	377140	345906	300752	338081
y3+	189861	153800	140977	111112	130644
y4+	211048	197437	183731	140070	164487
y5+	205109	185229	172557	128085	157648
y6+	1056431	918682	863165	660809	779004

LVAASQAALGL					
b10+	6820	7851	7745	4790	6186
b6+	5419	4427	7603	4787	5497
b8+	21514	21087	19376	20852	18434
b9+	12014	11654	10112	11069	10901
y2+	106366	116197	117964	122624	108989
LVNEVTEFAK					
b2+	374268	268141	303218	215308	256205
b5+	16266	13625	15181	15302	13309
y5+	220754	154548	178446	122189	148938
y6+	176482	136144	145909	107985	127371
y8+	509950	393376	432448	327222	377729
LVTDLTK					
b2+	666891	675969	616019	731335	676248
y4+	77445	69430	71422	81705	67270
y5+	2280199	2253141	2023224	2440519	2169755
y6+	280480	277696	263777	313434	279739
TYETTLEK					
b2+	415606	420788	408458	460176	440007
b3+	34798	40994	39469	36925	46516
y5+	277705	289315	267029	299302	290969
y6+	1014026	1097771	996484	1168965	1099349
YLYEIAR					
b2+	255486	244643	199500	225746	194335
b3+	9905	11553	9846	11958	13971
y3+	134815	117559	109390	102670	96850
y4+	176913	170876	151957	158845	143233
y5+	998967	931860	850526	866105	711598

Table 35: FWHM of 9 HSA tryptic peptides (100 pg HSA standard on-column) for graphical illustrations in Figure 34.

Peptides	$\Delta(\%B/min)$			
	0.61	0.52	0.35	0.25
AEFAEVSK	0.14	0.15	0.2	0.29
DDNPNLPR	0.17	0.15	0.22	0.23
DLGEENFK	0.16	0.17	0.21	0.29
FQNALLVR	0.33	0.28	0.39	0.53
LVAASQAALGL	0.22	0.17	0.19	0.34
LVNEVTEFAK	0.27	0.26	0.35	0.39
LVTDLTK	0.22	0.22	0.26	0.25

TYETTLEK	0.15	0.16	0.22	0.37
YLYEIAR	0.27	0.3	0.37	0.5

Table 36: Raw data for fragment y8+ peak area for boxplot in **Figure 45**. The outlier is marked in red.

arbitrary	peak area	Q1	93981
1	104000	median	109062.5
1	97796	Q3	115901
1	112511	IQR	21920
1	109855		
1	125670		
1	110481		
1	108270		
1	112026		
1	115713		
1	130889		
1	100928		
1	138851		
1	116465		
1	89091		
1	95611		
1	77513		
1	2694		
1	84585		

Table 37: Raw data for regression residual plot in **Figure 46**

c	y8+	y7+
0.1	0.043959	0.095526
0.5	0.107447	0.13273
1	0.038098	0.093576
2	0.105428	0.165594

Table 38: Raw data for calibration curves and boxplot for std. dev. for y8+ and y7+ in **Figure 46**.

fragment	std/rep	cons	#1	#2	#3	n	ratio	std	rel. std
y8+	A	0.1	0.0964	0.0917	0.1021	3	0.097	0.004	0.04
y8+	B	0.5	0.5655	0.4384	0.4782	3	0.49	0.05	0.1
y8+	C	1	1.0332	1.1334	1.0738	3	1.08	0.04	0.04
y8+	D	2	1.7084	2.1858	1.8388	3	1.9	0.2	0.1
y8+	E	5	4.239	3.3566	4.3995	3	4.0	0.5	0.1

y8+	F	10	10.9937	11.4202	6.9858	3	10	2	0.2
y7+	A	0.1	0.0903	0.0732	0.0904	3	0.085	0.008	0.1
y7+	B	0.5	0.5217	0.404	0.3927	3	0.44	0.06	0.1
y7+	C	1	0.8916	1.1129	1.0706	3	1.03	0.10	0.09
y7+	D	2	1.5752	1.8637	2.3495	3	1.9	0.3	0.2
y7+	E	5	4.6369	3.1935	4.0475	3	4.0	0.6	0.1
y7+	F	10	13.6043	8.631	8.5184	3	10	2	0.2

7.4.6 Statistics

Normality assessment – skewness

Table 39 contains raw data for normality assessment by skewness. If the skewness is not significant, a normal distribution is assumed.

Table 39: Raw data for normality assessment by skewness of data used in statistical testing.

	skew	N	Standard error of skewness	t skew	t crit	Significance (t_skew ≥ t_crit)
Excel function	=SKEW(n_1, n_2, \dots, n_N)				=T.INV.2T(probability[0.05], deg. freedom [N-1])	
peak area IS						
y8+ water	0.015263	17	0.549747	0.027764	2.119905	NO
y7+ water	-1.11033	17	0.549747	-2.01971	2.119905	NO
y8++ water	-0.92058	17	0.549747	-1.67455	2.119905	NO
residuals						
y8+_water	-1.46968	6	0.845154	-1.73895	2.570582	NO
y7+_water	-1.49405	6	0.845154	-1.76778	2.570582	NO
y8++_water	1.954448	6	0.845154	2.312535	2.570582	NO
y8+_cellmed	0.52323	6	0.845154	0.619095	2.570582	NO
y7+_cellmed	-2.03877	6	0.845154	-2.4123	2.570582	NO
y8++_cellmed	0.811712	6	0.845154	0.960431	2.570582	NO

Calculation method for normality assessment – peak area IS, fragment y8+_water

The standard error of skewness (SES) with N observations was calculated by the equation:

$$SES = \frac{6N(N-1)}{(N-2)(N+1)(N+3)}$$

For N=17, SES was calculated to be:

$$SES = \frac{6 * 17(17-1)}{(17-2)(17+1)(17+3)} = 0.549747 \quad (\text{Equation 4})$$

t_{skew} was calculated by the equation:

$$t_{skew} = \frac{skew}{SES}$$

For skew = 0.015263 and SES = 0.549747, t_{skew} was calculated:

$$t_{skew} = \frac{0.015263}{0.549747} = 0.027764$$

Grubb's test

Sorted (Ascending) dataset of fragment y8+ peak area from **Table 36** with the outlier marked in red: 2694, 77513, 84585, 89091, 95611, 97796, 100928, 104000, 108270, 109855, 110481, 112026, 112511, 115713, 116465, 125670, 130889, 138851. With sample mean = 101831 and standard deviation = 28410

Calculation method

The test statistic G, for outlier Y_i , sample mean \bar{Y} and the standard deviation of the sample mean s, is given by the formula:

$$G_{test} = \frac{|Y_i - \bar{Y}|}{s}$$

For $Y_i = 2694$, $\bar{Y} = 101831$ and $s = 28410$, gives:

$$G_{test} = \frac{|2694 - 101831|}{28410} = 3.4896 \dots$$

The critical G value, for sample size N, degrees of freedom N-2, significance level α and the t-critical value $t_{\frac{\alpha}{2N}, N-2}$, is given by the formula:

$$G_{critical} = \frac{N - 1}{\sqrt{N}} * \sqrt{\frac{(t_{\frac{\alpha}{2N}, N-2})^2}{N - 2 + (t_{\frac{\alpha}{2N}, N-2})^2}}$$

For N = 18, $\alpha = 0.05$ and $t_{\frac{\alpha}{2N}, N-2} = 2.12$, gives:

$$G_{critical} = \frac{18 - 1}{\sqrt{18}} * \sqrt{\frac{2.12^2}{18 - 2 + 2.12^2}} = 1.8764 \dots$$

For $G_{test} \geq G_{critical}$, the null hypothesis is rejected.

Welch's t-test – calibration curve slope for y8+

Table 40 contains the raw data for Welch's t-test on y8++ calibration curve slope and **Table 41** contains the statistical output file.

Table 40: Raw data for Welch's t-test - calibration curve for y8++ include the slope for the linear regression for each replicate set of calibration curves.

cons	ratio					
	water			cellmed		
	#1	#2	#3	#1	#2	#3
0.1	0.1076	0.0939	0.096	0.2336	0.1273	0.1311
0.5	0.5197	0.5234	0.4827	0.273	0.5553	
1	0.8711	0.8651	0.8004	1.3706	1.4191	0.6187
2	1.1768	1.5635	2.0604	4.0607	1.8263	3.3028
5	3.631	4.9885	4.4185	4.1404	3.7171	4.0878
10	11.0121	4.9793	7.146	10.1552	9.7583	8.5115
slope from lin. reg	1.0755	0.5325	0.7192	0.9529	0.9309	0.8143

Table 41: Welch's t-test output – Calibration curve for y8++

t-Test: Two-Sample Assuming Unequal Variances

	<i>water</i>	<i>cellmed</i>
Mean	0.954133333	0.934866667
Variance	0.048932333	0.005731613
Observations	3	3
Hypothesized Mean Difference	0	
df	2	
t Stat	0.142730478	
P(T<=t) one-tail	0.449792216	
t Critical one-tail	2.91998558	
P(T<=t) two-tail	0.899584432	
t Critical two-tail	4.30265273	

Single Factor ANOVA – fragment peak areas

Table 42 contains the raw data for ANOVA of LLVA*GEGHTR fragment peak areas and **Table 43** contains the statistical output file.

Table 42: Dataset for ANOVA of LLVA*GEGHTR fragment peak areas. F2 removed, poor injection, significantly lower intensity.

Area LLVA*GEGHTR (IS)			
replicate	y8+	y7+	y8++
A1	104000	101290	64196
A2	97796	106328	70673
A3	112511	109280	77326
B1	109855	110748	77487
B2	125670	124025	70027
B3	110481	122070	73665
C1	108270	127845	81570
C2	112026	116389	85906
C3	115713	109749	81571
D1	130889	133344	86623
D2	100928	114492	77307
D3	138851	128246	85186

E1	116465	105723	87731
E2	89091	93583	57328
E3	95611	99089	61417
F1	77513	59482	40904
F3	84585	87928	45107

Table 43: Raw ANOVA output file for LLVA*GEGHTR fragment peak areas.

Anova:
Single
Factor

SUMMARY

Groups	Count	Sum	Average	Variance
y8+	17	1830255	107662.058	257640213.
y7+	17	1849611	108800.647	319488926
y8++	17	1224024	72001.4117	199072560

ANOVA

Source of Variation	SS	df	MS	F	P-value	F crit
Between Groups	1488725048	4	7443625242	28.7694238	6.13611E-09	3.19072733
Within Groups	1241922719	9	258733900	8		6
Total	2730647768	3				

Calculation method for LSD – fragment peak areas

$$LSD_{A,B} = t_{\alpha,df} * \sqrt{MSW \left(\frac{1}{n_A} + \frac{1}{n_B} \right)}, \quad (\text{Equation 5})$$

where $t_{\alpha,df}$ is the two-tailed t-statistic at a given α with degrees of freedom (df) for the Between Groups Variation ANOVA statistic, MSW is the mean square for the Within Group Variation

ANOVA statistic and n_A and n_B are the number of observations for the respective groups. If all groups contain the same number of observations, the LSD is only calculated once.

For the ANOVA output in **Table 43**, $t_{0.05,2} = 4.30$, $MSW = 258733900$, $n_A = n_B = 17$ which gives

$$LSD_{A,B} = 4.30 * \sqrt{258733900 \left(\frac{1}{17} + \frac{1}{17} \right)} = 23739.$$

From **Table 44** below (in red) is the group which significantly differs from the two other groups.

Table 44: LSD for peak areas of fragment y8+, y7+ and y8++.

<i>Groups</i>	<i>Average</i>	<i>y8+ - Groups</i>	<i>Difference greater than LSD?</i>
y8+	107662		-
y7+	108800	1139	No
y8++	72001	35660	Yes

7.4.7 Detection attempt of ALT1 standard

The chromatograms from one of the first attempts with a protein column-load of 2.5 ng (estimated from BCA assay) has been depicted in **Figure 56**. The yellow field in the chromatograms indicates the elution window based on retention time predictions. A protein column-load of 2.5 ng was expected to produce detectable peak signals, given that HSA peptides previously were detected at a protein column-load of 100 pg (**Figure 33**). The chromatograms for the tryptic ALT peptides had no identifiable peak pattern. The sharp signal from FAFEER had a very narrow peak, which usually indicates that the signal comes from noise or LC pump irregularities. It was decided to pre-eliminate peptide LFLLADEVYQDNVYAAGSQFHSFK, due to its high hydrophobicity index of 48.46, which would require non-favorable alterations to the reconstitution solution.

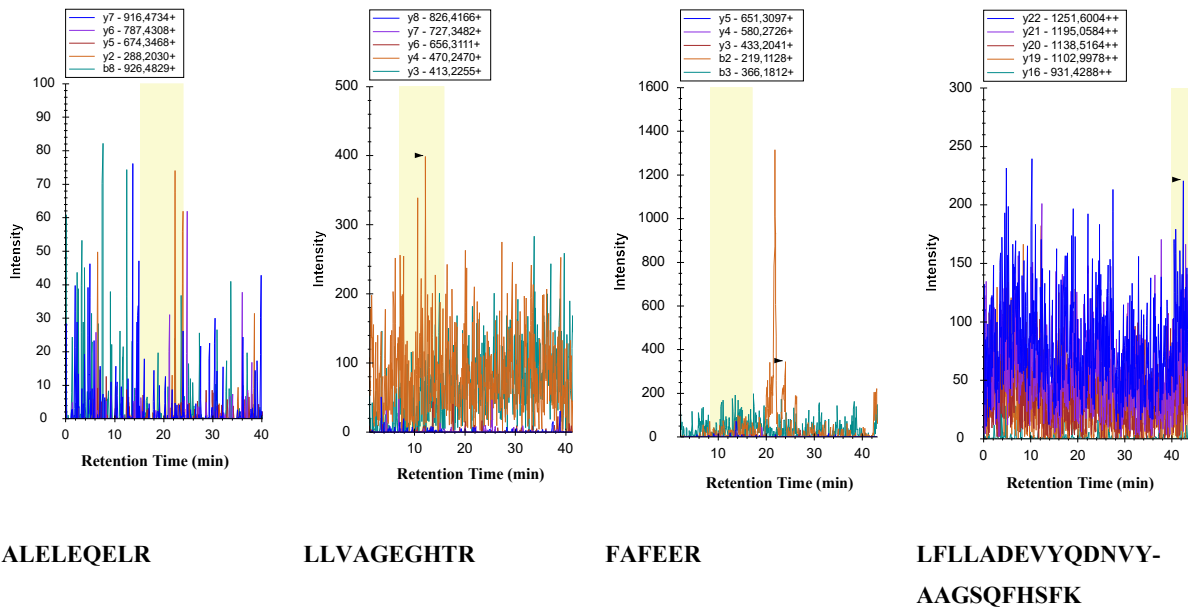


Figure 56: MRM chromatograms for ALT1 surrogate peptides from 2.5 ng ALT1 standard on-column (n=1). detection attempt. Chromatograms were acquired with SRC#2 and the yellow fields indicate retention time prediction. Raw data has not been included.

A thorough investigation of the protein standard source documents revealed that the ALT standard, as delivered by the manufacturer, was solubilized in a buffer containing among others bovine serum albumin (BSA) to stabilize ALT enzyme activity. The concentration of ALT or the ALT-to-buffer ratio was not stated. The initial column load, which was based on the total protein content of the sample was thereby misinterpreted. The source document could, however, verify that only ALT isoform 1 was present in the sample. Increasing the protein column-load incrementally from 2.5 ng to 250 ng and running an additional full scan (not shown) did neither produce an analyte signal.

End.